FINAL TECHNICAL REPORT

A: COVER SHEET

Name of Submitting Organization: Nuonics, Inc.

Address of Submitting Organization: 1862 Royal Majesty Court, Oviedo, FL 32765

Tel: 407-256-0028

DOE Award No.: DE-FC26-03NT41923

Project Title: Ultra-High Temperature Sensors Based on Optical Property Modulation and Vibration-Tolerant Interferometry

Dated: Dec.15, 2008.

Principal Author: Dr. Nabeel A. Riza (email: nriza@aol.com)

Period Covered by Report: Oct. 1, 2003 – September 30, 2008.

Type of Report: Final Technical Report

B: ABSTRACT

In this program, Nuonics, Inc. has studied the fundamentals of a new Silicon Carbide (SiC) materials-based optical sensor technology suited for extreme environments of coal-fired engines in power production. The program explored how SiC could be used for sensing temperature, pressure, and potential gas species in a gas turbine environment. The program successfully demonstrated the optical designs, signal processing and experimental data for enabling both temperature and pressure sensing using SiC materials. The program via its sub-contractors also explored gas species sensing using SiC, in this case, no clear commercially deployable method was proven. Extensive temperature and pressure measurement data using the proposed SiC sensors was acquired to 1000 deg-C and 40 atms, respectively. Importantly, a first time packaged all-SiC probe design was successfully operated in a Siemens industrial turbine rig facility with the probe surviving the harsh chemical, pressure, and temperature environment during 28 days of test operations. The probe also survived a 1600 deg-C thermal shock test using an industrial flame.

C: TABLE OF CONTENTS

A: COVER PAGE	1
B: ABSTRACT	2
C: TABLE OF CONTENTS	3
D: LIST OF GRAPHICAL MATERIALS	4
E: INTRODUCTION	13
F: EXECUTIVE SUMMARY	14
G: EXPERIMENTAL RESULTS	15
H: RESULTS AND DISCUSSION	105
I: CONCLUSION	111
J: REFERENCES	114

D: LIST OF GRAPHICAL MATERIALS

Figures

Fig. 1 Proposed basic design of the extreme environment minimally invasive optical sensor using single crystal SiC. PD_1/PD_2:Freespace Coupled Photo-detector; $M_1/M_2/M_3/M_4$: Chip Selection and Alignment Mirrors; M_5: Feedback Mirror; EOSCs: Etalon Optical Sensor Chips, e.g., Single Crystal Silicon Carbide Chip; PC: Polarization Controller; TL_1: Tunable Laser ; I: Fiber Optic Isolator; FL_1:Fiber Lens of Self Imaging Type with Half Self imaging Distance d_s where beam waist w_i is located ; P_1: Polarizer with a small angle along p-polarization direction; PBS_1:Polarization Beam Splitter; SL1/SL2: Imaging Lenses of Focal Lengths F_1/F_2 ; TM: Beam Spoiling Correction Adaptive Mirror; QWP_1: Quarter-wave Plate or 45^0 power Faraday Rotator; SMF: Single Mode Fiber.

Fig. 2. Experimental set-up of demonstrated SiC-based minimally invasive optical sensor for extreme temperature measurements. TL: Tunable laser, PBS: Polarization Beam Splitter, QWP: Quarter Wave Plate, SMF: Single Mode Fiber. FL_1:Fiber Lens of Self Imaging Type with Half Self imaging Distance d_s where beam waist w_i is located ; S_1/S_2 Imaging Lenses of Focal Lengths F_1/F_2.

Fig. 3. Sensor provided raw optical power measurements at 1547 nm as the SiC chip temperature is raised to 1000^0C.

Fig. 4. Sensor provided raw optical power measurements at 1530 nm as the SiC chip temperature is raised to 1000^0C.

Fig. 5. Sensor provided normalized $cos\{\phi_1(T)\}$and $cos\{\phi_2(T)\}$ measurements at 1547 nm and 1530 nm as the SiC chip temperature is raised to 1000^0C.

Fig. 6. Sensor Unwrapped Phase Shift Data $\Delta\phi_1(T)$ in Radians versus SiC Chip Temperature (^{0}C) with data taken at 1547 nm. A weak quadratic curve fit is achieved for this data.

Fig. 7. Sensor Unwrapped Phase Shift Data $\Delta\phi_2(T)$ in Radians versus SiC Chip Temperature (^{0}C) with data taken at 1530 nm. A weak quadratic curve fit is achieved for this data.

Fig. 8. Unwrapped Phase Shift Difference $\phi_{12} = \Delta\phi_1 - \Delta\phi_2$ data for the two wavelengths used for the sensor operations.

Fig. 9. Three dimensional (3-D) representation of the sensor calibration chart for the unambiguous instantaneous temperature measurement via the demonstrated sensor from room conditions to 100 ^{0}C. This 3-D plot uses the instantaneous phase difference data $\Delta\phi(T)$, instantaneous phase shift $\phi_1(T)$, and given temperature T.

Fig. 10: Proposed SiC-chip based wireless optical pressure sensor.

Fig. 11: Shown are the two Key Mechanical Models, (a) Clamped Edge model and (b) Simply Supported model, used to analyze the SiC Chip mechanical deformation behavior when seated in the proposed high pressure capsule.

Fig. 12: Plot shows maximum SiC chip deflection 'w_{max}' (at the center of the chip) under applied pressure for the Clamped Edge and Supported Edge boundary condition models. The chip boundary diameter was taken to be 5 mm.

Fig. 13: The expected stress produced in SiC sensor chip of 5 mm diameter and 280 µm thickness.

Fig. 14: Plot shows the effective theoretical focal length 'f_m' of the SiC chip acting as a convex mirror due to applied pressure. The focal length decreases as the differential pressure is increased.

Fig. 15: Experimental design used for seating the SiC chip in the high pressure capsule.

Fig. 16: Snap shot of the experimental seating components and their arrangements used for seating the 6-H SiC chip in the high pressure capsule. Components in photograph are labeled as: A: Brass chip seat holder with sealant canal and grooves; B: Steel seat; C: Aperture seat (washer) and D: SiC chip.

Fig. 17: SiC chip-based pressure system $I_i(x,y)$ optical images produced for (a) 0 atm, (b) 13.6 atm (200 psi), (c) 27.2 atm (400 psi), and (d) 40.8 atm (600 psi) high differential pressure conditions in the pressure capsule. Photo both axes dimensions in CCD pixel count.

Fig. 18: Plot shows demagnification of incident beam size as it reflects from the SiC chip under pressure acting as a weak convex mirror coupled to a 1:1 image inversion system.

Fig. 19: Plot shows the experimental beam demagnification along with the theoretical demagnification for Clamped and Supported sensor chip models. The behavior of the chip shifts from clamped model towards supported model as the pressure increases.

Fig.G.3.1 Schematic diagram of the LAMP Lab. experimental setup for the gas sensing experiment.

Fig. G.3. 2 (Pd-P) Reflected power of Pd-P doped silicon carbide upon exposure to nitrogen gas at Different pressure (a) 296 psi and (b) 300 psi (c) 392 psi (d) 400 psi as a function of temperature for normal incidence angle.

Fig. G.3.2 (B) Reflected power of B doped silicon carbide upon exposure to nitrogen gas at Different pressure (a) 296 psi and (b) 300 psi (c) 392 psi (d) 400 psi as a function of temperature for normal incidence angle.

Fig. G3. 3 Pd-P1 (I) Reflected power of Pd-P doped silicon carbide upon exposure to nitrogen and Hydrogen partial gas pressure: Nitrogen 294 psi + Hydrogen 4 psi as a function of temperature for normal incidence angle. (II) Contribution of Hydrogen on the refractive index of compressed layer at total pressure of 300 psi as a function of temperature.

Fig. G3.3 Pd-P2 (I) Reflected power of Pd-P doped silicon carbide upon exposure to nitrogen and Hydrogen partial gas pressure: Nitrogen 392 psi + Hydrogen 8 psi as a function of temperature for normal incidence angle. (II) Contribution of Hydrogen on the refractive index of compressed layer at total pressure of 400 psi as a function of temperature.

Fig. G.3.3 B1 (I) Reflected power of B doped silicon carbide upon exposure to nitrogen and Hydrogen partial gas pressure: Nitrogen 294 psi + Hydrogen 4 psi as a function of temperature for normal incidence angle. (II) Contribution of Hydrogen on the refractive index of compressed layer at total pressure of 300 psi as a function of temperature.

Fig.G.3.3B2 (I) Reflected power of B doped silicon carbide upon exposure to nitrogen and Hydrogen partial gas pressure: Nitrogen 392 psi + Hydrogen 8 psi as a function of temperature for normal incidence angle. (II) Contribution of Hydrogen on the refractive index of compressed layer at total pressure of 400 psi as a function of temperature.

Fig.G.3.4Pd-P1 (I) Reflected power of Pd-P doped silicon carbide upon exposure to nitrogen and Carbon Monoxide partial gas pressure: Nitrogen 294 psi + Carbon Monoxide 4 psi as a function of temperature for normal incidence angle. (II) Contribution of Carbon Monoxide on the refractive index of compressed layer at total pressure of 300 psi as a function of temperature.

Fig.G3.4Pd-P2 (I) Reflected power of Pd-P doped silicon carbide upon exposure to nitrogen and Carbon Monoxide partial gas pressure: Nitrogen 392 psi + Carbon Monoxide 8 psi as a function of temperature for normal incidence angle. (II) Contribution of Carbon Monoxide on the refractive index of compressed layer at total pressure of 400 psi as a function of temperature.

Fig.G3.4B1 (I) Reflected power of B doped silicon carbide upon exposure to nitrogen and Carbon Monoxide partial gas pressure: Nitrogen 294 psi + Carbon Monoxide 4 psi as a function of temperature for normal incidence angle. (II) Contribution of Carbon Monoxide on the refractive index of compressed layer at total pressure of 300 psi as a function of temperature.

Fig.G3.4B2 (I) Reflected power of B doped silicon carbide upon exposure to nitrogen and Carbon Monoxide partial gas pressure: Nitrogen 392 psi + Carbon Monoxide 8 psi as a function

of temperature for normal incidence angle. (II) Contribution of Carbon Monoxide on the refractive index of compressed layer at total pressure of 400 psi as a function of temperature.

Fig.G3.5Pd1 (I) Reflected power of Pd doped silicon carbide upon exposure to nitrogen and Carbon Dioxide partial gas pressure: Nitrogen 296 psi + Carbon Dioxide 4 psi as a function of temperature for normal incidence angle. (II) Contribution of Carbon Dioxide on the refractive index of compressed layer at total pressure of 300 psi as a function of temperature.

Fig.G3.5Pd-P2 (I) Reflected power of Pd-P doped silicon carbide upon exposure to nitrogen and Carbon Dioxide partial gas pressure: Nitrogen 392 psi + Carbon Dioxide 8 psi as a function of temperature for normal incidence angle. (II) Contribution of Carbon Dioxide on the refractive index of compressed layer at total pressure of 400 psi as a function of temperature.

Fig.G3.5B1 (I) Reflected power of B doped silicon carbide upon exposure to nitrogen and Carbon Dioxide partial gas pressure: Nitrogen 296 psi + Carbon Dioxide 4 psi as a function of temperature for normal incidence angle. (II) Contribution of Carbon Dioxide on the refractive index of compressed layer at total pressure of 300 psi as a function of temperature.

Fig.G.3.5B2 (I) Reflected power of B doped silicon carbide upon exposure to nitrogen and Carbon Dioxide partial gas pressure: Nitrogen 392 psi + Carbon Dioxide 8 psi as a function of temperature for normal incidence angle. (II) Contribution of Carbon Dioxide on the refractive index of compressed layer at total pressure of 400 psi as a function of temperature.

Fig.G.3.6Pd-P1 (I) Reflected power of Pd-P doped silicon carbide upon exposure to nitrogen and Methane partial gas pressure: Nitrogen 296 psi + Methane 4 psi as a function of temperature for normal incidence angle. (II) Contribution of Methane on the refractive index of compressed layer at total pressure of 300 psi as a function of temperature.

Fig.G3.6Pd-P2 (I) Reflected power of Pd-P doped silicon carbide upon exposure to nitrogen and Methane partial gas pressure: Nitrogen 392 psi + Methane 8 psi as a function of temperature for normal incidence angle. (II) Contribution of Methane on the refractive index of compressed layer at total pressure of 400 psi as a function of temperature.

Fig.G.3.6B1 (I) Reflected power of B doped silicon carbide upon exposure to nitrogen and Methane partial gas pressure: Nitrogen 296 psi + Methane 4 psi as a function of temperature for normal incidence angle. (II) Contribution of Methane on the refractive index of compressed layer at total pressure of 300 psi as a function of temperature.

Fig.G3.6B2 (I) Reflected power of B doped silicon carbide upon exposure to nitrogen and Methane partial gas pressure: Nitrogen 392 psi + Methane 8 psi as a function of temperature for normal incidence angle. (II) Contribution of Methane on the refractive index of compressed layer at total pressure of 400 psi as a function of temperature.

Fig.G3. 7a (I) Reflected power of undoped silicon carbide upon exposure to nitrogen and Methane partial gas pressure: Nitrogen 296 psi + Methane 4 psi as a function of temperature for normal incidence angle. (II) Contribution of Methane on the refractive index of compressed layer at total pressure of 300 psi as a function of temperature.

Fig.G3. 7b (I) Reflected power of undoped silicon carbide upon exposure to nitrogen and Methane partial gas pressure: Nitrogen 392 psi + Methane 8 psi as a function of temperature for normal incidence angle. (II) Contribution of Methane on the refractive index of compressed layer at total pressure of 400 psi as a function of temperature.

FigG3.8.Digital photographs of palladium-phospohorus and boron laser doped 4H-SiC chips.

Figure G3. 9. Project activities for SiC chip development, chip fabrication and optical response studies.

Fig. G3. 10. Laser-doped Palladium-Phosphorus profile in 4H-SiC substrate. The parent wafer was an undoped 4H-SiC substrate. A standard needs to be procured and analyzed to accurately convert counts per second to concentration.

Fig. G3. 11. Laser-doped Boron profile in 4H-SiC substrate. The parent wafer was an undoped 4H-SiC substrate. The sample has exceeded the solid solubility limit of $2.5x10^{20}$ cm^{-3} for B in SiC at the surface.

Fig. G3. 12. Parent wafer type: undoped 4H-SiC. Optical profilometric data for laser-untreated wafer surface. The average surface roughness (Ra) is 5 nm and the peak to valley roughness is 163.76 nm. This is the opposite surface of the Pd-P-doped surface.

Fig. G3. 13. Parent wafer type: undoped 4H-SiC. Optical profilometric data for laser-treated (laser-doped) wafer surface. The average surface roughness (Ra) is 12.49 nm and the peak to valley roughness is 1.22 μm. This is the Pd-P-doped surface.

Fig. G3. 14. Parent wafer type: undoped 4H-SiC. Optical profilometric data for laser-untreated wafer surface. The average surface roughness (Ra) is 4.48 nm and the peak to valley roughness is 56.98 nm. This is the opposite surface of the B-doped surface.

Fig. G3. 15. Parent wafer type: undoped 4H-SiC. Optical profilometric data for laser-treated (laser-doped) wafer surface. The average surface roughness (Ra) is 3.14 nm and the peak to valley roughness is 64.17 nm. This is the B-doped surface.

Fig.G4.1. All-SiC frontend probe-based optical sensor system for extreme gas temperature measurements in combustion engines.

Fig.G.4.2. SiC temperature frontend probe shown in an (a) unassembled and (b) assembled fashion.

Fig.G4.3. All-SiC temperature sensor deployed for a first test at Siemens rig facility.

Fig.G4.4 The assembled sensor optical transceiver module top view.

Fig.G4.5. IR CCD camera (8.8 mm x 6.6 mm active area view) received laser beam snap shots during thermal shock stage indicating on/off oscillatory Fabry-Perot etalon behavior of SiC optical chip due to the rapid thermal gradient. Left Photo: Power Max; Right Photo: Power Min.

Fig.G4.6 After first rig test of probe, expected part frontend discoloration is seen due to chemical exposure in combustor refractory section.

Fig.G4.7. Raw optical data recorded by the probe PD indicating the rig thermal ramp zone and the relative high temperature stabilization zone. Vertical axis is measured optical power in Watts; Horizontal axis is a time counter.

Fig.G4.8 Rig TC provided temperature reading during the Fig.G4.7 optical data acquisition period. This TC data is used for optical probe calibration. Vertical axis is measured temperature; Horizontal axis is a time counter.

Fig.G4.9. 15 min snap shot of optical power readings from probe during the stable ~ 1107 ºC region of the rig operation.

Fig.G4.10 TC data during the Fig.G4.9 data 15 min. time period.

Fig.G4.11. TC calibrated optical probe temperature sensing curve that can be used to deduce temperature readings.

Fig.G4.12. All-SiC probe and Type-R High Temperature Thermo-Couple under oxy-acetylene flame thermal and localized thermal ramp joint test with temperatures reaching 1600 ºC.

Fig.G4.13. Condition of Viton seal used in the probe connector before and after 28 days in rig.

Fig.G4.14 Probe condition showing copper sulphate deposits after 28 continuous days in the rig.

Tables

Table 1: Theoretical Central Deflections and Focal Lengths of the SiC Chip Convex Mirror versus Pressure.

Table 2: Experimental Optical Image Size vs. Capsule Differential Pressure P.

Table G.3.1. Typical combustion gas compositions.

Table G3.2.1: Contribution on compressed layer refractive index by pure nitrogen

Table G3.2.2: Contribution on compressed layer refractive index by different doping elements.

Table G3. 3. Palladium-Phosphorus Laser Doping Parameters.

Table G3. 4. Boron Laser Doping Parameters.

Table G4.1: Summary of all-SiC probe test at Siemens rig.

E: INTRODUCTION

The energy production community is looking for robust sensor solutions for the extreme conditions of next generation clean air coal-fired power plants. It has been known for some time that operating gas turbines with higher (e.g., > 1500 deg-C) can lead to higher efficiency and cleaner energy production [1] that is good for the environment and also good for business. Nevertheless, the dominant precious metals high temperature Thermo-Couple (TC) technology [2-3] that is deployed in these higher temperature test engines show unreliable performance, both from a temperature measurement and mechanical robustness point-of-view. The problem arises when different materials are combined to make these high temperature measurement probes, whether prior-art commercial electrical designs like packaged TCs or research community optical designs [4-9], e.g., sapphire fiber with gratings and external fiber packaging. Because fundamentally different materials have different Coefficient of Thermal Expansion (CTE) coefficients, CTE mismatch in the present probe designs leads to mechanical stresses and eventual probe failure.

To reach this goal of a new sensor technology for power plants, the DOE sponsored the present research program at Nuonics. Specifically, the objective of this program was to lay the solid technical foundations of a novel optical sensor technology based on high robustness SiC materials that would enable the robust and reliable sensing of temperature, pressure, and gas species in the gas turbine of a power plant. In addition, another objective of the program was to show if the proposed sensor technology when packaged as an industrial test probe can survive the harsh industrial environment of a commercial test turbine test.

F: EXECUTIVE SUMMARY

The program started with the theme that single crystal thick (e.g., 300 microns) SiC is a robust front-end optical sensor chip that could survive the harsh environment of a gas turbine and the chip optical property of refractive index is encoded with the gas temperature, pressure, and species information that can be recovered using optical interferometry.

Indeed on two fronts of temperature and pressure sensing, the program conclusively showed the novel optical designs, signal processing, and experimental data that forms the foundation of novel probe designs for future generation gas turbine deployment. Specifically, both optical and mechanical properties of the thick SiC chip in combination with wired and wireless optics were intelligently engaged with smart signal processing methods to realize the much needed extreme environment temperature sensing [10-16] as well as pressure sensing [17-19].

In addition, for the first time, all-SiC probe packaging was implemented to realize a temperature sensor that underwent successful commercial combustor test rig testing at a Siemens facility. Although the program was subjected to both large and small sub-contractor based delays, the program accomplished its major technical milestones within budget and DOE allocated time-lines. The Nuonics Small Business program has now laid an exciting platform for a novel sensor technology for temperature and pressure sensing for future energy production systems.

The temperature and pressure sensor work and Siemens site temperature probe rig tests work reported in this document has been conducted by Dr.Riza's team at Nuonics and PIPS Lab., CREOL-UCF. The gas species sensor work reported in this document has been conducted by Prof. Kar's team including Applicote Associates and the LAMP Lab., CREOL-UCF.

G: EXPERIMENTAL RESULTS

G.1 Temperature Sensing Fundamentals

Proposed Sensor Optical Design

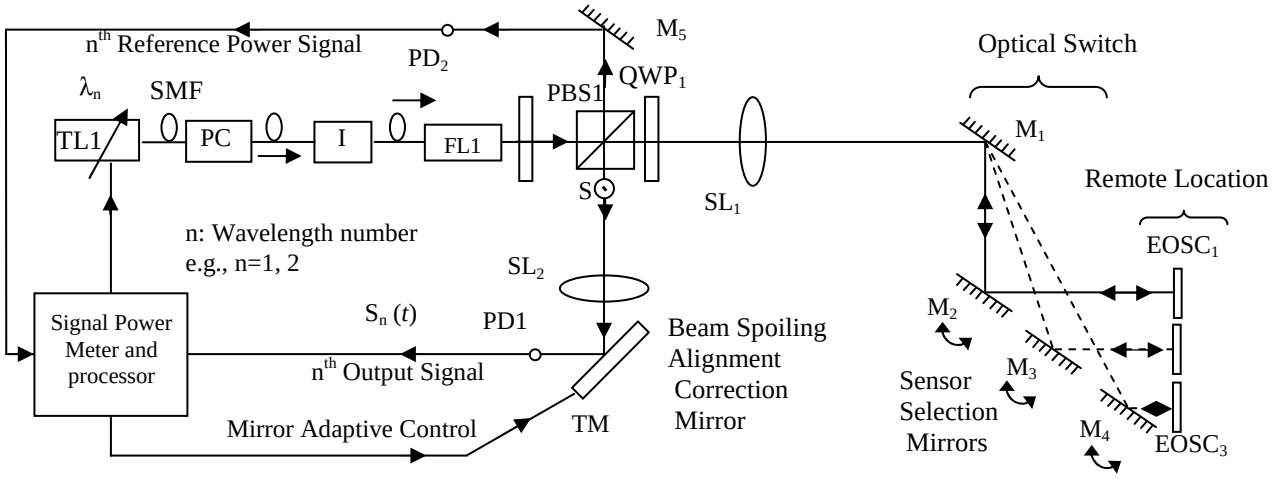

Fig. 1 Proposed basic design of the extreme environment minimally invasive optical sensor using single crystal SiC. PD_1/PD_2:Freespace Coupled Photo-detector; $M_1/M_2/M_3/M_4$: Chip Selection and Alignment Mirrors; M_5: Feedback Mirror; EOSCs: Etalon Optical Sensor Chips, e.g., Single Crystal Silicon Carbide Chip; PC: Polarization Controller; TL_1: Tunable Laser ; I: Fiber Optic Isolator; FL_1:Fiber Lens of Self Imaging Type with Half Self imaging Distance d_s where beam waist w_i is located ; P_1: Polarizer with a small angle along p-polarization direction; PBS_1:Polarization Beam Splitter; SL1/SL2: Imaging Lenses of Focal Lengths F_1/F_2 ; TM: Beam Spoiling Correction Adaptive Mirror; QWP_1: Quarter-wave Plate or 45^0 power Faraday Rotator; SMF: Single Mode Fiber.

Fig.1 shows the proposed basic design of the high temperature minimally invasive optical sensor. The sample front-end is composed for example of three weak Etalon Optical Sensor Chips (EOSCs) using single crystal SiC. Light from a tunable laser passes via fiber-optics such as a

polarization controller (PC) and isolator (I) to exit via a fiber lens (FL_1) to produce a freespace beam. This light then passes via a polarizer P_1 (at a slight angle to the horizontal or p-polarization direction) and a polarizing beam splitter PBS_1 to produce a s or vertically polarized reflected beam that via mirror M_5 enters photodetector PD_2 whose output is used to access sensor efficiency. The straight linearly (or horizontally) polarized beam from PBS_1 passes via a quarter-wave plate QWP_1 (or 45^0 power Faraday rotator) and a bulk spherical lens SL_1. The use of QWP_1 gives polarization insensitivity to the SiC sensing operations as circularly polarized light strikes the SiC crystal that can possess some birefringence. The lenses are used to reduce beam spreading loss. The mirrors M_1, M_2, M_3, and M_4 are 2-axis mirrors that are adjusted to select the desired EOSC and implement normal incidence alignment with the etalon chip. All mirror optics can also be made of high temperature capability SiC foam material such as used for space telescope applications. Because of its high refractive index (e.g., 2.57), single crystal SiC chip acts as a natural weak etalon in air with about 20% optical reflectivities at the two air-SiC interfaces. Light reflected from the chosen etalon chip traces the path back via the mirrors and SL_1 to reflect via PBS_1 as vertically polarized light towards spherical lens SL_2. The returning light via SL_2 then passes via the beamforming mirror TM to strike a freespace coupled photodetector PD_1. TM is a beam spoiling correction mirror such as a deformable mirror that as needed corrects wavefront distortions and keeps the returning beam aligned on PD_1 to produce the optimal sensing signal based on optical path length changes in the front-end etalon chip. Because the EOSCs can be mounted on various platforms that may have vibrations or other beam perturbing environmental effects such as air currents, pressure gradients, thermal gradients, the returning freespace beam from the sensing zone can suffer unwanted beam motions and wavefront distortions. Hence, for proper sensor operation, the returning beam must strike the active detection zone of the free-space large area (e.g., a few millimeter diameter) point

photodetector. Note that as the SiC crystal etalon optical path length changes due to change in sensing zone temperature, the etalon reflected signal power varies and can undergo several power variation cycles. To maintain proper sensor operation and calibration as explained next, the instantaneous PD_1 produced power level signal is normalized before signal processing required to compute the sensed temperature. This normalization is done in a no-moving parts electronic fashion by sweeping the laser wavelength to synthesize optical path length changes and then measure the nearest power maximum and minimum and using these max/min data for the instantaneous reading normalization, hence giving robustness to the sensor operations.

The proposed non-invasive sensor utilizes the SiC crystal Fabry-Perot cavity interference to extract sensing information. Specifically, classic expression for the reflectance from a Fabry-Perot type interference due to multiple reflections between two parallel dielectric plates with front surface power reflection of R_1 and back surface power reflectance R_2 is given by:

$$R_{FP} = \frac{R_1 + R_2 + 2\sqrt{R_1 R_2}\cos\phi}{1 + R_1 R_2 + 2\sqrt{R_1 R_2}\cos\phi} \ . \qquad (1)$$

Note that the SiC chip also acts as a natural optical window that can be placed as a sealing window separating an extreme temperature hazardous zone from a safe lower hazard zone. In this case for the single crystal SiC chip, R_1 is the reflectivity provided by the air-SiC interface facing the light beam present in the preferably friendlier zone while R_2 is the reflectivity provided by the SiC-air interface present in the hazardous extreme temperature zone. It is also possible to place the SiC chip as a mounted chip exposed to the entire extreme temperature zone with both crystal interfaces engaging the light beam equally exposed to high temperature.

An optical path length (OPL) parameter in radians for the proposed sensor is defined as:

$$\text{OPL} = \phi = \frac{4\pi n(\lambda) d}{\lambda}, \qquad (2)$$

where ϕ is the round-trip propagation phase in the SiC crystal of thickness *d* and refractive index *n* at a tunable laser wavelength λ at normal incidence. It can be shown that for Eq. 1, the maximum value of the reflectivity $R_{FP_{\max}}$ occurs when $cos(\phi) = 1$ and the minimum value of reflectivity $R_{FP_{\min}}$ occurs when $cos(\phi) = -1$ where:

$$R_{FP_{\max}} = \frac{R_1 + R_2 + 2\sqrt{R_1 R_2}}{1 + R_1 R_2 + 2\sqrt{R_1 R_2}} = \frac{(r_1 + r_2)^2}{(1 + r_1 r_2)^2}$$
$$R_{FP_{\min}} = \frac{R_1 + R_2 - 2\sqrt{R_1 R_2}}{1 + R_1 R_2 - 2\sqrt{R_1 R_2}} = \frac{(r_1 - r_2)^2}{(1 + r_1 r_2)^2} \qquad (3)$$

Note that the Eq. 3 expressions are simplified by using the relations $R_1 = r_1^2$ and $R_2 = r_2^2$ where r_1 and r_2 are the Fresnel amplitude reflection coefficients for the chip front and back interfaces, respectively. Given the input light travels through air with refractive index n_0=1, SiC chip with index *n*, and external hazardous zone with index n_1, the Fresnel power reflection coefficients for the SiC chip front and hazard zone interfaces can be written as:

$$R_1 = |r_1|^2 = \frac{(n - n_0)^2}{(n + n_0)^2}$$
$$R_2 = |r_2|^2 = \frac{(n_1 - n)^2}{(n_1 + n)^2}. \qquad (4)$$

Traditionally, a high quality Fabry-Perot cavity with deep highly narrow notches (or peaks) is designed by making highly reflective (> 95 % reflectivity) internal surfaces of the Etalon. For 6H-SiC in the near infrared region with average *n* = 2.57 and the SiC chip placed in air, using Eq. 4 gives $R_1 = R_2 = R = 0.193$. Although single crystal SiC acts as a natural etalon, it is also a very weak etalon in air due to its near 19 % reflectivity at the crystal interfaces. In fact, the classic Fabry-Perot effect is so weak that the interaction of laser light with the natural SiC crystal in air can be well approximated by classic two beam interferometry. This can be verified by the

fact that the first light beam reflected off the first air-SiC interface has 19.3% (as R=0.193) of the input beam laser power while the beam reflected by the second SiC-Air interface and returning to the sensor detector as a second optically delayed beam has a 12.5% of input laser power [as $R(1\text{-}R)^2$ = 0.125]. The third beam returning to the sensor detector after three reflections and double delay due to the SiC-Air interfaces and has only a 0.47 % power of the original input laser beam. Hence for the proposed SiC crystal-based sensor, one can use the first two beams from the SiC chip as the dominant terms for optical interference leading to the classic two-beam interferometry situation. Furthermore, if the SiC chip is placed in a hazard zone where the hazard zone contains materials other than air, R_1 and R_2 will further decrease making the two-beam interference approximation even stronger. Using this SiC specific two-beam approximation, the instantaneous detected optical power can be rewritten as:

$$P_m = K \cdot R_{FP} \approx K\left[R_1 + (1-R_1)^2 R_2 + 2(1-R_1)\sqrt{R_1 R_2}\cos\phi\right] \qquad (5)$$

where R_{FP} is the instantaneous optical reflectivity of the basic front-end SiC Fabry-Perot element while K is a constant that depends upon the experimental conditions such as input power, power meter response gain curve, beam alignments, and losses due to other optics. In addition, optical noise in the system with time can also change the amount of light received for processing, thus varying the constant K.

The overall goal of the proposed optical sensor is to use a minimally invasive technique to measure a single crystal SiC chip-based optical parameter that can then provide the temperature at the remoted SiC chip position. As seen from Eq. 5, the optical phase ϕ of the SiC chip is an appropriate sensor parameter for measurement and sensor processing. Eq. 5 also shows that the SiC sensor measured P_{m} power values will approximate a sinusoidal functional behavior.

This behavior is favorable for further data processing that will utilize phase difference values of these measured sinusoidal optical power data signals. Do note that exact expressions for the $P_{m_{\max}}$ and $P_{m_{\min}}$ values can be given as in these cases *cos*(ϕ) = 1 (for a maximum) and *cos*(ϕ) = -1 (for a minimum). These instantaneous $P_{m_{\max}}$ and $P_{m_{\min}}$ are given by:

$$P_{m_{\max}} = KR_{FP_{\max}} = K\frac{R_1 + R_2 + 2\sqrt{R_1R_2}}{1 + R_1R_2 + 2\sqrt{R_1R_2}}$$
$$P_{m_{\min}} = KR_{FP_{\min}} = K\frac{R_1 + R_2 - 2\sqrt{R_1R_2}}{1 + R_1R_2 - 2\sqrt{R_1R_2}}. \qquad (6)$$

Measurement of these localized maximum and minimum optical power values is important for normalizing the measured raw P_m data to generate the measured *cos*(ϕ) function that cannot exceed ± 1 values. Given any measurement P_m that follows a sinusoidal measurement behavior with a given $P_{m_{\max}}$ maximum value and $P_{m_{\min}}$ minimum value as achieved for a weak SiC etalon, this sinusoidal function rides on a Bias level given by Bias= 0.5{ $P_{m_{\max}}$ + $P_{m_{\min}}$ } with a max-to-min power swing given by { $P_{m_{\max}}$ - $P_{m_{\min}}$ }. To normalize this sinusoidal function so its maximum and minimum values are +1 and – 1, respectively, one must substract the bias from the power value P_m and then divide the whole function by 0.5 of the swing value, i.e.., implement the calculation { P_m – Bias}/ {0.5[$P_{m_{\max}}$ – $P_{m_{\min}}$]}, which gives the normalized value of the cosine function or Eq.7. This measured *cos*(ϕ) function using the normalization of the raw P_m data is given as:

$$\cos(\phi) = 2\frac{P_m - 0.5\times(P_{m_{\max}} + P_{m_{\min}})}{P_{m_{\max}} - P_{m_{\min}}}. \qquad (7)$$

Where $P_{m_{\max}}$ and $P_{m_{\min}}$ are the sensor measured localized optical power maximum and minimum values, respectively. The measured optical phase and phase difference values will then be used to compute the temperature measured by the sensor. Do note the equivalence of Eq. 5 representing the sensor theory and Eq. 7 that is used to implement the sensor data processing. Specifically, Eq. 5 can be rewritten to show that the Cosine of the OPL is equal to the measured optical power P_{m} minus a bias term and the resulting value divided by another bias term. In effect, Eq. 7 and Eq. 5 have the same format and hence Eq. 7 is used for real-time sensor data processing.

Note that based on the dynamic range of the single crystal SiC defined OPL parameter ϕ change due to temperature, the $cos(\phi)$ sinusoidal behavior can be over many cycles. Furthermore, based on the specific experimental conditions, the values of $P_{m_{\max}}$ and $P_{m_{\min}}$ can change for each specific cycle. Hence for calculating the OPL via an instantaneous P_{m} for a given sensing parameter condition, the $P_{m_{\max}}$ and $P_{m_{\min}}$ values within the respective OPL change single cycle should be used. Thus, for proper sensor operation of determining an instantaneous *cos*(OPL) and hence the instantaneous measurement parameter of temperature, the numerical operation of Eq. 7 needs to be implemented. This operation is done by measuring PD1 provided three power levels; namely, optical power P_{m} at the chosen wavelength and then measuring the closest (i.e., within one optical power min/max cycle), the values of $P_{m_{\max}}$ and $P_{m_{\min}}$. Key to these measurements is that the scaling factor *K* should be the same for all three measurements. As mentioned before, *K* depends on various experimental parameters such as laser power and beam alignment that can be maintained during a given measurement set. In

addition, P_{m} , $P_{m_{\max}}$, $P_{m_{\min}}$ depend on the instantaneous values of R_{FP}, $R_{FP_{\max}}$, and $R_{FP_{\min}}$, respectively. Note from Eq. 4 that $P_{m_{\max}}$ and $P_{m_{\min}}$ only depend on the SiC etalon interface Fresnel power coefficient values of R_1 and R_2. In-turn, R_1 and R_2 depend on the instantaneous refractive index n of SiC and the refractive indices of the chip front (i.e., n_0) and back-face (i.e., n_1) materials. On the other hand as seen from Eq.1, P_{m} not only depends on the instantaneous values of R_1 and R_2, but also depends on the *cos* (OPL) value where the OPL term contains not only the instantaneous refractive index of SiC, but also the instantaneous SiC chip thickness *d* and the optical wavelength λ set for the tunable laser. Here-in lies the method to rapidly measure the instantaneous values $P_{m_{\max}}$, $P_{m_{\min}}$ for a given measured instantaneous P_{m} at the chosen wavelength. Specifically, after recording P_{m}, the tunable laser is rapidly swept in wavelength about λ to make *cos*(OPL) = 1 and thus produce a $P_{m_{\max}}$ measurement. Similarly, the tunable laser is swept in wavelength about λ to make *cos*(OPL)= -1 and thus produce a $P_{m_{\min}}$ measurement. As all three PD_1 power measurements are now available, Eq. 7 is solved to get a value for the instantaneous *cos*(OPL) that will undergo signal processing to determine the sensing parameter of temperature. A key condition for the accuracy and robustness of this normalization process is that the instantaneous SiC refractive index n over the wavelength sweep range is essentially constant, thereby keeping *R* constant for all three PD1 power measurements of P_{m} , $P_{m_{\max}}$, and $P_{m_{\min}}$. It is also important that all three measurements are taken for the same exact experimental conditions (apart from wavelength) so that *K* and *T* are the same during this measurement set. One can study the effect of changing wavelength on the SiC refractive index by differentiating the OPL $\phi = \{4\pi/\lambda\}\{n\,d\}$ with respect to the wavelength giving:

$$\frac{d\phi}{d\lambda} = 4\pi d\left[\frac{-n}{\lambda^2} + \frac{1}{\lambda}\frac{dn}{d\lambda}\right] \quad (8)$$

The maximum wavelength change is required when either $P_m = P_{m_{max}}$ or $P_m = P_{m_{min}}$. In both these cases, a maximum $d\phi = \pi$ is required to change the PD_1 power reading from the maximum to minimum or vice versa. Hence, using Eq. 8 with the maximum tunable laser wavelength change conditions given by $d\phi = \pi$, $d\lambda = \Delta\lambda_{max}$, and $dn = \Delta n$, where $\Delta\lambda_{max}$ is the needed maximum wavelength change and Δn is the refractive index change caused by this wavelength change. Using these conditions and rearranging the terms of Eq. 8, one gets the needed maximum wavelength change $\Delta\lambda_{max}$ to be:

$$\Delta\lambda_{max} = \lambda\frac{\Delta n}{n} - \frac{\lambda^2}{4nd} \quad (9)$$

Eq.9 thus provides a relationship for the maximum change in tunable laser wavelength required to produce the desired local maxima $P_{m_{max}}$ and minima $P_{m_{min}}$, given an instantaneous P_m value of the sensor. Note that Eq. 9 requires knowledge of the change in refractive index Δn of the SiC material with respect to the wavelength. For 6H-SiC single crystal material, this change in refractive index in the infrared band (e.g., 1500-1600 nm) is very small, e.g., < 0.01 % . For example, assuming a 0.01% change in refractive index for a 300 μm thick SiC chip with an average refractive index of 2.57 at a wavelength of 1550 nm, the resultant $\Delta\lambda_{max}$ is found to be 0.77887 nm. However, if one neglects the change in refractive index term in Eq. 10, $\Delta\lambda_{max}$ = 0.77902 nm. Note that the 0.00015 nm difference in $\Delta\lambda_{max}$ for these two cases is extremely small and practically out of the tuning step of a typical commercial laser source. Hence, a small < 1 nm range wavelength sweep of an eye safe 1550 nm band tunable laser will be sufficient to

generate the required $P_{m_{\max}}$ and $P_{m_{\min}}$ values of light power required for normalization (via Eq. 7) of sensor instantaneous P_{m} data.

For another set of new P_{m} , $P_{m_{\max}}$, $P_{m_{\min}}$ measurements for perhaps a different K (scaling constant affected by for instance receiver beam alignment) and T (i.e., temperature in hazardous zone) situation, a new *cos*(OPL) can be computed that is also correctly normalized for further signal processing. Thus, each near instantaneous three power set reading of P_{m} , $P_{m_{\max}}$, and $P_{m_{\min}}$ is self-normalized to give the appropriate *cos*(OPL) data. Take the simple case of when the SiC chip sits in an air surrounding implying $R_1 = R_2 = R$. In this case using Eq. 6, the extreme power readings can be written as:

$$P_{m_{\max}} = K\frac{4R}{(1+R)^2} \qquad (10)$$
$$P_{m_{\min}} = 0$$

If the values of K and R (due to possible change in SiC front and back interface Fresnel reflection coefficient parameters) fluctuate over different instantaneous 3-reading power sets, the peak modulation swing $4KR/(1+R)^2$ of the PD1 power cycle (see Eq. 10) may change but the *cos*(OPL) data due to the self-normalization process from the sensor system is still accurate and robust for further signal processing. This attribute of the proposed sensor is particularly attractive for fossil fuel applications where the proposed sensor front-end SiC chip will be exposed to extreme mechanical and chemical effects that can alter receive beam alignments and also change refractive index of the medium surrounding the SiC chip that will cause a change/decrease in the Fresnel power coefficients of the SiC chip. Because the proposed sensor signal processing and operations is robust to such changes, a powerful sensor can be realized for extreme

environments. This attribute is all the more powerful when compared to standard Fabry-Perot-based sensors using broadband light and power spectrum measurements where the Fabry-Perot etalon must maintain its given spectral shape throughout sensor operations. Hence any changes in Fresnel coefficients will drastically affect the quality of the spectral filter function that will make detection of the shifts of the spectral maxima/minima all the more difficult. Recall that shaped Fabry-Perot filter functions require highly reflective etalon interfaces, a key limitation in extreme fossil fuel applications where these interface reflectivities can severely degrade with extreme and cyclic temperature swings.

The proposed instrument can also be calibrated in a continuous mode as explained next. In this case, wavelength tuning is not required to generate the $P_{m_{\max}}$ and $P_{m_{\min}}$ values required for normalization. Instead, the sensing parameter such as temperature is swept over the desired sensing zone that causes the SiC refractive index n and chip thickness d to change that in-turn causes the required max/min *cos*(OPL) change to produce naturally induced $P_{m_{\max}}$ and $P_{m_{\min}}$ values at PD1. In this case, once all the P_{m} data is recorded over the whole sensor calibration temperature range, $P_{m_{\max}}$ and $P_{m_{\min}}$ values within a given one cycle zone are used to normalize all the P_{m} values within this given one cycle power data. In this special case, it must be shown that $P_{m_{\max}}$ and $P_{m_{\min}}$ remain constant over any one power variation cycle for the proposed SiC chip. Recall that the Fresnel power reflectivity *R* for the SiC chip in air can be written as:

$$R = \frac{(n - n_0)^2}{(n + n_0)^2} \tag{11}$$

Taking the derivative of Eq. 11 on both sides with respect to the refractive index *n*:

$$dR = \frac{2(n-n_0)}{(n+n_0)}\left\{\frac{(n+n_0)-(n-n_0)}{(n+n_0)^2}\right\}dn$$

$$\Rightarrow \Delta R = \frac{4n_0(n-n_0)}{(n+n_0)^3}\Delta n \qquad (12)$$

Now consider that the sensor chip OPL $\phi = \frac{4\pi nd}{\lambda}$ undergoes a π phase change to introduce one optical power cycle variation detected by PD_1. This power variation can be due to the combined effect of change in refractive index and thickness of SiC. However, as a worst case scenario, it is assumed that the change in OPL is only due to the SiC refractive index change. Note that this condition imposes an extreme restriction on the OPL change while in practical situations; the actual restriction being less severe due to the accompanied change in thickness. Nevertheless, the corresponding change in refractive index of SiC associated with one optical power cycle is given by $\Delta n = \frac{\lambda}{4d}$. Using this value of Δ*n* in Eq. 12, the corresponding change in *R*, the coefficient of power reflectivity of the front-end sensor chip is given by:

$$\Delta R = \frac{n_0(n-n_0)}{(n+n_0)^3}\frac{\lambda}{d} \qquad (13)$$

Again the worst case for *R* change will be for SiC in air or n_0=1. As an example, using a value of *n*=2.6 typical for single crystal 6H-SiC, a thickness of 0.5 mm, and λ= 1550 nm, a Δ*R* of 0.000106 or 0.0106% is obtained. This minute change in PD_1 detected optical power reflectivity is very small to influence the per power cycle data P_m normalization procedure. Hence the assumption of constant R_1 and R_2 for one power variation cycle proposed for the sensor continuous-mode calibration is valid.

Proposed Sensor Signal Processing for Unambiguous Temperature Sensing

Now consider the proposed sensor used for measuring some arbitrary temperature T that induces changes in both refractive index and thickness of the SiC chip. The variation of chip refractive index thickness product or $n \times d$ induces a change in the PD_1 detected optical power where:

$$\cos\{\phi(T)\} = \cos\left\{\frac{4\pi n(T)d(T)}{\lambda}\right\} = \left\{2\frac{P_m - 0.5\times(P_{m_{\max}} + P_{m_{\min}})}{P_{m_{\max}} - P_{m_{\min}}}\right\}, \qquad (14)$$

$$\phi(T) = \cos^{-1}\left\{2\frac{P_m - 0.5\times(P_{m_{\max}} + P_{m_{\min}})}{P_{m_{\max}} - P_{m_{\min}}}\right\}. \qquad (15)$$

Here λ is the wavelength of operation. For a given instantaneous temperature T of the SiC chip remotely placed in the sensing environment of temperature T, PD_1 records the three optical power levels P_m, $P_{m_{\max}}$, $P_{m_{\min}}$ (as mentioned earlier), and hence the instantaneous phase $\phi(T)$ can be computed. To calibrate the sensor, this procedure is repeated for the desired temperature range of $T_{\min}$ to $T_{\max}$. The sensor provided instantaneous $\phi(T)$ phase value change from the minimum temperature to the maximum temperature given by $\Delta\phi_1(T)$ can be expressed as:

$$\Delta\phi_1 = \left\{\frac{4\pi n(T_{\max})d(T_{\max})}{\lambda_1}\right\} - \left\{\frac{4\pi n(T_{\min})d(T_{\min})}{\lambda_1}\right\} = 2\pi m + \sigma_1. \qquad (16)$$

Here, because of the rather large (e.g., 300 μm) proposed thickness of the SiC chip, $\Delta\phi_1$, the unwrapped phase obtained from Eq. 15 by adding 2π after each cycle, is expected to have m number of 2π phase cycles plus a possible fixed phase value of σ_1. Because of the presence of multiple power cycles, a phase ambiguity arises in the sensor data obtained using P_m

data at λ_1. This phase ambiguity can be removed by measuring the instantaneous sensor phase $\phi(T)$ at another carefully selected wavelength λ_2. This wavelength λ_2 is selected such that the total unwrapped phase shift change $\Delta\phi_2$ in going from $T_{\min}$ to $T_{\max}$ is increased by π and given by:

$$\Delta\phi_2 = \left\{\frac{4\pi n(T_{\max})d(T_{\max})}{\lambda_2}\right\} - \left\{\frac{4\pi n(T_{\min})d(T_{\min})}{\lambda_2}\right\} = 2\pi(m+0.5) + \sigma_1. \qquad (17)$$

Here, the unwrapped phase difference defined as $\phi_{12} = \Delta\phi_1 - \Delta\phi_2 = \pi$ as the temperature changes from $T_{\min}$ to $T_{\max}$. Note that the refractive index is assumed to be the same for wavelengths λ_1 and λ_2. Based on earlier reported experimental data for 6H-SiC in the near infrared band, this approximation is indeed valid, particularly when the two wavelengths are within 100 nm of each other as later shown in the experimental section of this report. Solving Eq. 16 and Eq.17 gives:

$$\lambda_2 = \lambda_1 \frac{2\pi m + \sigma_1}{2\pi(m+0.5) + \sigma_1}. \qquad (18)$$

Eq. 18 is used to select the second wavelength of operation for the proposed temperature sensor. Note that the additional phase shift σ_1 can be made zero by either selecting wavelength λ_1 such that the total phase shift is an integral multiple of 2π or by selecting the $T_{\min}$ and $T_{\max}$ such that σ_1 vanishes. In these cases with $\sigma_1 = 0$, Eq. 18 can be rewritten as:

$$\lambda_2 = \lambda_1 \frac{m}{m+0.5}. \qquad (19)$$

Note that the process of unwrapping the instantaneous phase $\phi(T)$ is for design purposes to verify proper unambiguous sensor processing conditions via dual wavelength selection. For a given temperature T, the proposed sensor must generate PD_1 provided P_m, $P_{m_{\max}}$, $P_{m_{\min}}$

optical power data set values at Eq. 19 based two pre-selected optical design wavelengths of λ_1

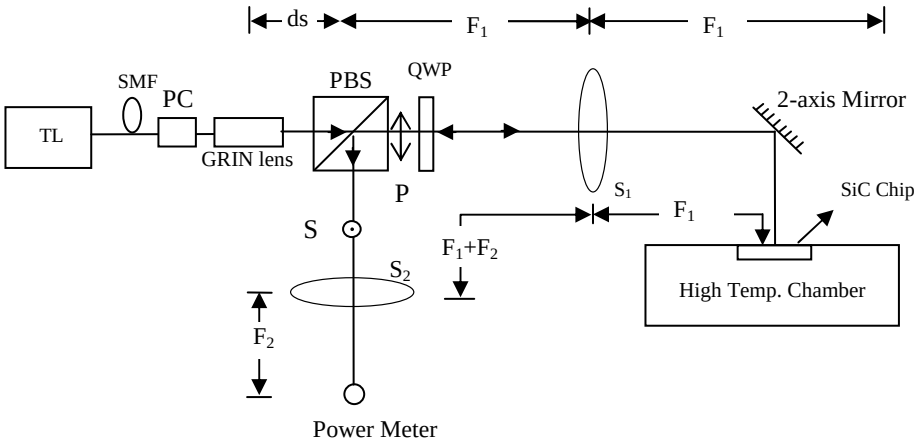

Fig. 2. Experimental set-up of demonstrated SiC-based minimally invasive optical sensor for extreme temperature measurements. TL: Tunable laser, PBS: Polarization Beam Splitter, QWP: Quarter Wave Plate, SMF: Single Mode Fiber. FL_1:Fiber Lens of Self Imaging Type with Half Self imaging Distance d_s where beam waist w_i is located ; S_1/S_2 Imaging Lenses of Focal Lengths F_1/F_2.

and λ_2. These power values are used to compute the instantaneous sensor phase values of $\phi_1(T)$ and $\phi_2(T)$ at the temperature T. This process is repeated for the entire temperature range of T_{min} to T_{max}. The instantaneous sensor phase difference $\Delta\phi(T) = \phi_1(T) - \phi_2(T)$ is calculated using the measured power data. A unique set of values of $\Delta\phi$ and $\phi_1(T)$ (or $\phi_2(T)$) exists for each temperature value eliminating the sensor power data ambiguity problem. Note that $\Delta\phi$ changes from $-\pi$ to π and completes many cycles as the temperature changes over the designated T_{min} and T_{max} range. During the sensor calibration process, the $\Delta\phi$, T, $\phi_1(T)$ (or $\phi_2(T)$) values are stored.

During sensor real-time temperature sensing operations, $\Delta\phi$ and $\phi_1(T)$ (or $\phi_2(T)$) are measured and matched to the unique T in the computer table that gives the same values for $\Delta\phi$ and $\phi_1(T)$ (or $\phi_2(T)$. Because today's commercial tunable lasers can be reset quickly (e.g., 1 ms) and accurately (e.g., within 0.01 nm), the proposed sensor can quickly provide the desired sensing parameter, i.e., temperature value where the SiC chip is remotely placed.

The Fig. 2 proof-of-principle sensor system is set-up in the laboratory to demonstrate the feasibility of the Fig. 1 design. A single SiC chip with no coatings present is placed and sealed in the experimental high temperature chamber based on induction heating. SiC used is 6H single crystal type with an average refractive index of 2.57. Using Eq. 8, the SiC chip front surface power reflection coefficient is calculated to be R = 0.193 implying that 19.3% of the input strike light on the chip take a first bounce off the chip to return to the photo-detector. On the other-hand, the light reflected first bounce back from the high temperature exposed rear surface of the SiC chip has a power reflection coefficient given by $R(1\text{-}R)^2$ = 0.125 or 12.5 % of the input laser light. Light returning to the photo-detector after a second bounce from the SiC chip high temperature interface is a much smaller $R^3(1\text{-}R)^2$ = 0.0047 or 0.47 % fraction of the original input laser light power. These first order calculations firstly imply that about 0.193+0.125=0.318 or approximately 32 % of the input light power will return from the SiC chip to strike the receive photo-detector. Second, the natural reflection properties for the SiC chip in air produces strong two beam interferometry that is expected to give a classic sinusoidal interference function.

Given the proposed sensor system's high efficiency (> 30%), a typical lower power 1.5 mW tunable laser source is used to launch light into the freespace optics coupled to the SiC chip. Specifically, the tunable laser has a wide 1500-1600 nm tuning range with a 0.01 nm tuning step and 0.0005 nm laser line-width. As seen in Fig.2., the tunable IR laser is collimated by a fiber Graded Index Rod (GRIN) lens with a d_s =6 cm half self-imaging distance and a 0.44 mm $1/e^2$

beam waist diameter or approximately 0.88 mm null-to-null beam size. The half-self imaging distance for the GRIN lens is where the Gaussian beam has a minimum beam waist and hence perfect collimation. A mechanical fiber-based polarization controller (PC) is used to produce the desired horizontal (or p) polarization light that exits the GRIN lens. This collimated light from the GRIN-lens passes through a PBS and only lets p- polarization light to pass through towards the SiC chip. Hence, the PBS works as a polarization noise filter to prevent any unwanted s or vertical polarization input light from reaching the SiC chip. A lens S_1 is placed between the GRIN lens and SiC chip to prevent large beam expansion. The distance between the fiber lens and imaging lens S_1 is 36 cm, where F_1=30 cm is the focal length of S_1 and 6 cm is from the GRIN half self-imaging distance. The distance between S_1 and SiC chip is 30 cm. The PBS is placed 15 cm before S_1. A QWP plate oriented at 45^0 to the horizontal or p-axis is placed between the PBS and S. The QWP converts the input linear p-polarization to circular polarization. As the SiC chip is a slightly birefringent material, using circularly polarized input light makes the sensing system polarization independent to the SiC chip rotational orientation. A F_2=10 cm focal length sphere S_2 is placed 25 cm from the PBS deflected port, and a large area Newport photo-detector with a 3 mm diameter is placed 10 cm away from lens S_2. All optics are anti-reflection (AR) coated for the near IR 1550 nm band.

With the given optical design in Fig.2, the Gaussian beam waist is formed on the SiC chip and the photo-detector. The light beam waist on the SiC chip is 0.88 mm null-to-null beam size while on the detector it undergoes a factor of 3 reduction in size to 0.29 mm due to ratio of focal lengths F_1/F_2 = 30 cm/10 cm. This demagnification of the beam size makes the sensor received beam easily located within the 3 mm diameter active area of the Newport free-space coupled detector. Unlike Fig.1, no active alignment mirrors are used because of the large area of the photo-detector size and the static and controlled environment of the SiC chip placed in the

high temperature test chamber. The chamber consists of a small (~7.9 mm diameter) hole in a stainless steel disk. The hole is covered with an induction heating coil powered by a 2.5 kW, 200 KHz, 240/380/480 V, 3-Phase alternating current power supply. The hole is sealed by placing the SiC chip on the opening with ceramic insulator rings that clamp the chip into position. The chip boundary is free to expand as it is not restricted in the sealing ceramic package. A steel disk is used to clamp the entire assembly from the top. The chip sits mid-way between the coil positioning to provide a uniform temperature to both sides of the chip. A salient feature of the chamber design is the reduced size of the steel cavity and hence small SiC chip exposure area which reduces stress variations across the exposed chip surfaces. There are no measurable optical reflections from the background of the chip as the steel cavity is terminated with a non-optical quality plate. The chip acts like a sealed optical window in the induction heating-based high temperature chamber. The chamber assembly has coarse translation stages to adjust the position of the laser beam with-respect to the SiC chip designated targeting zone. An external fixed mirror with fine x-y tilt control is used to make sure that the laser beam strikes the SiC chip at normal incidence. The 6-H SiC single crystal chip used has a 300 μm thickness and a 0.5 cm x 0.25 cm rectangular size. Reference temperature T of the SiC chip is monitored by a K-type thermocouple that is in contact with the SiC chip zone that is external to the test chamber but close (within 1 mm) to the probe optical beam. The thermocouple wire is inserted from the top steel plate through the ceramic rings and placed in contact with the top side of the SiC chip so it measures the heated chip temperature.

The freespace laser beam only interacts with a small 0.88 mm diameter central targeted region on the SiC chip. Hence, high quality (e.g., $\lambda/50$) optical flatness requirements are only subjected to a very small region of the chip front and back surfaces. Note that for proper in-line interferometry, the front and back surfaces of the SiC chip over the active laser region must be

parallel to enable high spatial coherence optical detection. In case, the surfaces are slightly non-parallel, a fringe pattern will appear on the detector surface. One can practically alleviate this issue by using a pin-hole placed in front of the photo-detector with the pinhole size much smaller that a single fringe cycle. In this way, high spatial coherence interferometric data can be taken as needed for proper sensor operations. Single crystal SiC is known as an excellent optical quality material and hence it is optically suited for the proposed minimally invasive sensor design. In our case, the used SiC chip surfaces were the desired quality and no pinhole use was required where the large area Newport point photo-detector acted as a natural pin-hole.

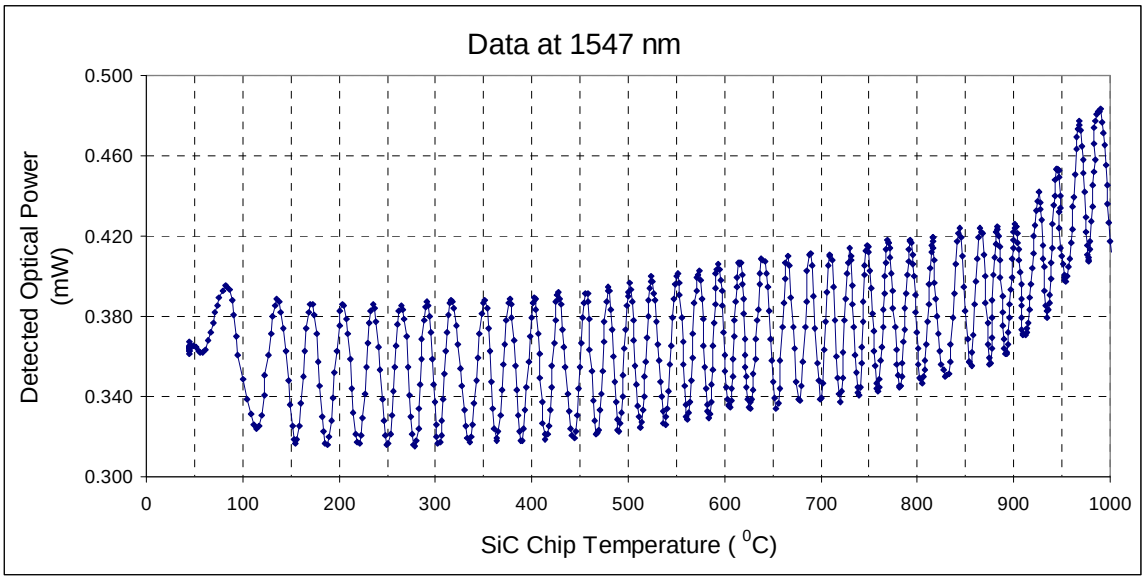

Fig. 3. Sensor provided raw optical power measurements at 1547 nm as the SiC chip temperature is raised to 1000^0C.

To demonstrate proof-of-concept sensor operations, an experiment is performed where the optical power by the sensor photo-detector is continuously recorded with the temperature chamber-based SiC chip heating from room temperature to 1000 ^{0}C. Here the chosen tunable laser wavelength λ_1 = 1547.0 nm, giving m = 37 optical power detection 2π cycles over the designed room temperature to 1000 ^{0}C sensor range (see Fig.3). Using the wavelength design

Eq. 20 with m = 37 and λ_1 = 1547.0 nm, one gets λ_2 = 1526.4 nm that should provide 37.5 optical power detection 2π cycles. To stay within experimental margin of error, a slightly higher value of λ_2 = 1530 nm is used such that one does not exceed the unambiguous range of π phase shift. The sensor photo-detector optical power and temperature data are recorded using a computer where 750 data sets are recorded as the SiC temperature is increased from near room temperature to 1000 ^{0}C using current heating of the test chamber. A better sensor resolution can be achieved over the same near 1000 ^{0}C range using more data samples per optical power cycle. In effect, the proposed sensor can zoom into a specific temperature zone and take extensive power data using accurate low noise optical power meters and fast sampling data analog-to-digital converters. Hence, accurate calibration of the sensor can be implemented using the proposed robust signal processing methods.

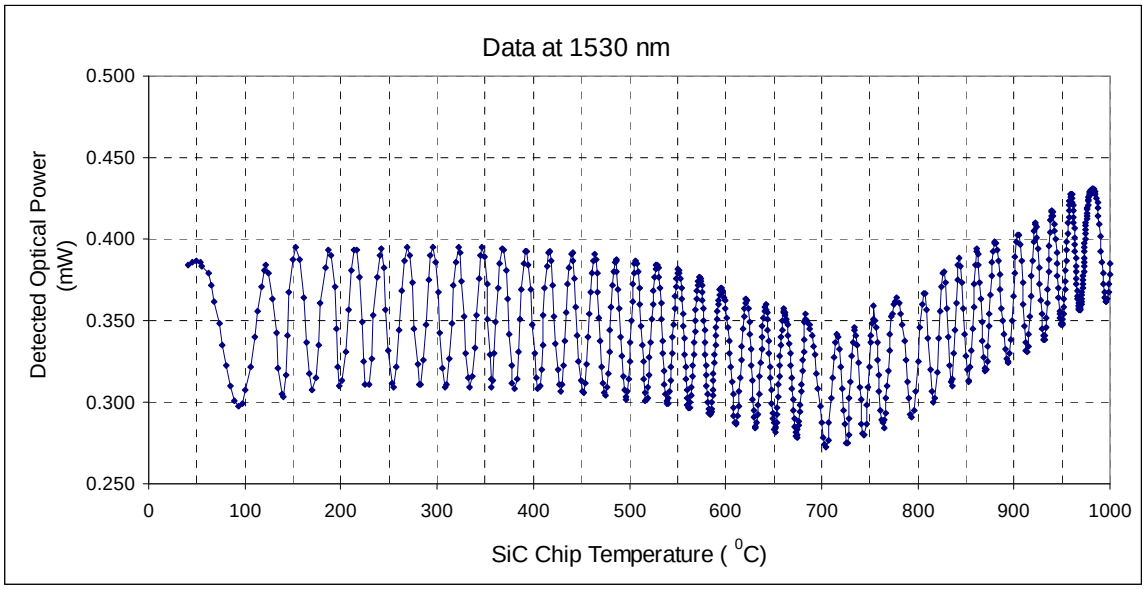

Fig. 4. Sensor provided raw optical power measurements at 1530 nm as the SiC chip temperature is raised to 1000^{0}C.

Fig. 3 and 4 show the raw sensor optical power data in mWs obtained for two different wavelengths using the computer automated power and temperature measurement set-up. Note that over the 1000 °C temperature measurement process, as expected, the power maximum and minimum values per cycle change depending on the time varying experimental conditions such as mechanical vibrations, thermal gradients, and air currents that affect the optical returning beam to the photo-detector. Because the present experiment is characterizing the proposed optical sensor, one can store the optical power data over the entire temperature band and then process optical power data per cycle to produce the required normalized plot of the cosine of the chip optical phase ϕ versus temperature.

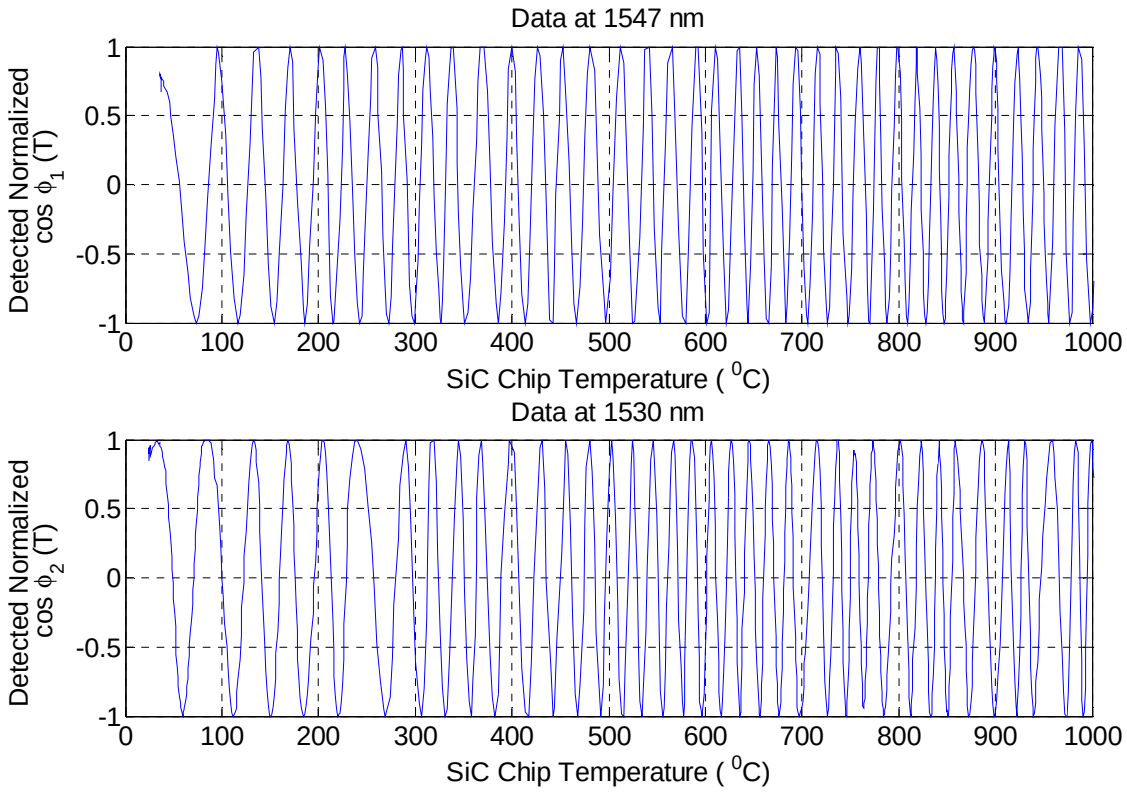

Fig. 5. Sensor provided normalized $cos\{\phi_1(T)\}$and $cos\{\phi_2(T)\}$ measurements at 1547 nm and 1530 nm as the SiC chip temperature is raised to 1000^0C.

Fig. 5 shows this normalized $cos\{\phi(T)\}$ plot obtained for the two wavelengths of 1530 nm and 1547 nm. Fig. 3 and 4 show the sensor's data ambiguity issue as the same values of $cos\{\phi(T)\}$ occur for many different values of temperature. To check the elimination of the data ambiguity in the gathered data set, one simply takes into consideration the number of cycles recorded and adds 2π after each cycle to get an unwrapped phase value. This mathematical operation can be done in software and these unwrapped $\phi(T)$ phase value results in radians for the Fig. 3 experimental data are shown in Fig. 6 and Fig. 7.

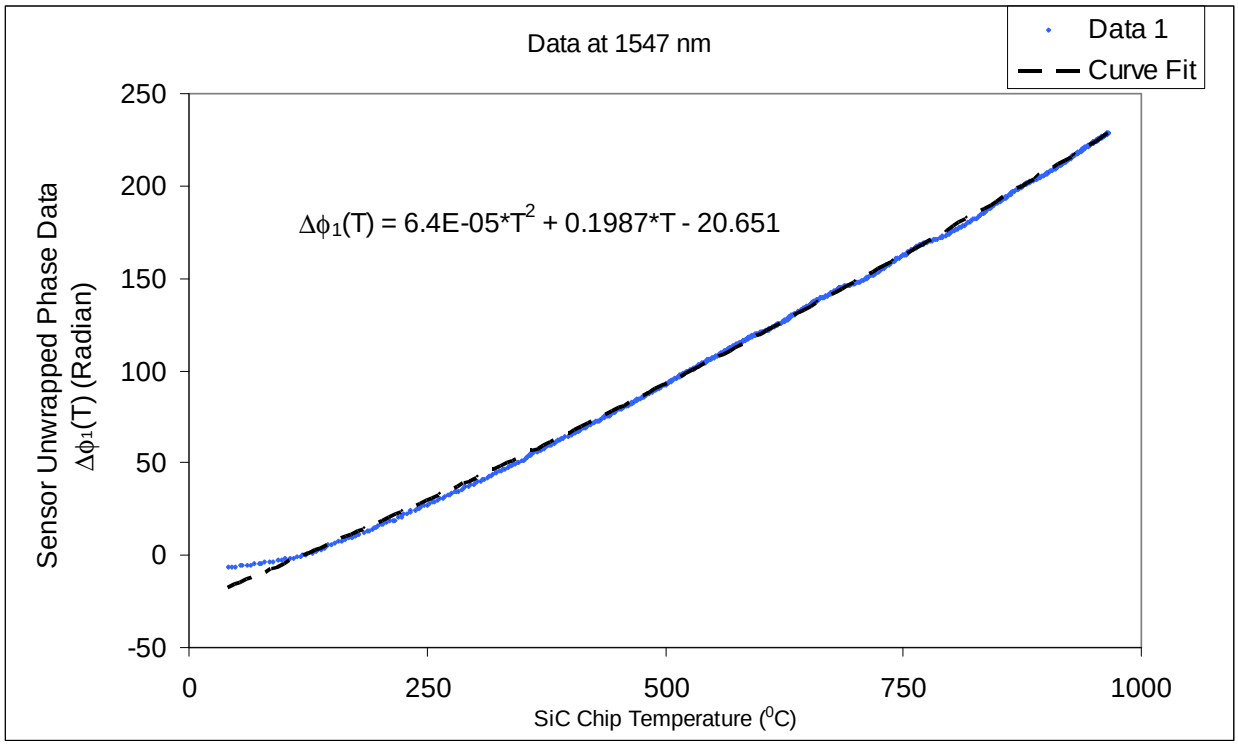

Fig. 6. Sensor Unwrapped Phase Shift Data $\Delta\phi_1(T)$ in Radians versus SiC Chip Temperature (^{0}C) with data taken at 1547 nm. A weak quadratic curve fit is achieved for this data.

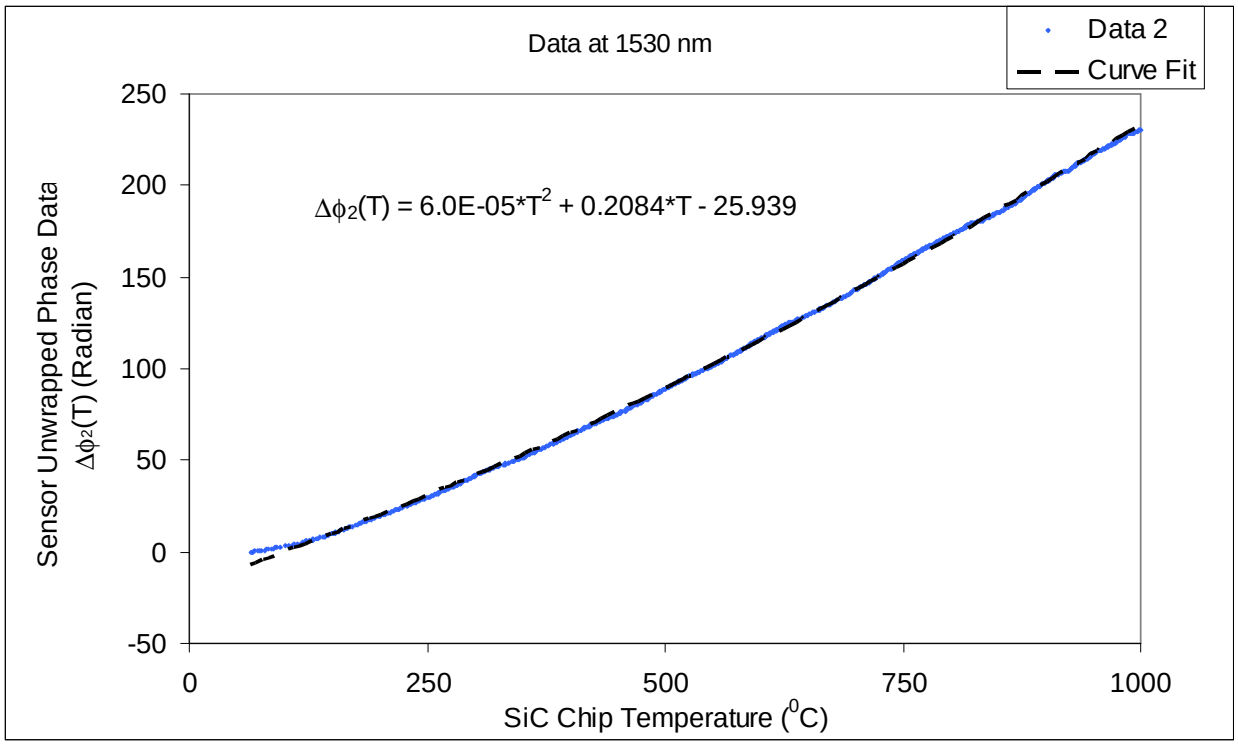

Fig. 7. Sensor Unwrapped Phase Shift Data $\Delta\phi_2(T)$ in Radians versus SiC Chip Temperature (^{0}C) with data taken at 1530 nm. A weak quadratic curve fit is achieved for this data.

Note in Fig. 5 for the room temperature to 1000 ^{0}C range, the optical power for 1547 nm sweeps 37 cycles while for 1530 nm sweeps the expected almost 37.5 cycles. Hence experiments conducted at wavelengths of λ_1= 1547 nm and λ_2= 1530 nm give the desired unwrapped phase values $\Delta\phi_1(T)$ and $\Delta\phi_2(T)$, respectively. Next, the curve fits to the $\Delta\phi_1$ and $\Delta\phi_2$ data are used to calculate $\phi_{12} = \Delta\phi_1(T) - \Delta\phi_2(T)$ and ϕ_{12} is plotted in Fig. 8. Note that this unwrapped phase difference $\phi_{12}(T)$ is slightly less than π radians for the temperature range from 35^{0}C to 1000 ^{0}C, as needed for the implemented sensor design. Thus the data in Fig. 8 does show how the 37 ambiguous cycles of phase data versus temperature have been converted to almost a single unambiguous π cycle making the gathered sensor data appropriate for processing.

For real time temperature measurement via the sensor, the two wavelength calibration data is used, hence eliminating the need to unwrap the phase data from the sensor. The instantaneous phase difference unlike unwrapped phase difference takes values from $-\pi$ to π.

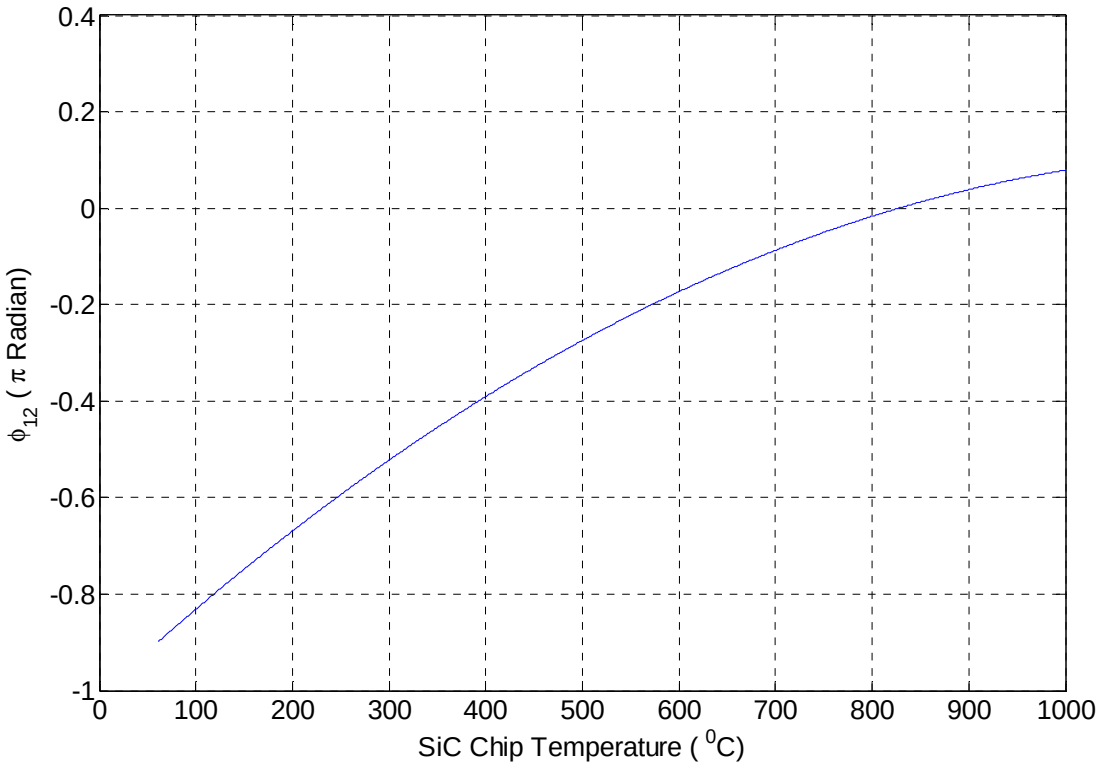

Fig. 8. Unwrapped Phase Shift Difference $\phi_{12} = \Delta\phi_1 - \Delta\phi_2$ data for the two wavelengths used for the sensor operations.

This instantaneous phase difference $\Delta\phi(T)$ and the corresponding instantaneous phase $\phi_1(T)$ (or $\phi_2(T)$) produces a unique data pair and when compared to the stored calibration data set provides a unique unambiguous temperature value. To visually illustrate this novel ability of the sensor signal processing, a three dimensional (3-D) plot with axes of $\Delta\phi(T)$, ϕ_1 , and T is generated using measurements for the two wavelengths at the room temperature to 100 ^{0}C temperature range.

This curve shown in Fig. 9 shows a helical spring like behavior where for every set of values of $\Delta\phi$ and ϕ_1, there is only one value of the temperature corresponding to that data set. Note that the extended sensor experimental calibration curve to 1000 ^{0}C is again a spiral curve (like Fig. 9) with changing pitch according to the changing period of the chip OPL parameter variations. Here again there is no ambiguity in the temperature measurements provided by the proposed sensor. The real-time sensor temperature resolution depends both upon the quality of the stored calibration optical power data and the real-time optical noise in the sensor system. Fundamentally, the proposed sensor determines the real-time temperature value by taking real-time optical power measurements and processing this optical power information to compare with previous calibration data. To insure high fidelity calibration data, the measured near sinusoidal optical power variation with temperature change must be sampled at a very high frequency (e.g., 50 X) compared to the fundamental frequency.

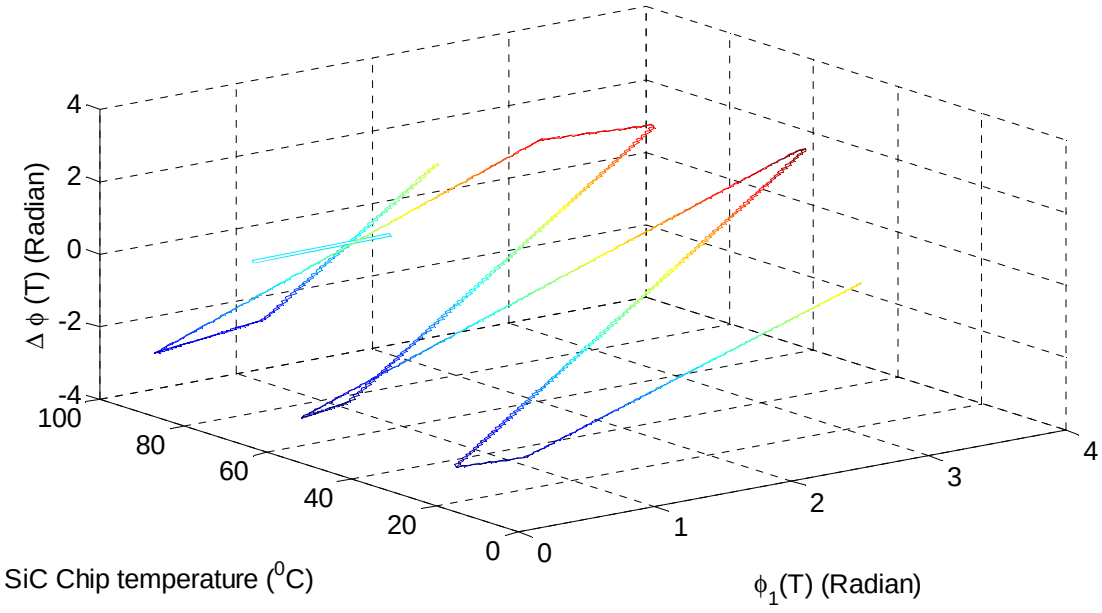

Fig. 9. Three dimensional (3-D) representation of the sensor calibration chart for the unambiguous instantaneous temperature measurement via the demonstrated sensor from room

conditions to 100 ^{0}C. This 3-D plot uses the instantaneous phase difference data $\Delta\phi(T)$, instantaneous phase shift $\phi_1(T)$, and given temperature T.

In addition, the optical detector and power meter noise floor should enable low quantization errors to enable high dynamic range, e.g., > 40 dB or > 10,000:1 optical power gray-scale measurements. Recall that this calibration and real-time power data is used to compute both the instantaneous phase and instantaneous phase difference values that then determine the temperature value. Hence, the resolution of the instantaneous phase difference value indeed will impose a limit on the sensor temperature resolution when the proposed phase shift-based processing is used to determine the temperature. For the present sensor proof-of-concept calibration, 750 data values are taken from room temperature to 1000^{0}C. In theory and to a first approximation, the average sensor resolution based on the given data sampling range can be estimated to be approximately 970 ^{0}C / 750 ~ 1.3 ^{0}C. It is interesting to note that the measured temperature period of the optical power cycle decreases with increasing temperature, beginning near the 30^{0}C and approaching 20^{0}C near the 1000 ^{0}C level. This implies that higher optical power measurement sampling rates are required at higher temperatures of the calibration process if the same temperature sensing resolution has to be maintained. Today, commercially available power meters can easily measure optical power accurately from milli-watts to nano-Watts (nWs) or a 60 dB gray-scale range. Therefore, optical power measurement instrumentation can help reduce computational errors in the sensor processing. Furthermore, the laser power can be increased to any desired higher value so that the minimum power change per degree temperature change is significantly higher than the detector noise.

Thus, the proposed minimally invasive single crystal SiC chip-based optical sensor when used with the proposed signal processing can provide true unambiguous temperature

measurements for extremely high temperatures that the single crystal SiC can naturally withstand in environmentally unfriendly settings. Quantitatively, the effect of temperature on the proposed single crystal SiC-based optical sensor has been investigated and results for the used 300 μm thick SiC chip showed a 2π OPL change (or $\phi(T)$ phase shift change) for an average temperature change range of 30 to 20 ^{0}C. More specifically around room temperature, a 30 ^{0}C change causes a 2π optical power cycle. Later at the extreme 1000 ^{0}C temperature, the SiC refractive index and thickness are at a higher value causing a 2π optical power cycle for a smaller 20^{0}C change in temperature. These results also point out that the proposed SiC sensor requires calibrated data for proper operations over a wide sensing parameter range. Another point to note is that the sensor performance can be considered coded in temperature period, i.e., a given temperature value is always within a specific sensor temperature period for a 2π optical power cycle. This particular effect can also be used to extend the unambiguous temperature detection range of the proposed sensor. Starting with the defined sensor OPL parameter expression at a λ_1 wavelength and temperature T :

$$\phi(T) = \left\{ \frac{4\pi n(T) d(T)}{\lambda} \right\}. \quad (20)$$

Taking the derivative of both sides of Eq.20gives:

$$\frac{d}{dT}\{\phi(T)\} = \frac{4\pi}{\lambda}\left[d(T)\frac{\partial}{\partial T} n(T) + n(T)\frac{\partial}{\partial T} d(T) \right]. \qquad (21)$$

The rate of change of phase or $d\phi(T)/dT$ governs the variation of the temperature change causing a full power cycle. If this rate remains constant, there is no variation in temperature change that produces a full optical power cycle.

G.2. Pressure Sensing Fundamentals

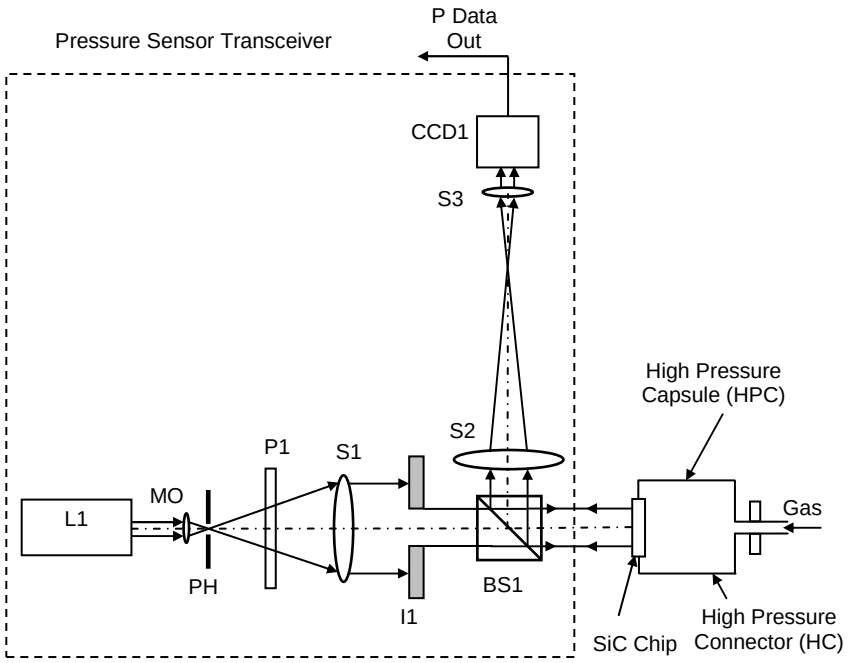

Fig. 10: Proposed SiC-chip based wireless optical pressure sensor.

Fig.10 shows the proposed wireless pressure sensor concept that uses a remotely placed all-passive optical sensor capsule made of a single crystal SiC chip acting as the capsule window and a pressure sealed capsule assembly made of a suitable high pressure high temperature material such as a ceramic (including SiC forms, e.g., sintered SiC) or high pressure stainless steel. The capsule has a high pressure connector that interfaces to the high pressure hot gas (or fluid) flow system that is linked to the high temperature high pressure hot gas flow system such as a fossil fuel plant under test. The SiC optical window sits in a specially designed sealed pressure seat that creates the desired high pressure boundary conditions for the deployed SiC chip. The Fig.10 sensor operates as follows. The input laser beam from a laser L1 is passed through an expansion-filter system of microscope objective lens MO and pin-hole PH. The cleaned and expanded beam is vertically polarized using a polarizer P1 and then collimated using

a biconvex lens S1. The portion of the light beam that transmits through the Beam Splitter BS1 hits the SiC chip seated in the high pressure capsule with a sealed circular boundary. The size of the beam hitting the SiC chip is controlled by an iris I1 that is placed between S1 and BS1. Under ambient atmospheric pressure conditions (atmospheric pressure or 1 atm), the reflection from the front and back surfaces of the SiC chip give a phase map that represents the relative optical path length (OPL) differences between the two surfaces. This phase information is seen on a 2-D CCD detector CCD1 in the form of fringes. The initial fringe pattern can be written as $I_i(x, y)$ as the initial phase map of a given SiC chip. For a perfect flatness parallel faces chip, one would not observe any fringes; just a gray-scale uniform optical power level. Imaging lenses S2 and S3 are used to form a 1:1 imaging system between the SiC chip and the CCD. For laboratory experiments discussed later, a compressed air cylinder is connected to the pressure capsule via a manual regulator to control the pressure inside the capsule relative to the external ambient atmospheric pressure.

Key principle of operations of the proposed sensor is the global sensing of the chip deformation due to pressure. As the pressure in the capsule increases with respect to the external ambient pressure, the SiC chip undergoes a mechanical deformation and assumes a convex mirror position for the striking incident collimating beam. In effect, the SiC convex mirror acts as a diverging refractive weak lens that produces a beam expansion for the reflected incident beam. Hence, one should expect a magnification of the beam received at the remote CCD. However, given the Fig. 10 design uses a 1:1 imaging system between the chip and the CCD, the chip convex mirror-like deformation combined with the inverting imaging system produces a reduction in the beam size at the CCD with increasing pressure. Hence by monitoring the optical beam image size on the CCD, a pressure measurement can be remotely achieved. Because CCD's are highly light sensitive devices and single crystal SiC is sufficiently (e.g., > 10 %)

reflective (e.g., > 10 % reflectivity) for visible laser wavelengths, only a low power (e.g., < 10 mW) laser is required for the proposed sensor design. Do note that for highly remote distance operations when transceiver and capsule distances exceed for example 1 m, lenses S2 and S3 can be removed. In this case, the received beam expansion is monitored to access pressure. For the present paper, the basic Fig.10 design is investigated as appropriate for short distance remoting as in a controlled laboratory environment. The SiC chip undergoes a mechanical deformation as the pressure in the capsule is increased. In order to evaluate the nature and extent of this deformation, a theoretical analysis of the mechanical response of the SiC chip within the pressure capsule becomes essential. The nature and extent of this mechanical response is in turn responsible for the optical response of the sensor system.

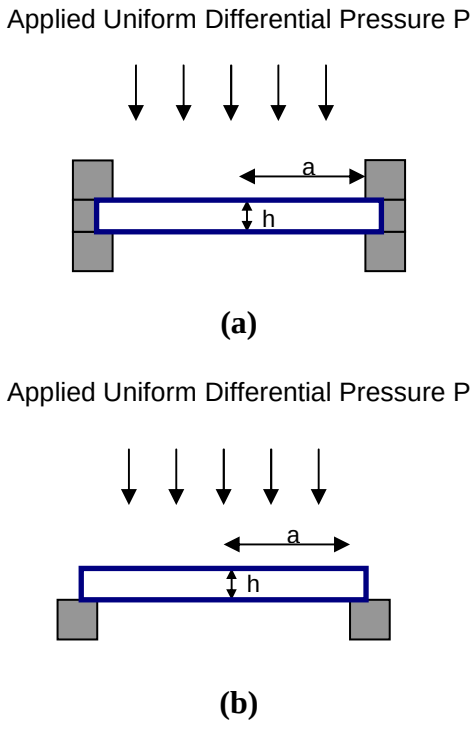

Fig. 11: Shown are the two Key Mechanical Models, (a) Clamped Edge model and (b) Simply Supported model, used to analyze the SiC Chip mechanical deformation behavior when seated in the proposed high pressure capsule.

Hence, for optimal pressure sensor design a mathematical relationship between the mechanical and optical responses within the sensor system needs to be established. The mechanical response of the deployed 6H-SiC chip is dependant on its mounting in the given test pressure capsule. Specifically, the mounting method defines the boundary condition necessary for solving the equations that give the amount of deflection of the SiC chip which it turn determines the power of the pressure sensitive convex mirror behavior of the chip.

Considering the design of the given pressure capsule SiC chip seat , two major methods, namely, a circular chip with ‘Clamped Edges’ and circular chip with ‘Simply Supported Edges’ are analyzed for the test capsule (see Fig. 11(a),(b)). In effect, the SiC chip experimental mounting method, shown later for the test capsule in this study, results in a hybrid-solution of the mentioned methods. Furthermore, the deflection analysis is sub-divided under two regimes of small and large deflection analysis. The small deflection regime is defined by the condition that the maximum deflection should be less than half the thickness of the chip [20]. Specifically, the region in the middle plane of the sensor chip, undergo small displacements perpendicular to the direction of the plane thus forming the middle surface of the chip. When these displacements are small in comparison with the thickness of the chip, the strain of the middle plate can be neglected and analysis is in the small deflection regime. When this is not true, the analysis is extended to include the effect of strain of the middle plane of the chip. This large deflection regime analysis gives deflection and stress results that deviate from the small deflection regime. As shown later via the experiments, the proposed pressure sensor operates well within the small deflection regime of the utilized 6H-SiC chip. Also note that failure stress analysis of the SiC chip is essential for a robust sensor design. Hence, the maximum stress values generated for all pressure cases have to be evaluated. Proper design requires working with pressures that generate maximum stress values that are less than the failure yield stress value for 6H-SiC. This pressure-

limited operation ensures the reliable and repeatable performance of the SiC chip and hence the proposed wireless optical pressure sensor.

Under uniformly distributed applied pressure, a circular sensor chip with clamped edges (see Figure 11(a) exhibits deflection according to the following classic expression [20]:

$$w(r) = \frac{P(a^2 - r^2)^2}{64D}, \tag{1}$$

where *w(r)* is the bend in chip at a certain radius *r*, *P* is applied differential pressure between the two isolated sides of the chip, '*a*' is the radius of the chip, 'ν' is the chip material Poisson's ratio and *D* is its rigidity constant. *D* is defined as:

$$D = \frac{Eh^3}{12(1-\nu^2)}, \tag{2}$$

where *'E'* is the chip material modulus of elasticity and '*h*' is the thickness of the chip. The maximum deflection is at the center of the chip and is given by:

$$w_{\max} = \frac{Pa^4}{64D}. \tag{3}$$

The maximum stress caused by pressure is at the boundary of the chip given by the equation:

$$(\sigma_r)_{\max} = \frac{3Pa^2}{4h^2}. \tag{4}$$

For a circular sensor chip with supported edges (see Figure 11(b)), the deflection under uniformly distributed applied pressure is given by the following expression [20]:

$$w(r) = \frac{P(a^2 - r^2)}{64D}\left(\frac{5+\nu}{1+\nu}a^2 - r^2\right). \tag{5}$$

The maximum deflection is at the center of the chip and is given by:

$$w_{\max} = \frac{Pa^4}{64D}\left(\frac{5+\nu}{1+\nu}\right). \tag{6}$$

The maximum stress in the supported chip caused by pressure is at the center of the chip given by the equation:

$$(\sigma_r)_{\max} = \frac{3Pa^2(3+\nu)}{8h^2}. \qquad (7)$$

Now consider the proposed case of a 6H-SiC chip with thickness *'h'* of 280 µm, radius *'a'* of 2.5 mm, Poisson's ratio *'ν'* of 0.16 and Young's Modulus *'E'* of 415 GPa [21-22].

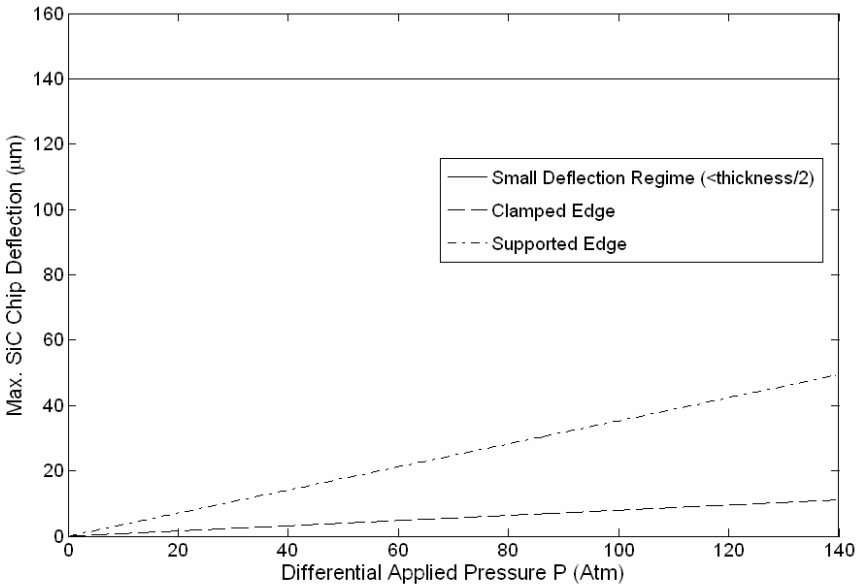

Fig. 12: Plot shows maximum SiC chip deflection 'w_{max}' (at the center of the chip) under applied pressure for the Clamped Edge and Supported Edge boundary condition models. The chip boundary diameter was taken to be 5 mm.

Fig. 12 shows the expected deflection produced for 6H-SiC sensor chip with the applied differential pressure in the pressurized capsule. The maximum deflection of the sensor chip, with a 5 mm diameter pressure boundary and thickness of 280 µm, is expected to be well within the small deflection range (i.e., < Thickness/2= 140 µm) at 100 atmospheres.

The expected stress produced for 6H-SiC sensor chip with the applied differential pressure in the pressurized capsule is shown in Fig. 13. Using a 1 GPa yield stress [23] (approx.) for the 6H SiC chip, the demonstrated wireless pressure sensor is expected to work safely up to a pressure of 100 atm.

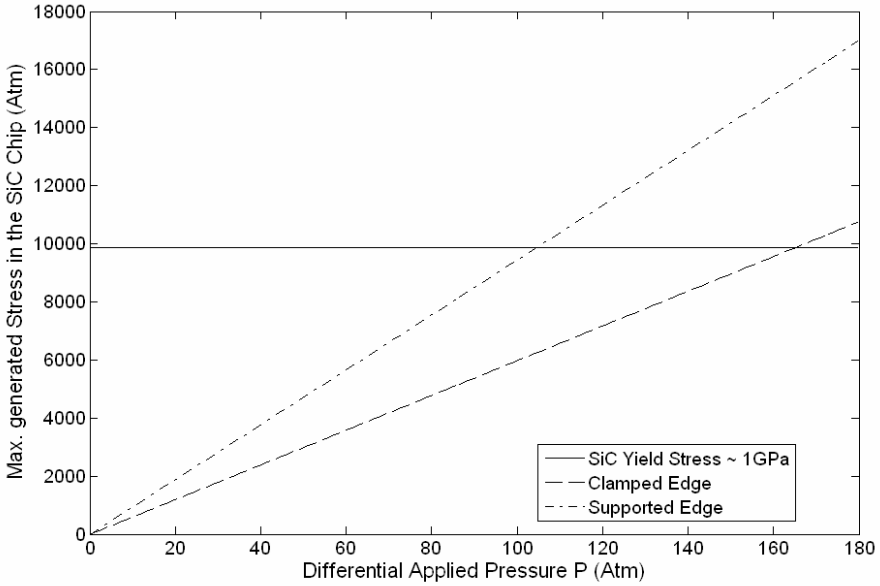

Fig. 13: The expected stress produced in SiC sensor chip of 5 mm diameter and 280 μm thickness.

Comparing the two Fig. 2 SiC chip seating setups in the small deflection regime, the supported edge chip seating case gives approximately 3.7~5 times larger deflection than the clamped chip case (see Fig. 12) but then it also gives 1.5~1.75 times higher maximum stress value (see Fig. 13). Since the experimental set-up to seat the SiC chip in the high pressure cell utilized in the present study is a hybrid of the two cases, the maximum stress value is expected to be in a range whose limits are defined by the stress values given by the mentioned two cases. Same discussion holds true for the maximum deflection of the SiC chip. Note that in the large deflection regime, exact analytical solutions are not available and only approximate analytical solutions can be utilized. However, numerical methods and simulation tools (like Finite Element

Method Software) can provide more exact solutions for the plate/chip deflections and stress values. After deflection according to equations (1) or (5) under small deflection regime, the surface of the SiC chip and hence the optical response of the SiC chip can be approximated by a weak lens. Geometrical analysis for weak lensing mirror optics (i.e., when lensing mirror radius of curvature R << Lensing mirror Central Thickness w_{max}) can be carried out to show that the SiC weak convex mirror focal length fm in cm is given by [24]:

$$f_m = \frac{R}{2} = \frac{w_{\max}^2 + a^2}{4w_{\max}^2 \times 10^4} cm, \qquad (8)$$

where w_{max} is the SiC chip central position maximum displacement with applied differential pressure P and a is the radius in microns of the SiC chip pressure boundary. Using Equations (3), (6), and (8), and a pressure boundary of a= 2.5 mm, Table 1 gives the theoretically expected maximum chip central deflection and equivalent weak focal length values for the SiC chip under specific varying pressure values. These pressure values were implemented later in the experiment. In addition, Fig.14 shows the theory predicted focal length change for the SiC weak mirror for a broad range of pressures.

Table 1: Theoretical Central Deflections and Focal Lengths of the SiC Chip Convex Mirror versus Pressure.

Differential Pressure P		**Model 1**		**Model 2**	
		Supported Sensor Chip		**Clamped Sensor Chip**	
(psi)	**(atm)**	**Chip Central Deflection w_{max} (μm)**	**Convex Mirror Focal Length f_m (cm)**	**Chip Central Deflection w_{max} (μm)**	**Convex Mirror Focal Length f_m (cm)**
0	0	0.000	∞	0.000	∞
200	13.61	4.804	32.53	1.080	144.68
300	20.41	7.206	21.68	1.620	96.45
400	27.21	9.608	16.26	2.160	72.34
500	34.01	12.010	13.01	2.699	57.87
600	40.82	14.412	10.84	3.240	48.23

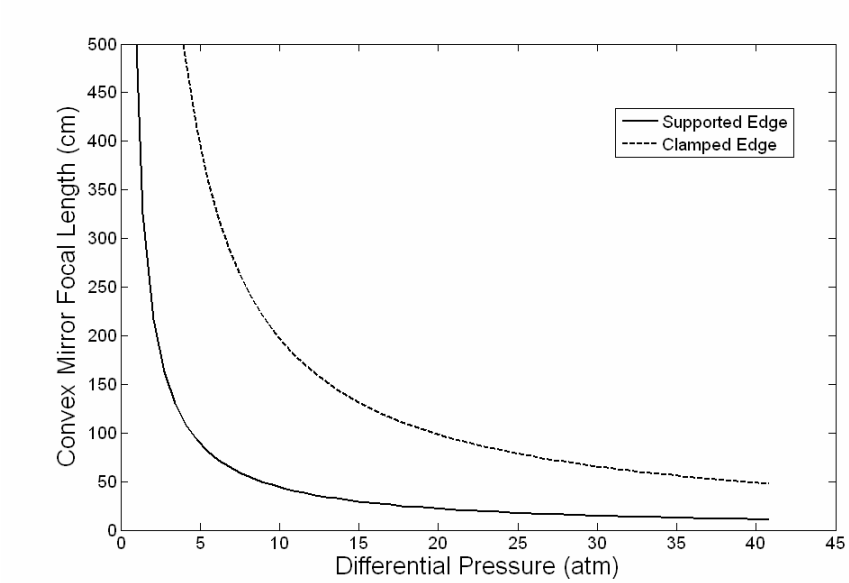

Fig. 14: Plot shows the effective theoretical focal length 'f_m' of the SiC chip acting as a convex mirror due to applied pressure. The focal length decreases as the differential pressure is increased.

Recall that the SiC chip acts as a weak convex mirror (equivalently, a weak concave lens) within the proposed Fig.10 wireless optical sensor setup containing S2/S3 1:1 imaging system. The S2 and S3 lenses have focal lengths F_2 and F_3, respectively ($F_2 = F_3 = F$). When the SiC chip experiences no differential pressure (P=0), it acts like a flat mirror and S3/S4 lenses form a 1:1 imaging system with magnification M=1. As P increases, the SiC chip starts acting like a convex mirror (or concave lens) with a long negative value focal length. It is well known that the equivalent focal length f_e for two lenses (convex lens focal length F_2 and mirror focal length f_m) placed L apart is given by:

$$f_e = \frac{F_2(L - f_m)}{L - (F_2 + f_m)}. \qquad (12)$$

Hence, the SiC chip weak concave lens in combination with the first imaging lens S2 forms an equivalent imaging lens with a new f_e focal length. With F_2=F and L=F, and considering weak lensing conditions which are true for the proposed SiC pressure sensor, the new pressure

dependent optical linear demagnification M (f_m is a negative value) for the imaging system can be approximately written as:

$$M = \frac{F_3}{f_e} = \frac{F}{f_e} = \frac{f_m}{(f_m - F)} = \frac{1}{1 - F / f_m}. \qquad (13)$$

As M can be measured by computer-based image processing of the CCD acquired images in Fig.10 and F is known, f_m can be calculated. Furthermore, as f_m is related to w_{max} of the SiC chip (See Eqn.8) and w_{max} is related to the differential pressure P in the capsule (see Eqns. 3 & 6), the measured pressure P can be calculated. As actual experimental conditions for the SiC chip seating can be a combination of the clamped and supported chip deformation models, each proposed wireless sensor should be calibrated using a state-of-the-art pressure gauge. In effect, a sensor calibration table should be deployed that stores precision taken pressure values and their corresponding M values provided by the wireless optical pressure sensor. In this way, any non-linear effects within the pressure versus M function can be calibrated into the sensor measurements leading to reliable and accurate pressure measurements.

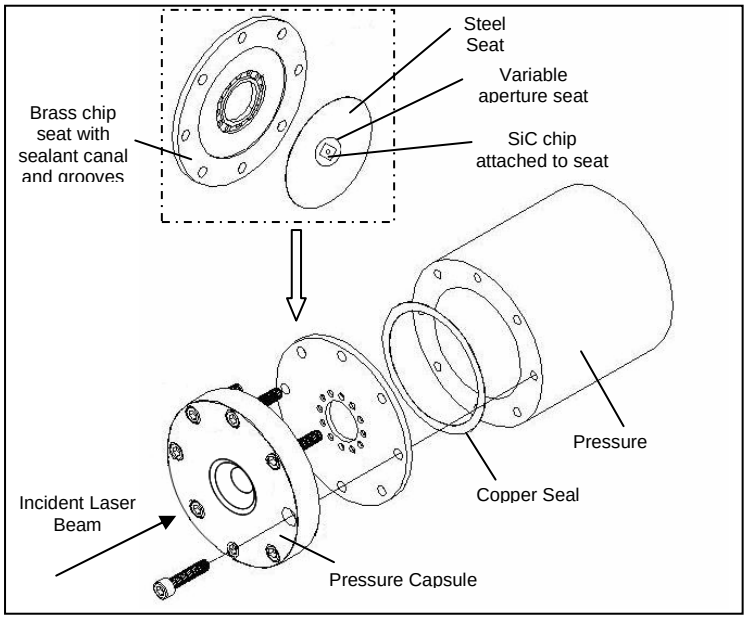

Fig. 15: Experimental design used for seating the SiC chip in the high pressure capsule.

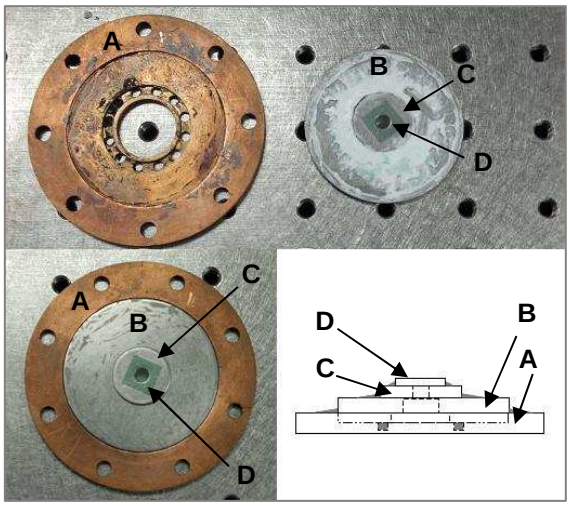

Fig. 16: Snap shot of the experimental seating components and their arrangements used for seating the 6-H SiC chip in the high pressure capsule. Components in photograph are labeled as: A: Brass chip seat holder with sealant canal and grooves; B: Steel seat; C: Aperture seat (washer) and D: SiC chip.

In order to study the pressure measurement aspects of the proposed Fig.10 wireless sensor, a high pressure stainless steel capsule is fabricated as shown in Fig. 15. Fig.16 shows the manner in which a square 1 cm x 1 cm SiC chip is seated in the pressure capsule. The variable aperture seat (washer) used has a 5 mm diameter and creates the circular pressure boundary on the chip. The washer is attached to the steel seat by a GE RTV 102 silicone rubber adhesive sealant with operational temperature range of – 60 °C to 204 °C. The SiC chip is attached to the washer using a layer of the same sealant. The sealant is filled in the canal of the brass seat so it strongly holds on to the steel seat. A layer of the sealant was also applied at the edges of the two seats to avoid any leaks. Do note that for high temperature or temperature independent pressure sensor operations, a modified SiC seating design should be utilized to match seat and chip material Thermal Coefficient of Expansion (CTE) values to avoid temperature dependent global

chip deformation. This aspect will be pursued in future advanced stage work. To enable the present Fig. 10 sensor design, a 10 mW 633 nm (red wavelength) linear polarization He-Ne laser is used as the source L1. The expansion-filter system utilizes a 10X MO lens and 10 μm PH. The collimating lens has a focal length of 15 cm.

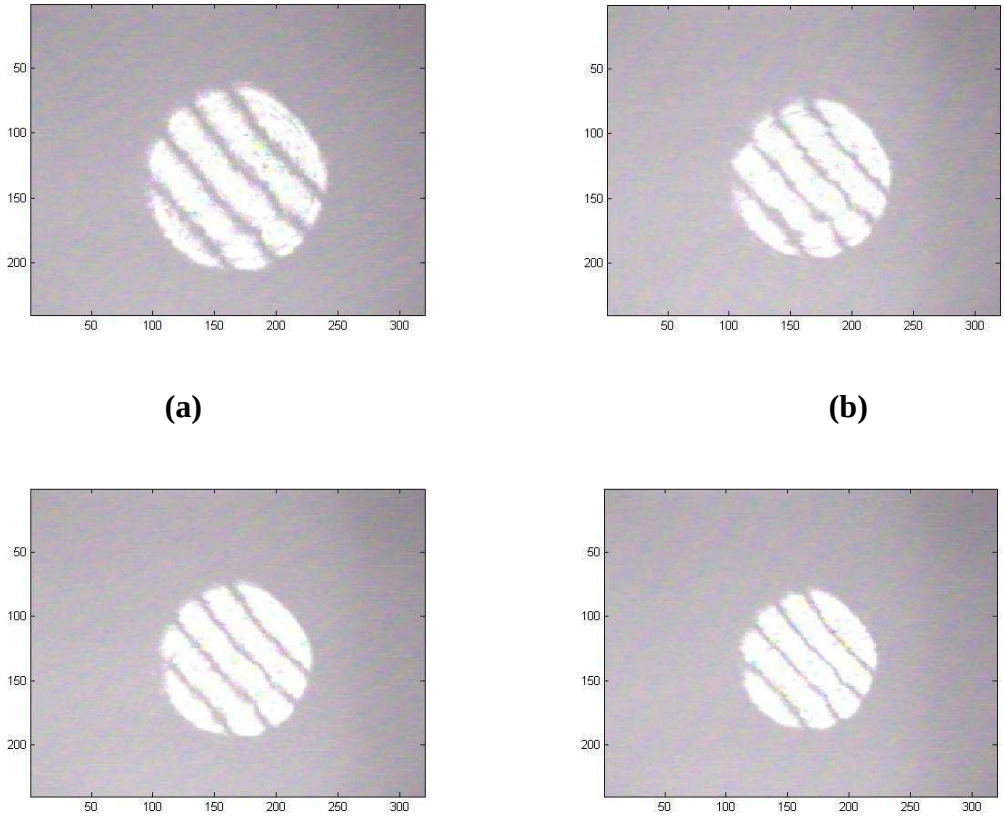

Fig. 17: SiC chip-based pressure system $I_i(x,y)$ optical images produced for (a) 0 atm, (b) 13.6 atm (200 psi), (c) 27.2 atm (400 psi), and (d) 40.8 atm (600 psi) high differential pressure conditions in the pressure capsule. Photo both axes dimensions in CCD pixel count.

The sealed circular boundary of the SiC chip for the experiment is of ~ 5 mm diameter. Imaging lenses S2 and S3 have 10 cm focal lengths forming a 40 cm path 1:1 imaging system between the SiC chip and CCD. The temperature condition during the experiment is the ambient 26 ºC room temperature. The manual regulator connected to the compressed air cylinder is used

to control the pressure inside the capsule relative to the external ambient 1 atm pressure. As shown in Fig. 17, as the pressure in the capsule increases above 1 atm, the differential pressure P on the SiC chip produces an increasing convex mirror chip deformation of the initial pattern $I_i(x,y)$ thus producing a pattern reduction in size. Fig. 17 shows the set of images from the wireless pressure sensor where the initial fringe pattern size decreases with increasing capsule differential pressures up-to 40.8 atm (1 psi = 0.068 atm). A quantization of the image reduction versus applied differential pressure P in the capsule for P taken up-to 40.8 atm is shown in Table 2 giving the experimentally measured values for M versus P.

Table 2: Experimental Optical Image Size vs. Capsule Differential Pressure P.

Differential Pressure P		**Image Size**	**Measured Magnification**
(psi)	**(atm)**	**(CCD pixels)**	**(M=Image Size/147)**
0	0	147	1.00
200	13.61	135	0.92
300	20.41	130	0.88
400	27.21	125	0.85
500	34.01	117	0.80
600	40.82	112	0.76

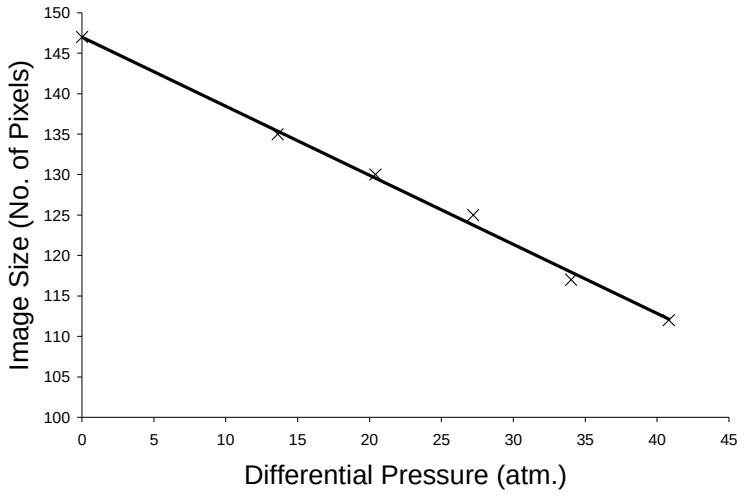

Fig. 18: Plot shows demagnification of incident beam size as it reflects from the SiC chip under pressure acting as a weak convex mirror coupled to a 1:1 image inversion system.

Fig. 18 connects the discrete experimental data to show a plot of differential pressure P on SiC chip versus image size given by pixel count. These results show a linear behavior of the applied differential pressure P versus the measured optical parameter of image size. Sensor pressure resolution is given by the inverse of the slope of the plot in Fig. 18. This plot indicates a current experimental resolution of 1.17 atm calculated as 40.82 atm/ [(147-112) pixels]. Resolution measurement is restricted by the pixel size in the deployed CCD. Here 147 pixels of the CCD = 5 mm real size using the 1:1 imaging approach.

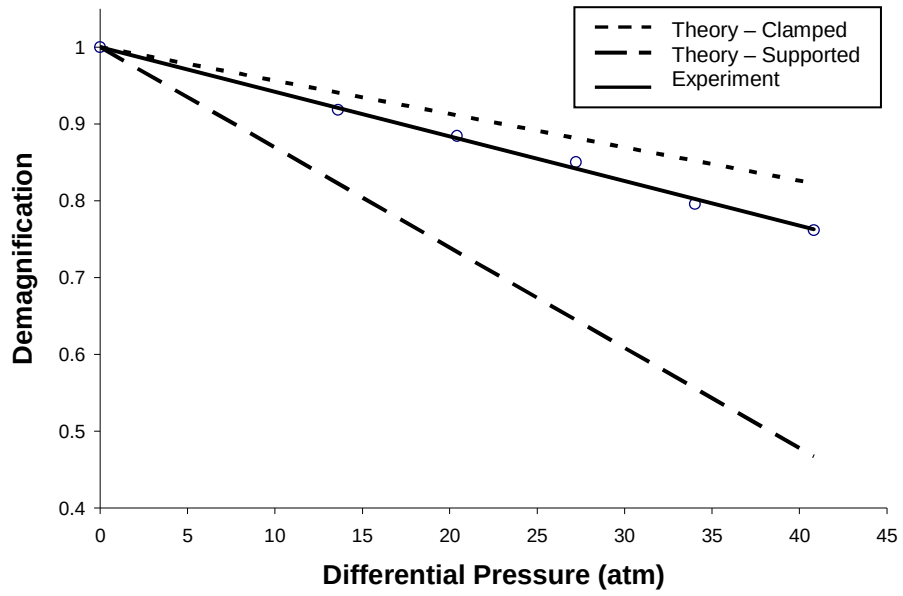

Fig. 19: Plot shows the experimental beam demagnification along with the theoretical demagnification for Clamped and Supported sensor chip models. The behavior of the chip shifts from clamped model towards supported model as the pressure increases.

For comparison and sensor design accuracy, Fig.19 shows plots for the experimentally detected image magnification M versus pressure P for the studied wireless sensor versus the theoretical design plots.

G.3. Gas Species Sensing Fundamentals
(Kar LAMP Lab. Provided Data and Information)

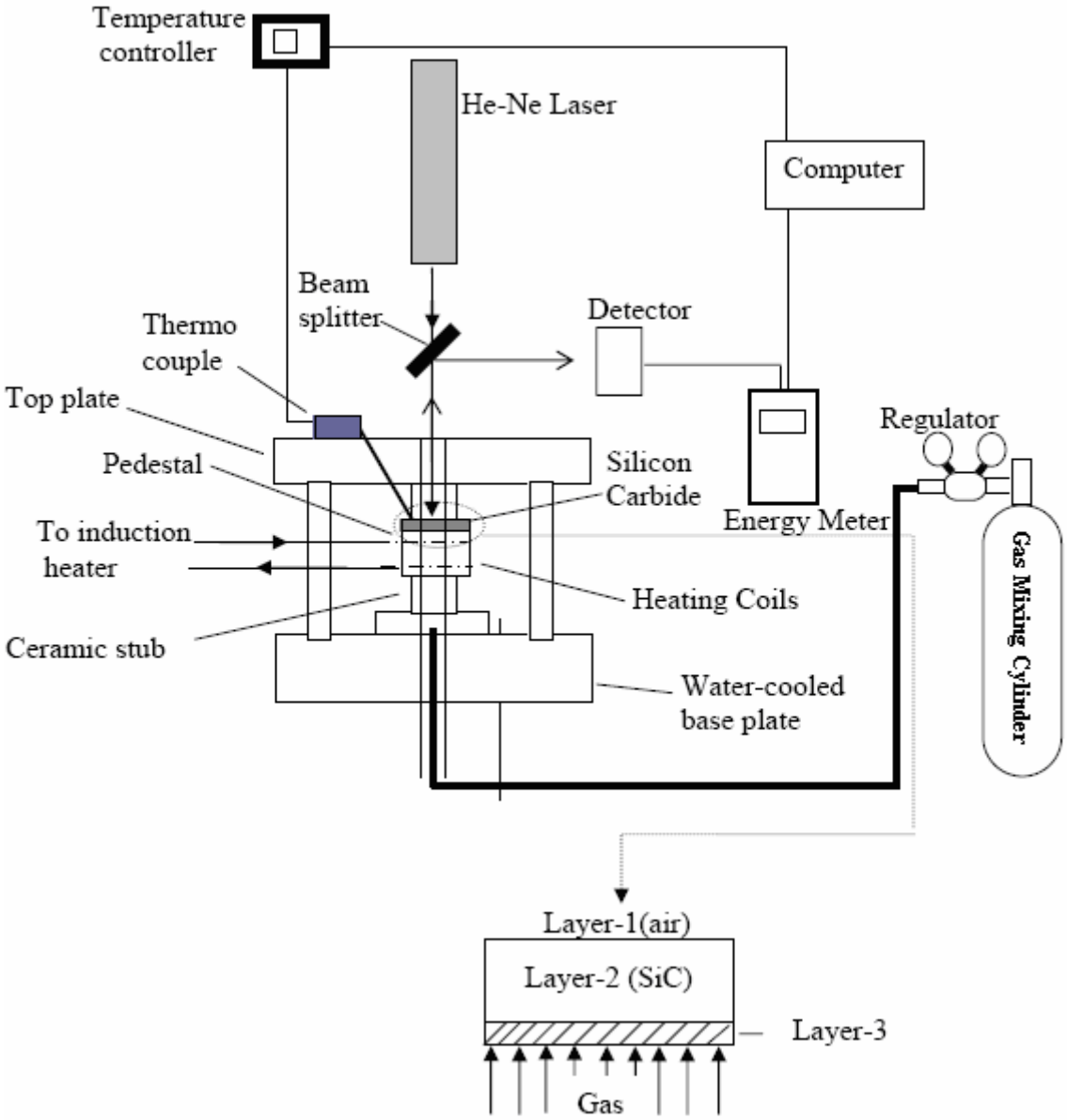

Fig.G.3.1 Schematic diagram of the LAMP Lab. experimental setup for the gas sensing experiment.

In the Kar LAMP Lab., a continuous wave helium-neon (He-Ne) laser of wavelength 632.8 nm was used to understand the changes in the refractive index (n_3) of a compressed layer (see Fig.G.3.1) at the chip-gas interface in the presence of a combustion gas such as H_2, CO, CO_2, and CH_4 for both Pd-P and B doped samples. The combustion gases are present in the

combustor in trace amounts as presented in Table G.3.1. The SiC chip is inherently a Fabry-Pérot interferometer enabling optical measurements pertaining to interference patterns that were analyzed to calculate the compressed layer refractive index, n_3.

"In 1995, ISE (Iniziative Sviluppo Energia) started construction of a new 'clean' power plant, called CET3, at ILVA Taranto, Italy. The plant consisted of three identical combined cycle units capable of producing 530 MW of electrical power. The plant was designed to utilize Blast Furnace Gas (BFG) and Linz Durer Gas (LDG). Dejong Coen was contracted to design and provide the supplementary firing system to produce steam at 540^{o}C. The burners were to utilize BFG and LDG gas supported by natural gas" [25]. The gas composition of the gas mixture for our case has been determined by the following BFG standard [25] as shown in Table G3.1.

Table G.3.1. Typical combustion gas compositions.

Gas Type	BFG (Blast Furnace Gas) [mole %]	LDG (Linz Durer Gas) [mole %]
H_2	4.53	0.96
CH_4	<0.003	-
CO	22.38	69.15
CO_2	23.19	23.19
N_2	48.60	14.89
O_2	0.25	-

A single crystal 4H-SiC wafer of thickness 399 µm was used as an optical chip in this experiment. The experimental setup for studying the optical properties of the chip is shown in Fig. G.3.1. The chip was heated using a steel pedestal as shown in Fig. G.3.1 and the bottom surface of the chip was exposed to the gas mixtures at different pressures. Due to high thermal conductivity of SiC, the thermal energy is transferred to the gas mixture at the chip-gas interface, creating a thermal boundary layer containing hot gas mixture at the interface. This enables us to

test the sensing capability of SiC at high temperatures, pressures and gas species. The effects of the pressure, temperature, and gas compositions of H_2, CO, CO_2, and CH_4 on the optical response of the chip have been studied by examining the reflectivity of the chip. The SiC chip serves as an amplitude-splitting device, so that two reflected lights may be considered as arising from two coherent virtual sources lying behind the silicon carbide wafer. This optical property of SiC makes it an interferometric sensor inherently, enabling highly sensitive remote sensing. A compressed layer (Fig. G.3.1), which consists of compressed SiC atomic layers and hot gases at the chip-gas interface, is formed at the interface due to high pressures and temperatures of the gas mixture. The interface of SiC experiences compressive stresses under high gas pressures and this produces a denser atomic layer of SiC near its bottom surface than the rest of the upper region of the chip.

The measured reflected power exhibits interference pattern with alternating maximum and minimum powers generated by constructive and destructive interference of light respectively for different gas compositions as shown in Fig. G.3.2 to Fig.G.3.6. The patterns of the oscillations are unique to the type of gases. These patterns can be attributed to the characteristic identity of the individual gases in chemical sensing applications. The chip response is selective to the gas species. The refractive index of the composite layer changes depending on the gas species as shown in Fig. G.3.2 to Fig.G.3.6.

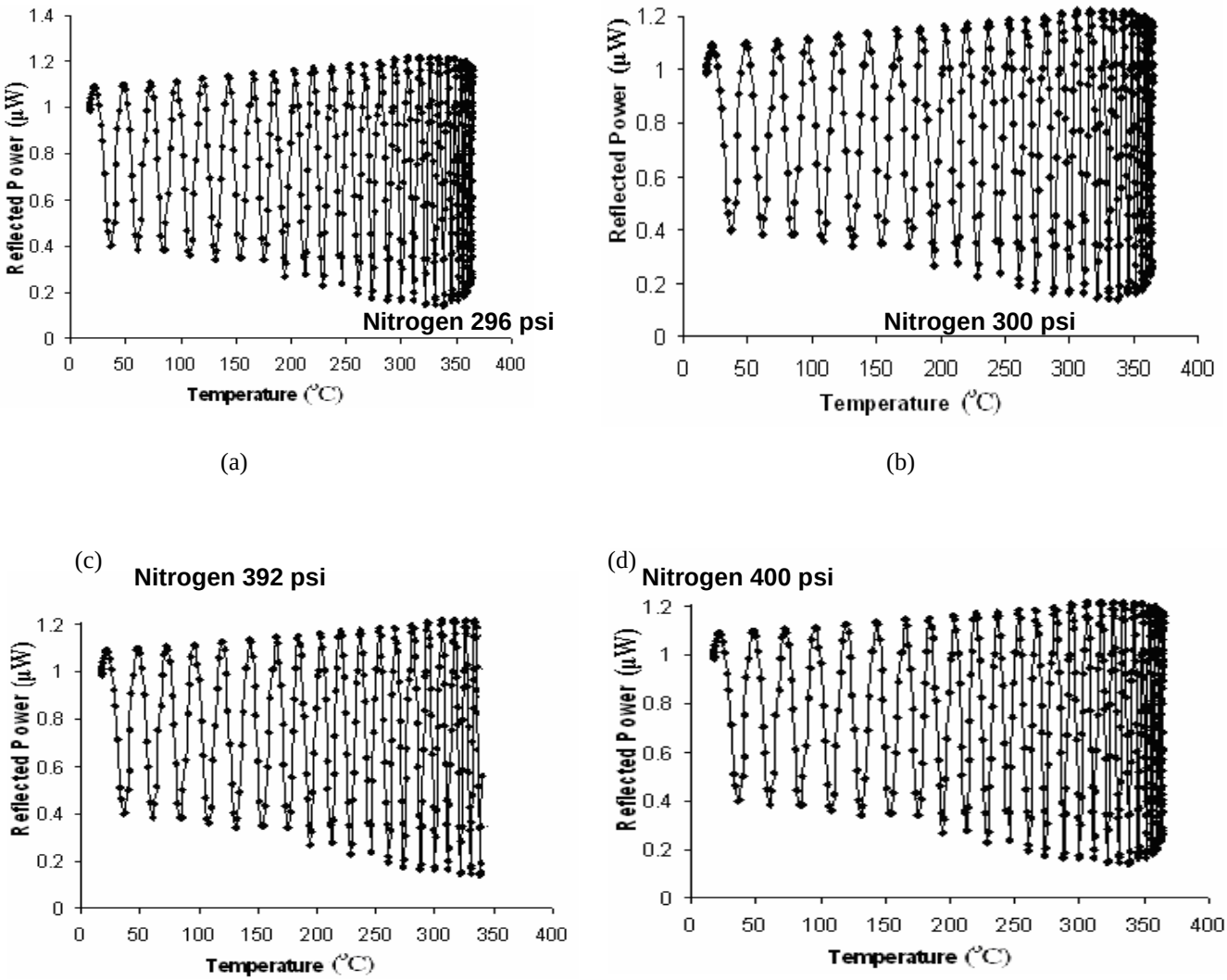

Fig. G.3. 2 (Pd-P) Reflected power of Pd-P doped silicon carbide upon exposure to nitrogen gas at Different pressure (a) 296 psi and (b) 300 psi (c) 392 psi (d) 400 psi as a function of temperature for normal incidence angle.

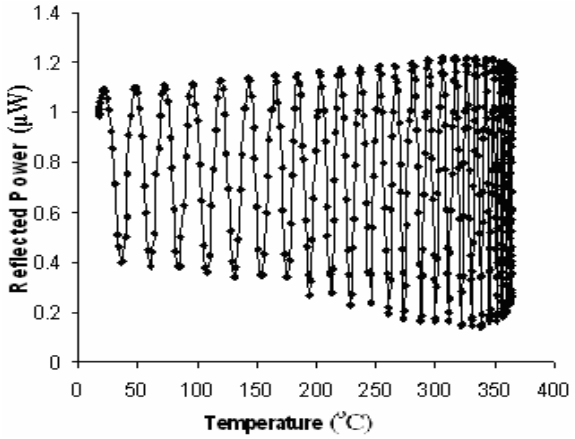

(a)

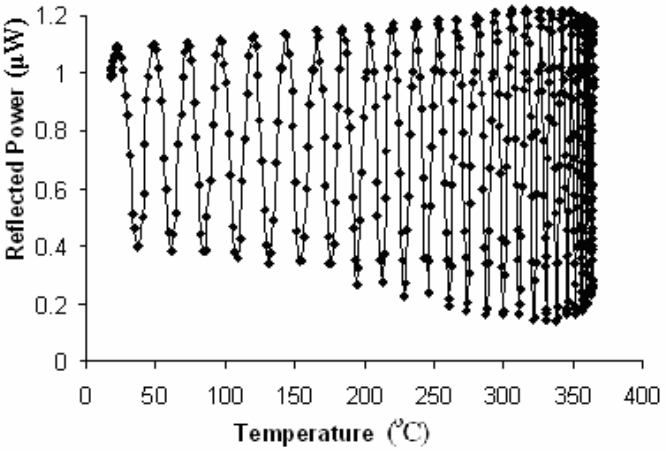

(b)

(c) **Nitrogen 392 psi**

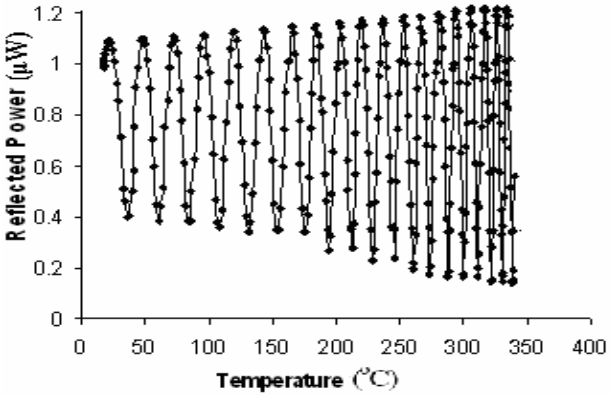

(d) **Nitrogen 400 psi**

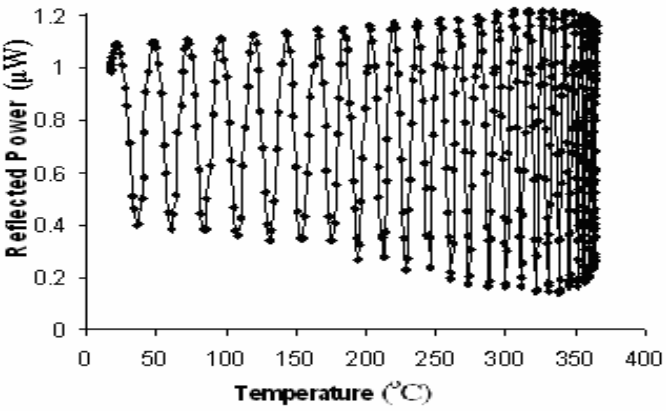

Fig. G.3.2 (B) Reflected power of B doped silicon carbide upon exposure to nitrogen gas at Different pressure (a) 296 psi and (b) 300 psi (c) 392 psi (d) 400 psi as a function of temperature for normal incidence angle.

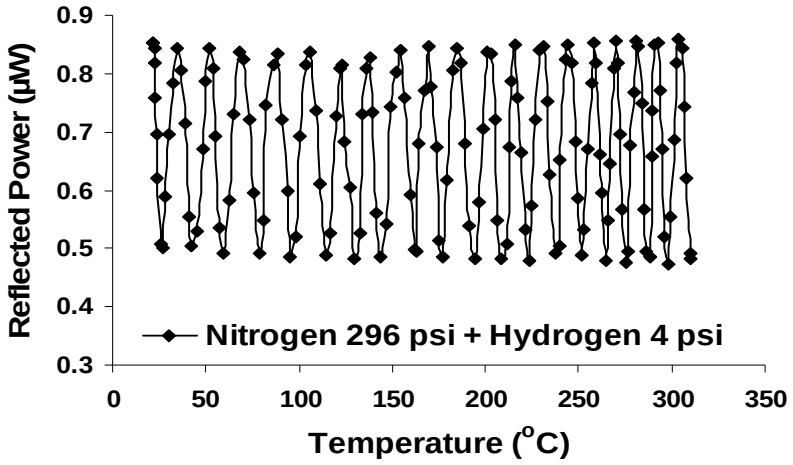

(I)

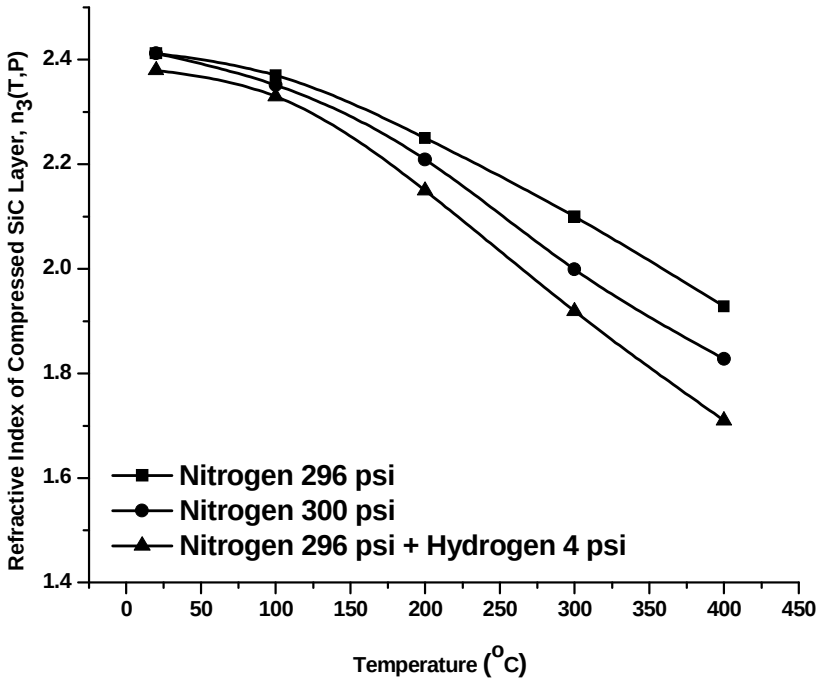

(II)

Fig. G3. 3 Pd-P1 (I) Reflected power of Pd-P doped silicon carbide upon exposure to nitrogen and Hydrogen partial gas pressure: Nitrogen 294 psi + Hydrogen 4 psi as a function of temperature for normal incidence angle. (II) Contribution of Hydrogen on the refractive index of compressed layer at total pressure of 300 psi as a function of temperature.

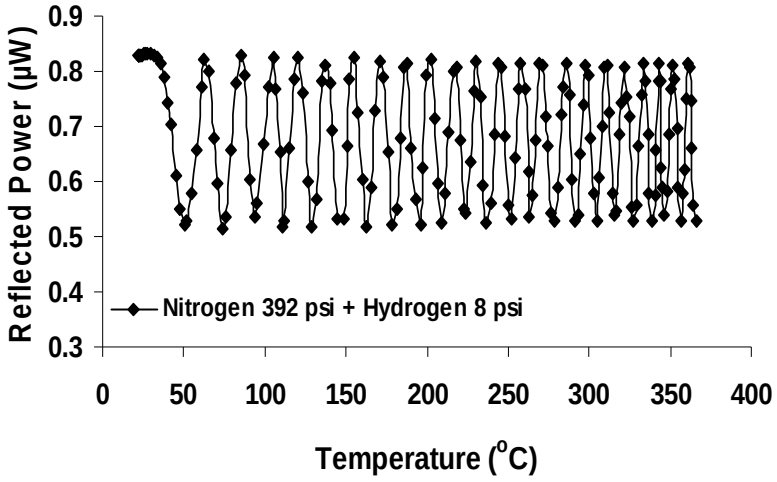

(I)

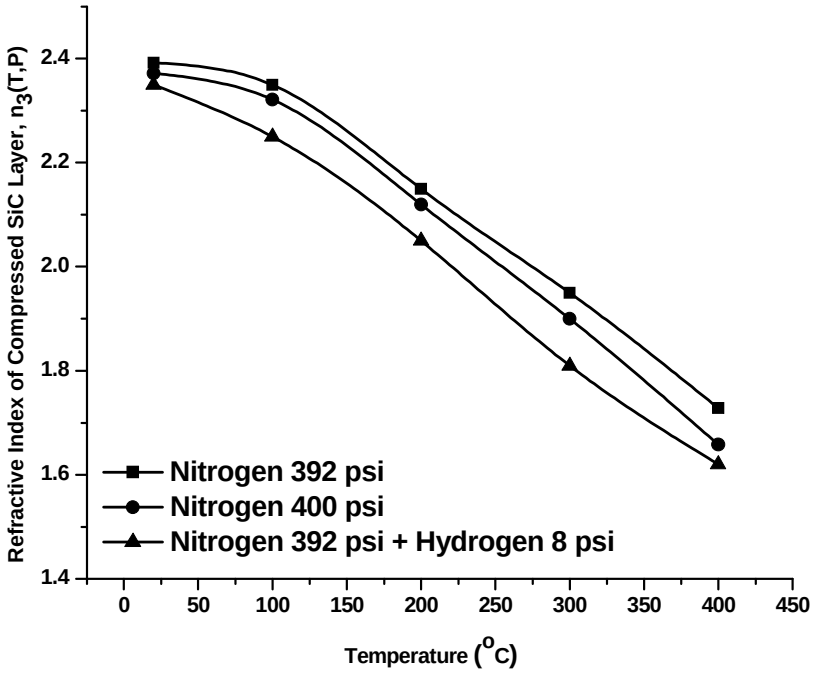

(II)

Fig. G3.3 Pd-P2 (I) Reflected power of Pd-P doped silicon carbide upon exposure to nitrogen and Hydrogen partial gas pressure: Nitrogen 392 psi + Hydrogen 8 psi as a function of temperature for normal incidence angle. (II) Contribution of Hydrogen on the refractive index of compressed layer at total pressure of 400 psi as a function of temperature.

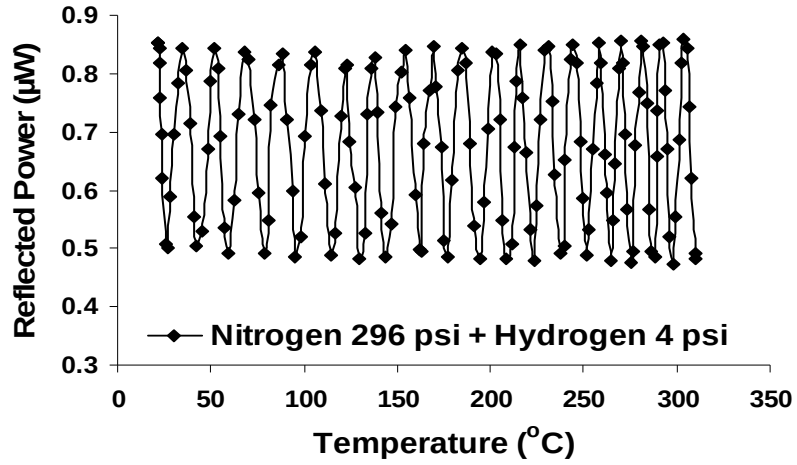

(I)

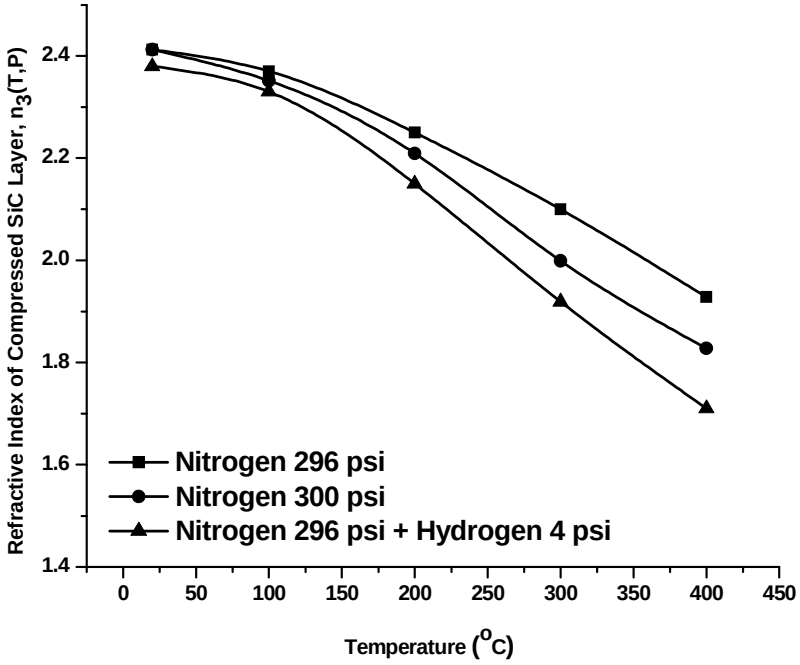

(II)

Fig. G.3.3 B1 (I) Reflected power of B doped silicon carbide upon exposure to nitrogen and Hydrogen partial gas pressure: Nitrogen 294 psi + Hydrogen 4 psi as a function of temperature for normal incidence angle. (II) Contribution of Hydrogen on the refractive index of compressed layer at total pressure of 300 psi as a function of temperature.

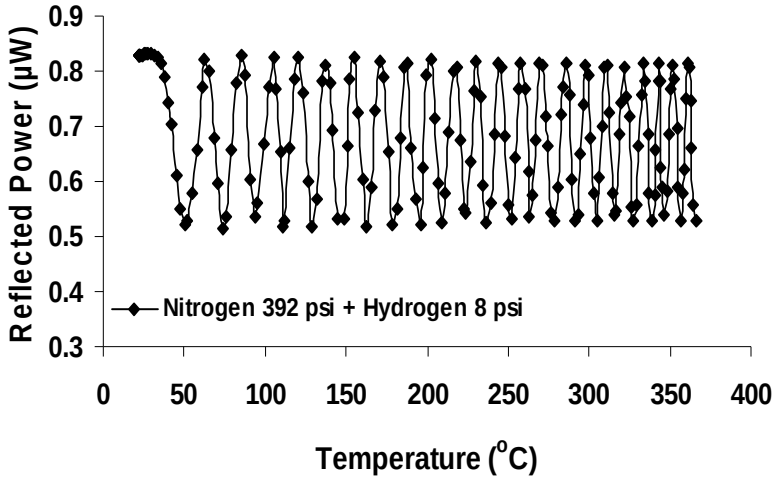

(I)

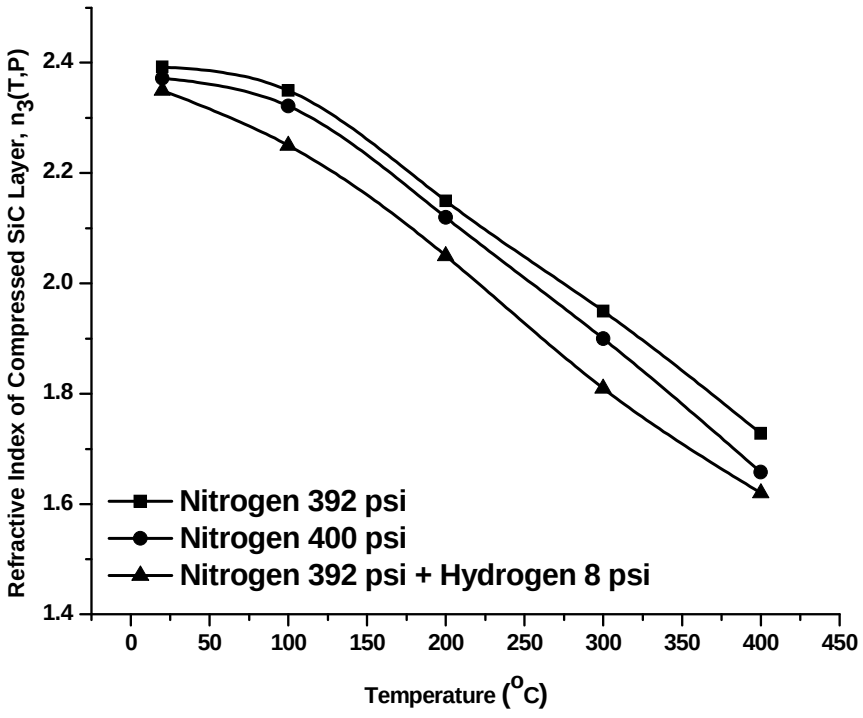

(II)

Fig.G.3.3B2 (I) Reflected power of B doped silicon carbide upon exposure to nitrogen and Hydrogen partial gas pressure: Nitrogen 392 psi + Hydrogen 8 psi as a function of temperature for normal incidence angle. (II) Contribution of Hydrogen on the refractive index of compressed layer at total pressure of 400 psi as a function of temperature.

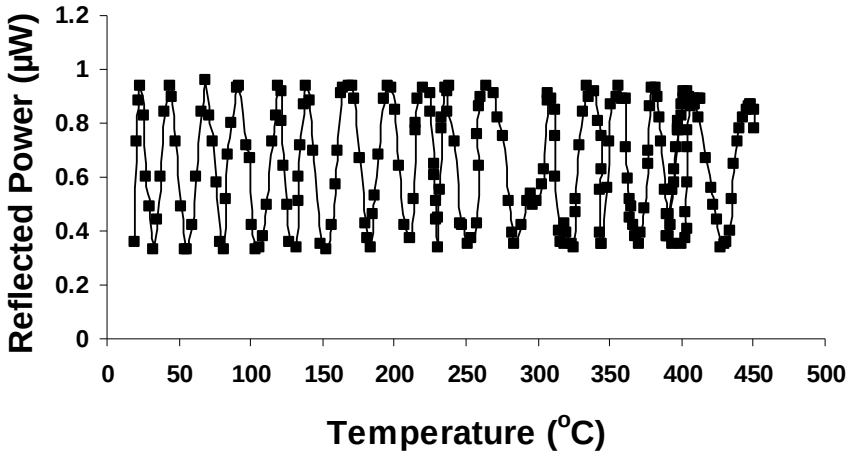

Nitrogen 296 psi + Carbon Monoxide 4 psi

(I)

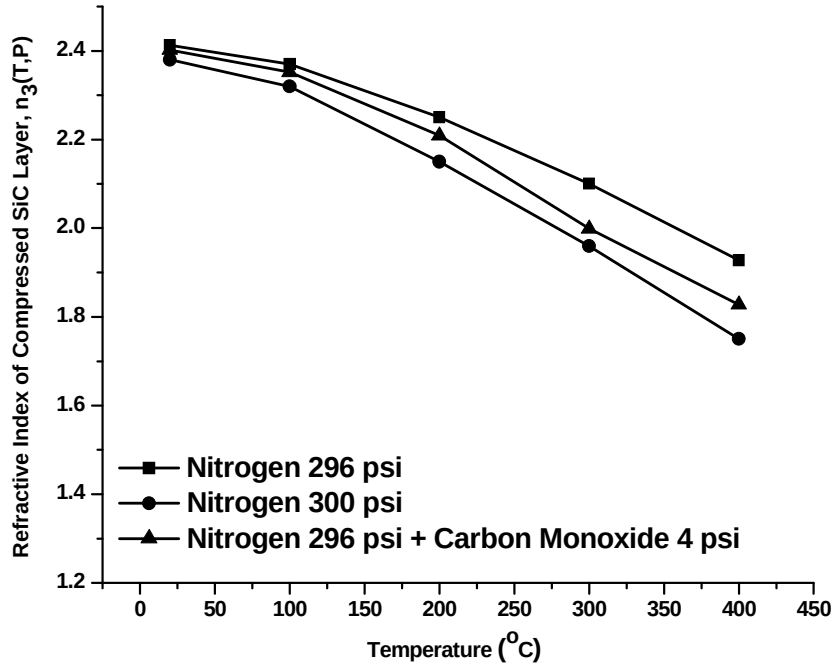

(II)

Fig.G.3.4Pd-P1 (I) Reflected power of Pd-P doped silicon carbide upon exposure to nitrogen and Carbon Monoxide partial gas pressure: Nitrogen 294 psi + Carbon Monoxide 4 psi as a function of temperature for normal incidence angle. (II) Contribution of Carbon Monoxide on the refractive index of compressed layer at total pressure of 300 psi as a function of temperature.

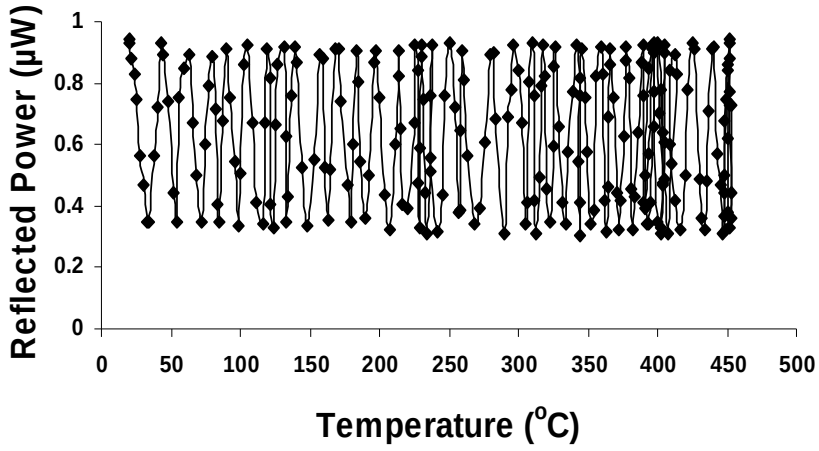

Nitrogen 392 psi + Carbon Monoxide 8 psi

(I)

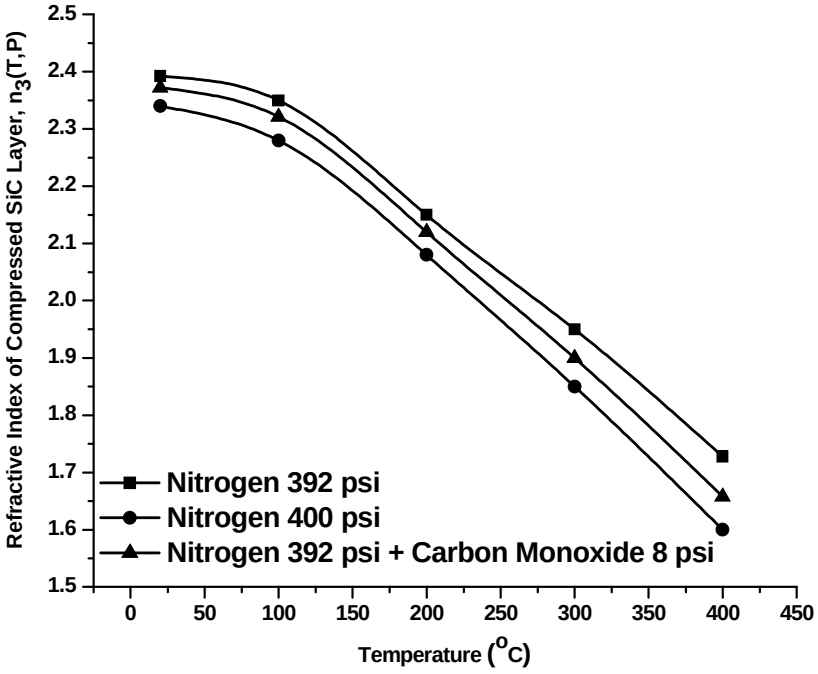

(II)

Fig.G3.4Pd-P2 (I) Reflected power of Pd-P doped silicon carbide upon exposure to nitrogen and Carbon Monoxide partial gas pressure: Nitrogen 392 psi + Carbon Monoxide 8 psi as a function of temperature for normal incidence angle. (II) Contribution of Carbon Monoxide on the refractive index of compressed layer at total pressure of 400 psi as a function of temperature.

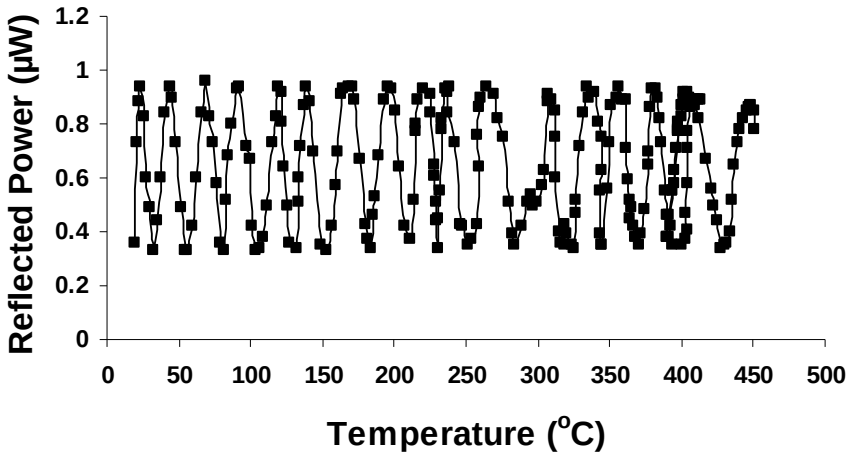

(I)

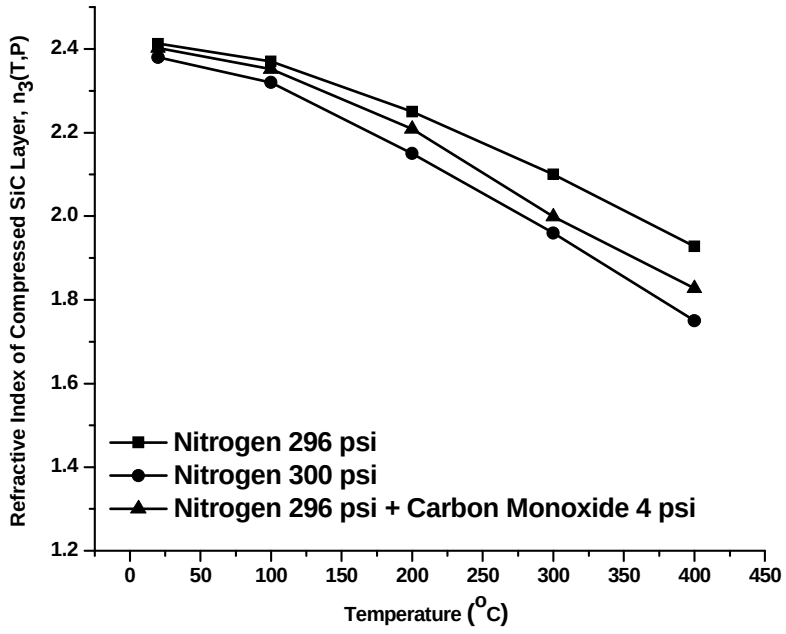

(II)

Fig.G3.4B1 (I) Reflected power of B doped silicon carbide upon exposure to nitrogen and Carbon Monoxide partial gas pressure: Nitrogen 294 psi + Carbon Monoxide 4 psi as a function of temperature for normal incidence angle. (II) Contribution of Carbon Monoxide on the refractive index of compressed layer at total pressure of 300 psi as a function of temperature.

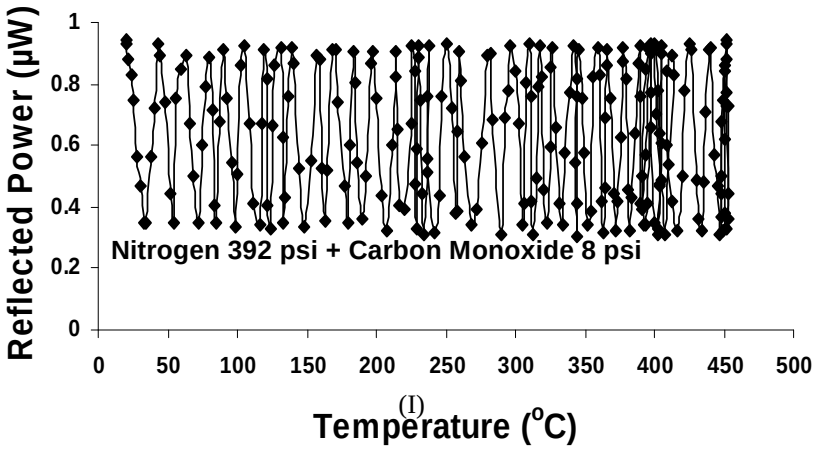

(I)

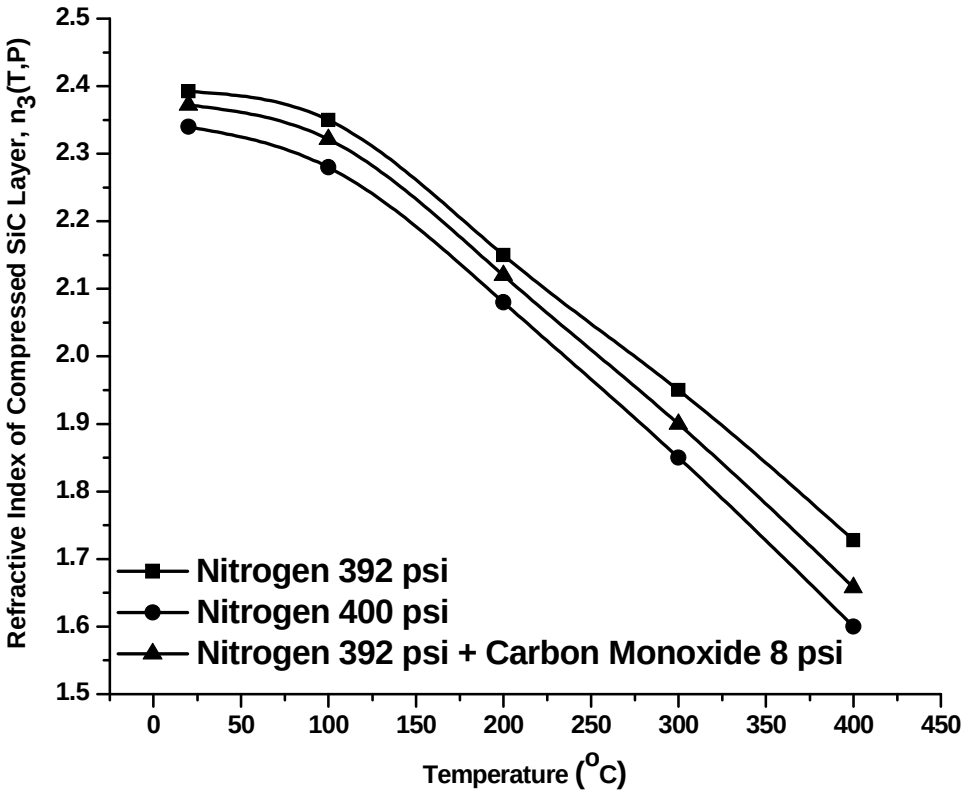

(II)

Fig.G3.4B2 (I) Reflected power of B doped silicon carbide upon exposure to nitrogen and Carbon Monoxide partial gas pressure: Nitrogen 392 psi + Carbon Monoxide 8 psi as a function of temperature for normal incidence angle. (II) Contribution of Carbon Monoxide on the refractive index of compressed layer at total pressure of 400 psi as a function of temperature.

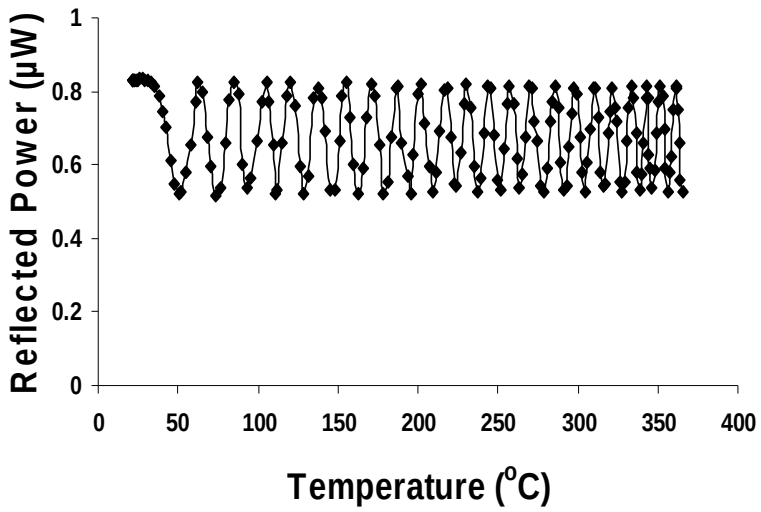

(I)

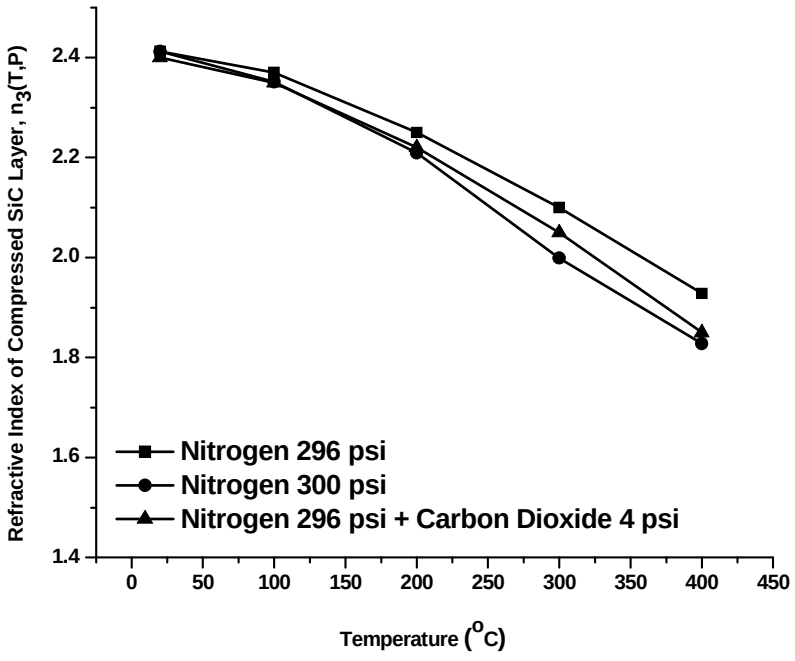

(II)

Fig.G3.5Pd1 (I) Reflected power of Pd doped silicon carbide upon exposure to nitrogen and Carbon Dioxide partial gas pressure: Nitrogen 296 psi + Carbon Dioxide 4 psi as a function of temperature for normal incidence angle. (II) Contribution of Carbon Dioxide on the refractive index of compressed layer at total pressure of 300 psi as a function of temperature.

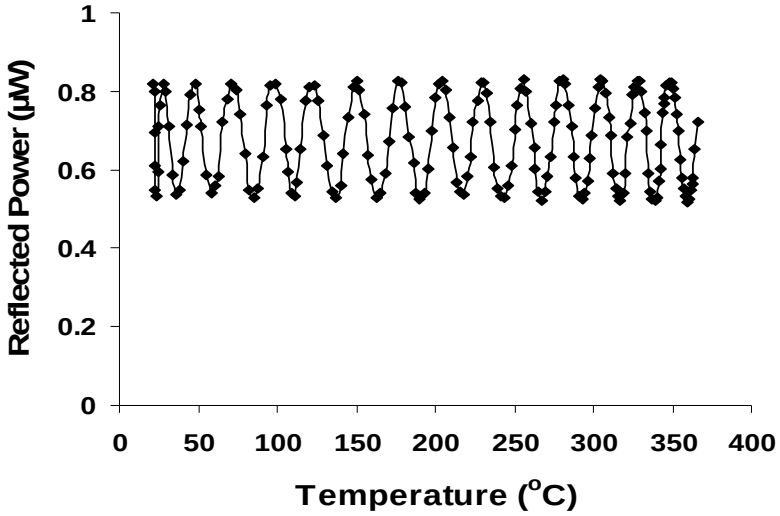

(I)

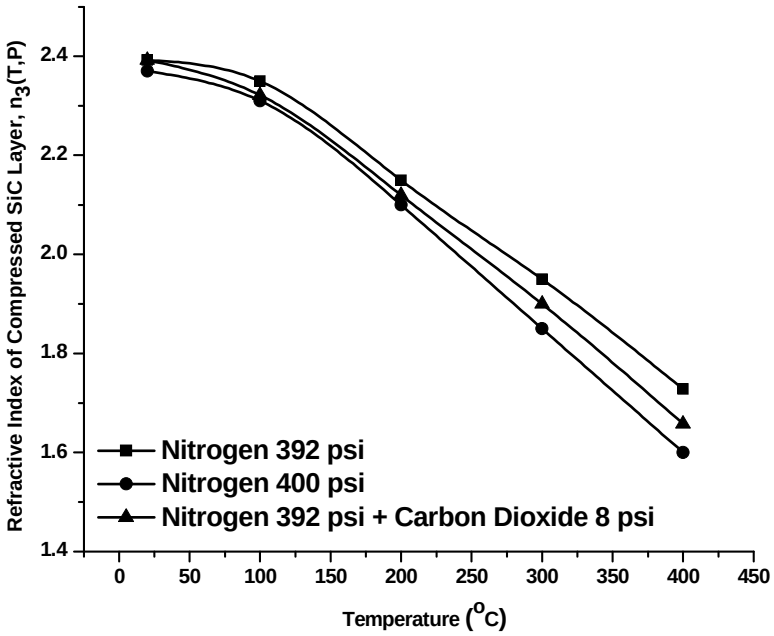

(II)

Fig.G3.5Pd-P2 (I) Reflected power of Pd-P doped silicon carbide upon exposure to nitrogen and Carbon Dioxide partial gas pressure: Nitrogen 392 psi + Carbon Dioxide 8 psi as a function of temperature for normal incidence angle. (II) Contribution of Carbon Dioxide on the refractive index of compressed layer at total pressure of 400 psi as a function of temperature.

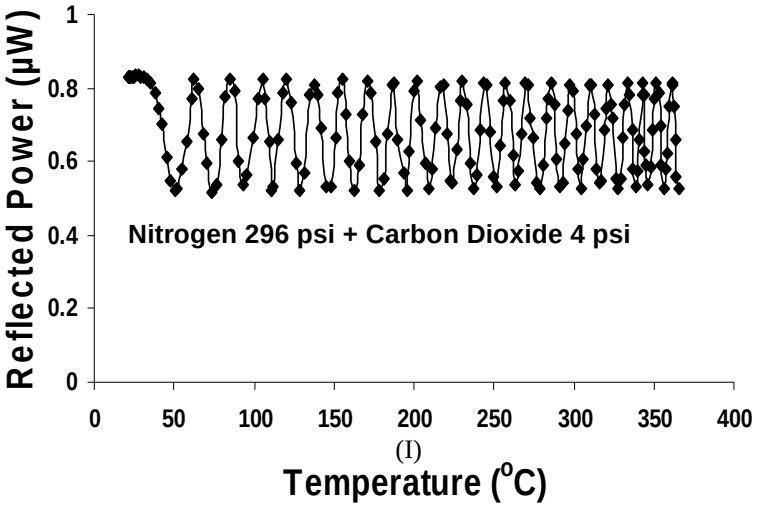

(I)

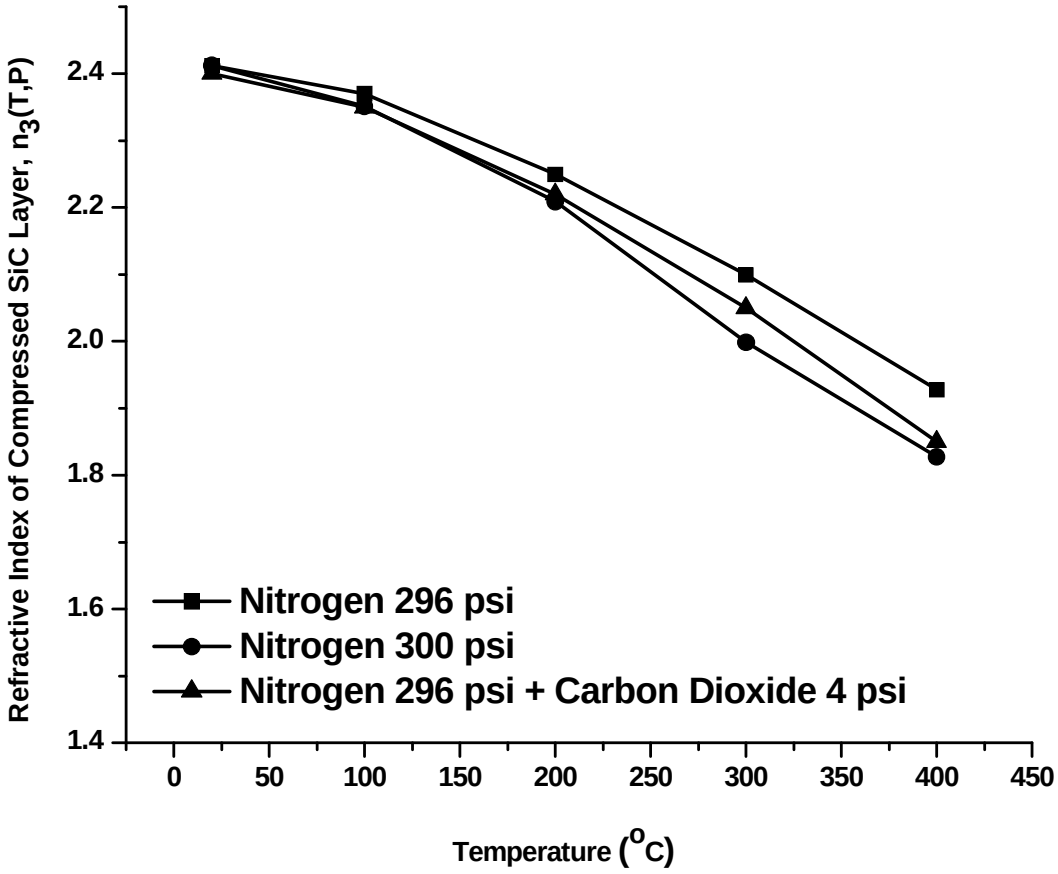

(II)

Fig.G3.5B1 (I) Reflected power of B doped silicon carbide upon exposure to nitrogen and Carbon Dioxide partial gas pressure: Nitrogen 296 psi + Carbon Dioxide 4 psi as a function of temperature for normal incidence angle. (II) Contribution of Carbon Dioxide on the refractive index of compressed layer at total pressure of 300 psi as a function of temperature.

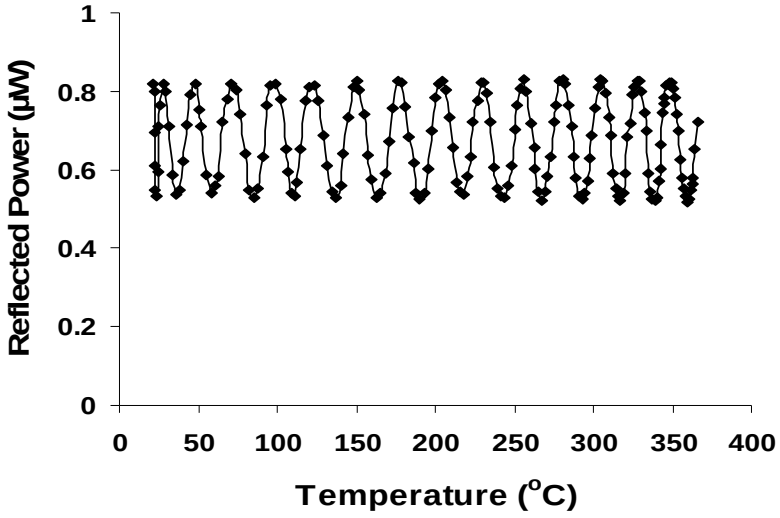

(I)

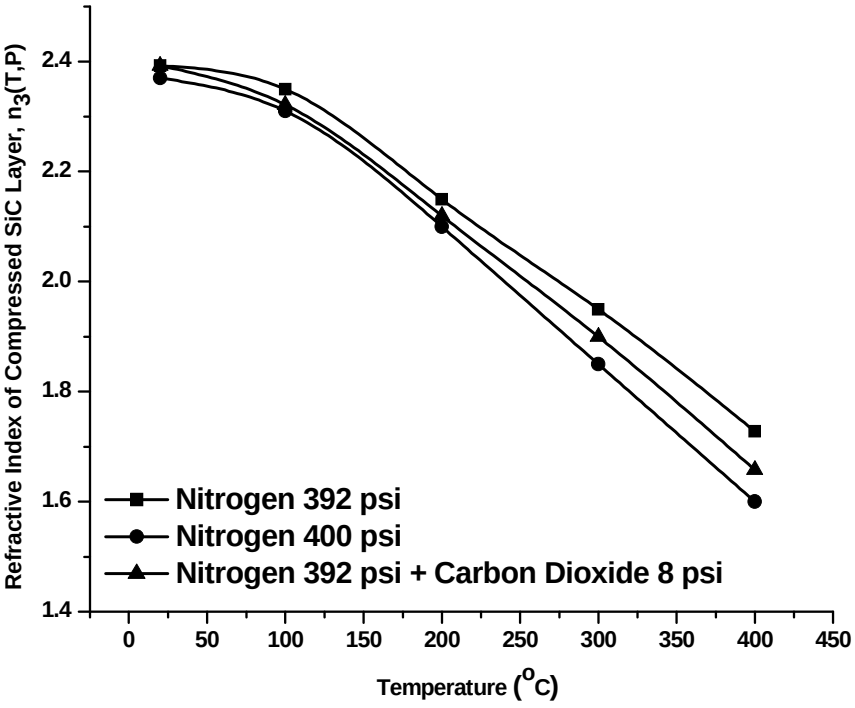

(II)

Fig.G.3.5B2 (I) Reflected power of B doped silicon carbide upon exposure to nitrogen and Carbon Dioxide partial gas pressure: Nitrogen 392 psi + Carbon Dioxide 8 psi as a function of temperature for normal incidence angle. (II) Contribution of Carbon Dioxide on the refractive index of compressed layer at total pressure of 400 psi as a function of temperature.

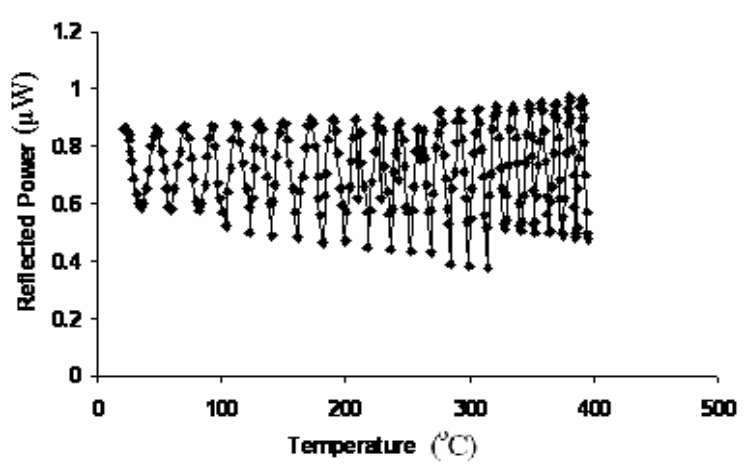

Nitrogen 296 psi + Methane 4 psi

(I)

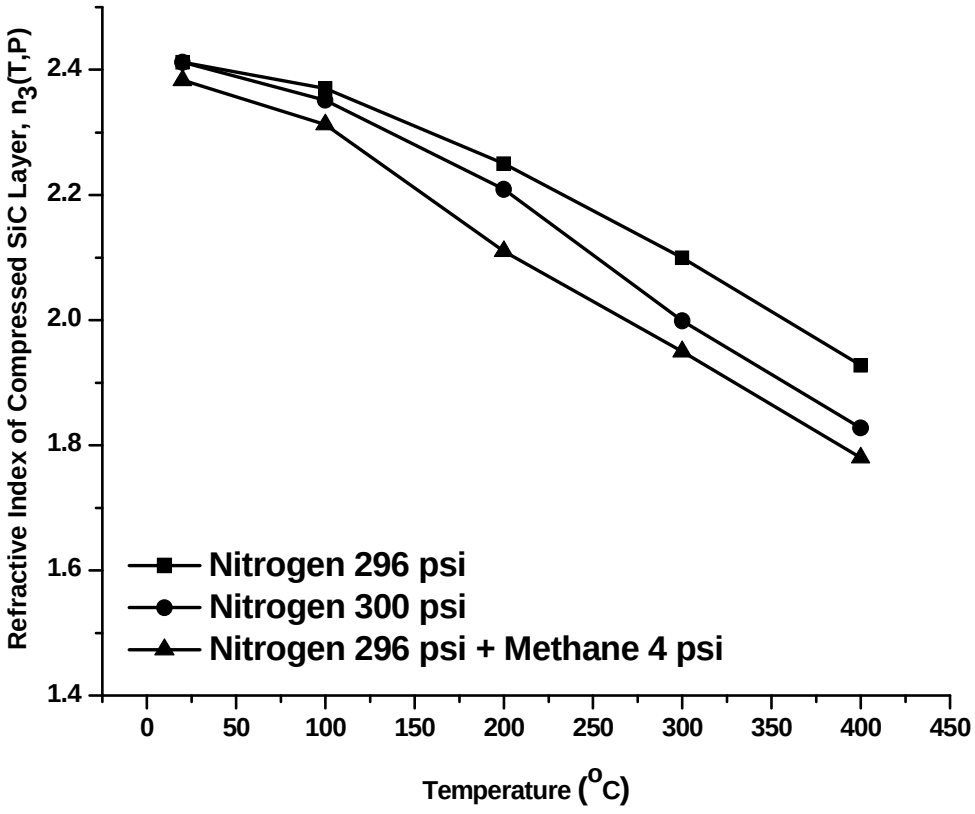

(II)

Fig.G.3.6Pd-P1 (I) Reflected power of Pd-P doped silicon carbide upon exposure to nitrogen and Methane partial gas pressure: Nitrogen 296 psi + Methane 4 psi as a function of temperature for normal incidence angle. (II) Contribution of Methane on the refractive index of compressed layer at total pressure of 300 psi as a function of temperature.

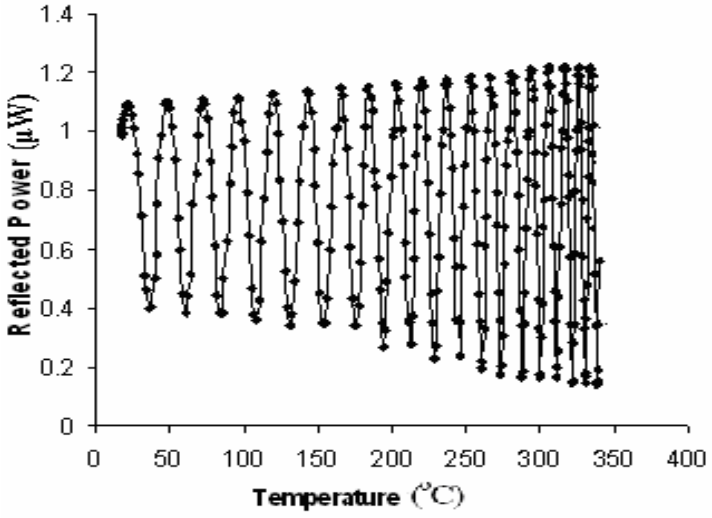

Nitrogen 392 psi + Methane 8 psi

(I)

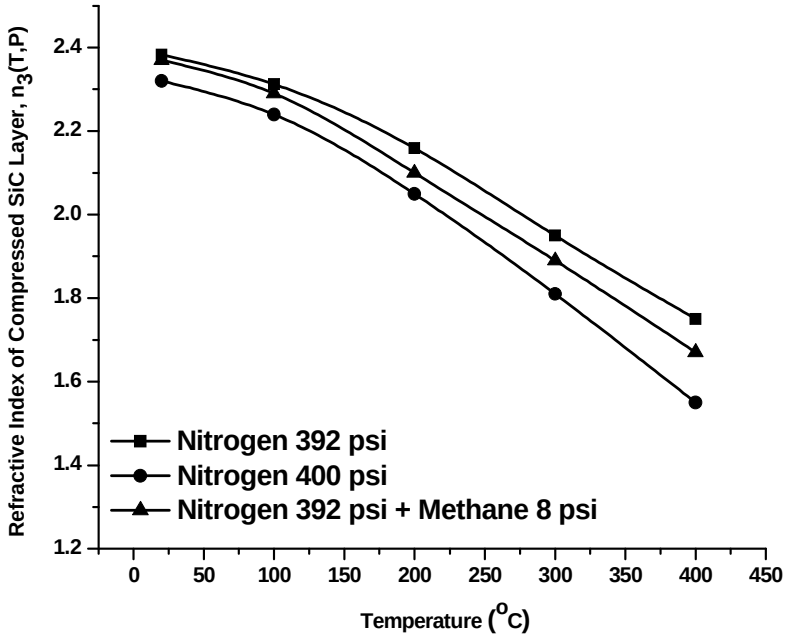

(II)

Fig.G3.6Pd-P2 (I) Reflected power of Pd-P doped silicon carbide upon exposure to nitrogen and Methane partial gas pressure: Nitrogen 392 psi + Methane 8 psi as a function of temperature for normal incidence angle. (II) Contribution of Methane on the refractive index of compressed layer at total pressure of 400 psi as a function of temperature.

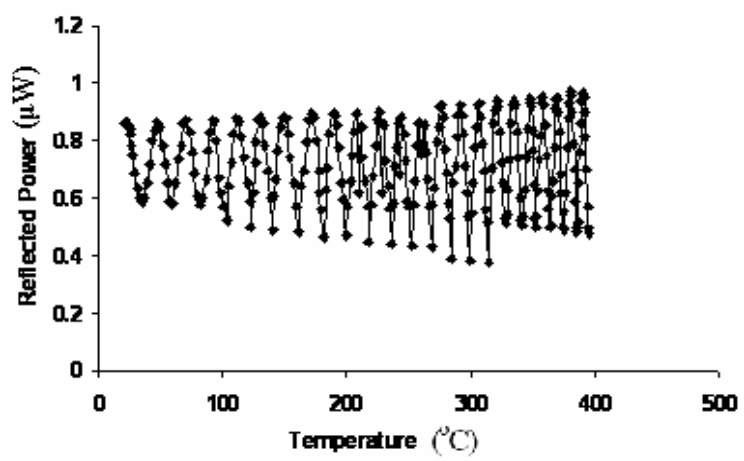

Nitrogen 296 psi + Methane 4 psi

(I)

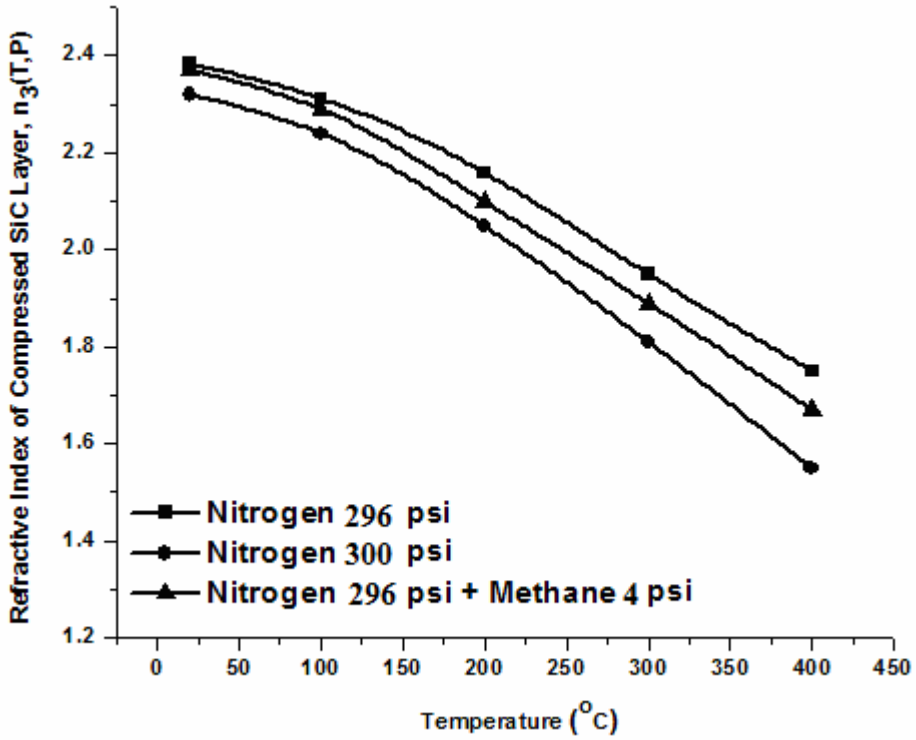

(II)

Fig.G.3.6B1 (I) Reflected power of B doped silicon carbide upon exposure to nitrogen and Methane partial gas pressure: Nitrogen 296 psi + Methane 4 psi as a function of temperature for normal incidence angle. (II) Contribution of Methane on the refractive index of compressed layer at total pressure of 300 psi as a function of temperature.

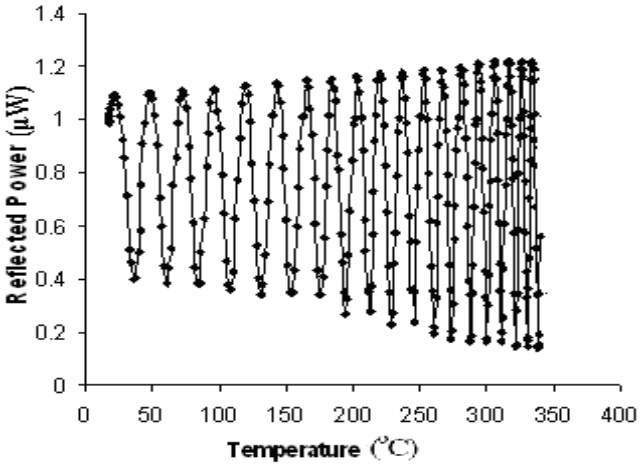

(I)

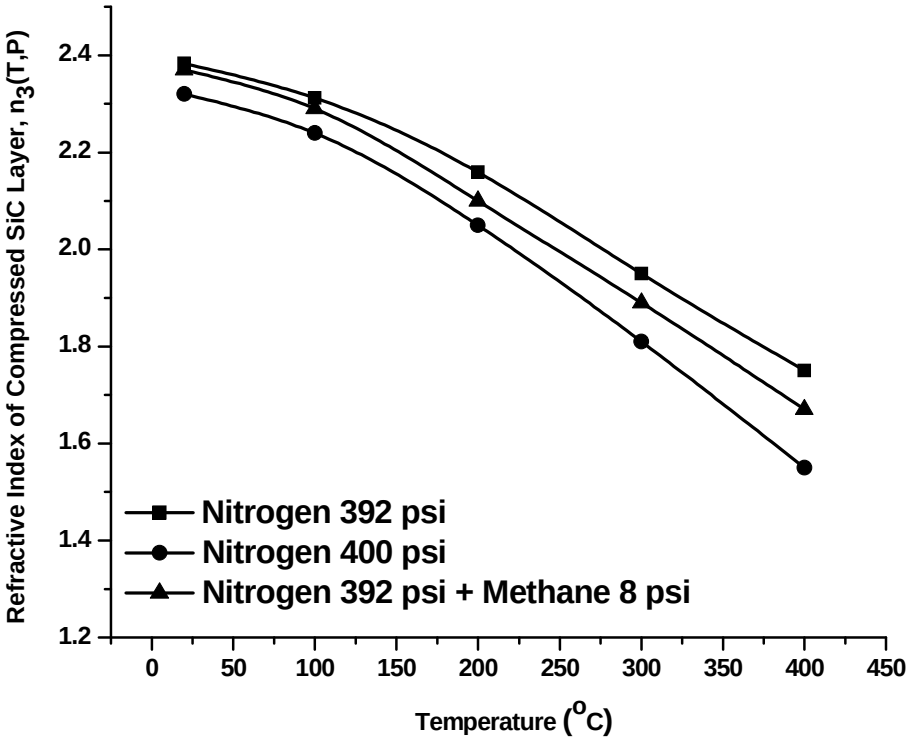

(II)

Fig.G3.6B2 (I) Reflected power of B doped silicon carbide upon exposure to nitrogen and Methane partial gas pressure: Nitrogen 392 psi + Methane 8 psi as a function of temperature for normal incidence angle. (II) Contribution of Methane on the refractive index of compressed layer at total pressure of 400 psi as a function of temperature.

The refractive index can be extracted from the interference pattern using the following expression [26-28]:

$$n_{m+1} = \frac{\lambda_0 + n_m d_0 \left[2 - \frac{1}{E}(\Delta P) - \alpha_{mid}(\Delta T) \right]}{d_0 \left[2 - \frac{3}{E}(\Delta P) + \alpha_{mid}(\Delta T) \right]} \quad (1)$$

Here $\Delta T = T_{Final1} - T_0$, $\Delta P = P_{Final} - P_0$. Various symbols in Eq. (1) are defined in the nomenclature section. From the refractive indices data, it is clearly observed that at high temperature and pressure the compressed layer refractive index decreases.

Next described is the contribution ($\Delta n_{3,X}$) to the compressed layer refractive index due to different combustion gases. 'X' refers to different combustion gases such as H_2, CO, CO_2 and CH_4. The refractive index data can be used to sense all the different combustion gases. Let us say that the refractive index of the compressed layer is $n_{3,296N2}$ for 296 psi of nitrogen. When 4 psi of hydrogen added to 296 psi of pure nitrogen, the refractive index of the compressed layer due to this 300 psi gas mixture is $n_{3,296N2+4H2}$. The value of $n_{3,296N2+4H2}$ is less the value of $n_{3,296N2}$, indicating that 4 psi of hydrogen has reduced the compressed layer refractive index compare to the compressed layer refractive index in presence of 296 psi of pure nitrogen. This reduction in the compressed layer refractive index is given by,

$$\Delta n_{3,H2} = n_{3,296N2} - n_{3,296N2+4H2} \quad (2)$$

In this section, the Kar LAMP Lab. discusses the change in compressed layer refractive index due to different combustion gas species mixtures compare to the same pressure of pure nitrogen. According to the earlier stated figures, it is clear that the compressed layer refractive

indices of pure nitrogen pressure of 300 psi and the partial pressure of combustion gases with nitrogen of same pressure have distinct different value which indicates that the difference is due to the combustion gas species. It has been observed that for hydrogen partial pressure of 4 psi and 8 psi, the compressed layer refractive indices are less compare to the pure nitrogen pressure of 300 psi and 400 psi respectively. But for other combustion gases, the compressed layer refractive indices are larger than the pure nitrogen. So, the refractive indices data can be used to detect different combustion gas species. The contribution of different combustion gases to the compressed layer refractive index have been tabulated in Table G3.2.1 for pure nitrogen and Table G3.2.2 for hydrogen, methane, carbon monoxide, carbon dioxide. Figs. G3.7 are the graphical representation of the contributions.

Table G3.2.1: Contribution on compressed layer refractive index by pure nitrogen

Doping	Gas Species	Partial Pressure	Contribution $(\Delta n_{3,X})$ of combustion gases to the compressed layer $\Delta n_{3,X} = n_{3,YN2} - n_{3,aN2+bX}$				
			20°C	100°C	200°C	300°C	400°C
B	N_2	296 psi	0.01	0.05	0.12	0.20	0.30
		392 psi	0.02	0.12	0.15	0.22	0.33
Pd-P	N_2	296 psi	0.01	0.05	0.12	0.20	0.30
		392 psi	0.02	0.12	0.15	0.22	0.33
Undoped	N_2	296 psi	0.01	0.05	0.12	0.20	0.30
		392 psi	0.02	0.12	0.15	0.22	0.33

Table G3.2.2: Contribution on compressed layer refractive index by different doping elements.

Doping elements	Gas Species	Partial Pressure	Contribution $(\Delta n_{3,X})$ of combustion gases to the compressed layer $\Delta n_{3,X} = n_{3,YN2} - n_{3,aN2+bX}$				
			20°C	100°C	200°C	300°C	400°C
B	H_2	4 psi	0.03	0.04	0.10	0.18	0.21
		8 psi	0.04	0.10	0.10	0.14	0.14
Pd-P	H_2	4 psi	0.03	0.04	0.10	0.18	0.21
		8 psi	0.04	0.10	0.10	0.14	0.14
Undoped	H_2	4 psi	0.03	0.04	0.10	0.18	0.21
		8 psi	0.04	0.10	0.10	0.14	0.14
B	CH_4	4 psi	0.01	0.03	0.05	0.10	0.10
		8 psi	0.02	0.04	0.05	0.11	0.12
Pd-P	CH_4	4 psi	0.01	0.02	0.04	0.10	0.10
		8 psi	0.02	0.02	0.05	0.11	0.12
Undoped	CH_4	4 psi	0.01	0.02	0.04	0.10	0.10
		8 psi	0.02	0.02	0.05	0.11	0.12
B	CO	4 psi	0.01	0.01	0.04	0.10	0.10
		8 psi	0.02	0.02	0.03	0.05	0.07
Pd-P	CO	4 psi	0.01	0.01	0.04	0.10	0.10
		8 psi	0.02	0.02	0.03	0.05	0.07
Undoped	CO	4 psi	0.01	0.01	0.04	0.10	0.10
		8 psi	0.02	0.02	0.03	0.05	0.07
B	CO_2	4 psi	0.01	0.02	0.03	0.05	0.08
		8 psi	0.02	0.04	0.05	0.10	0.12
Pd-P	CO_2	4 psi	0.01	0.02	0.03	0.05	0.08
		8 psi	0.02	0.04	0.05	0.10	0.12
Undoped	CO_2	4 psi	0.01	0.02	0.03	0.05	0.08
		8 psi	0.02	0.04	0.05	0.10	0.12

The chip response behavior of the Pd/3C-SiC (epilayer on Si substrate) Schottky junctions has been studied at 400°C in the presence of hydrogen gas with varying concentrations from 500 to 10,000 ppm [29]. The sensitivity, response time and the reversibility were investigated from the transient response characteristics of the doped SiC chips. The sensitivity was found to be a function of applied bias across the junction. A gas sensing mechanism has been proposed for these Schottky sensors [29-30]. Also boron has been already successfully used for detection of methane [31].

In Table G3.2.2, ‘a’ refers to the pressure of N_2 in the gas mixture, ‘b’ refers to the pressure of X (X= H_2, CO, CO_2, or CH_4) in the gas mixture, Y refers to the pressure of pure N_2 where Y= a, Y=296 psi when b=4 psi and Y= 392 psi when b = 8 psi.

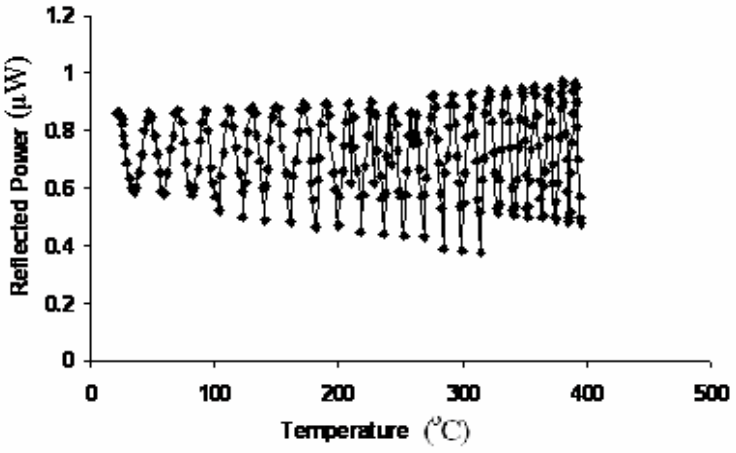

Nitrogen 296 psi + Methane 4 psi

(I)

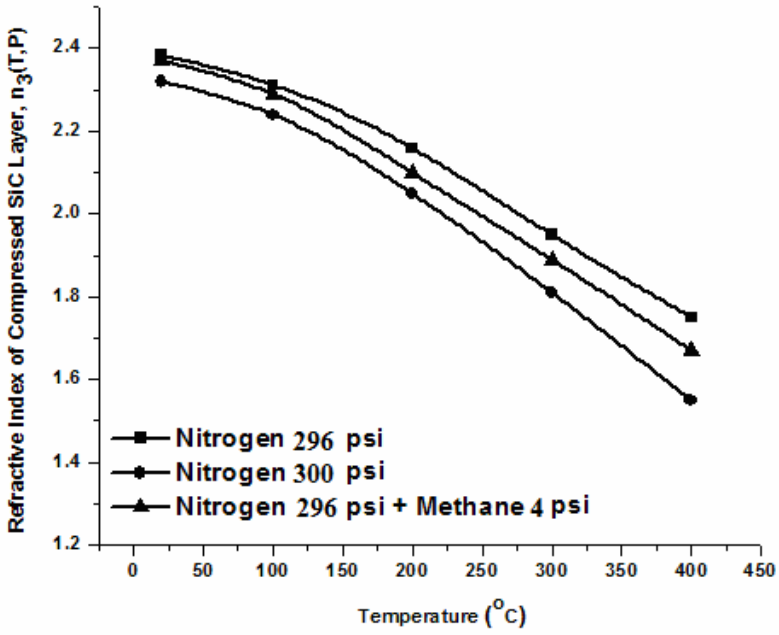

(II)

Fig.G3. 7a (I) Reflected power of undoped silicon carbide upon exposure to nitrogen and Methane partial gas pressure: Nitrogen 296 psi + Methane 4 psi as a function of temperature for normal incidence angle. (II) Contribution of Methane on the refractive index of compressed layer at total pressure of 300 psi as a function of temperature.

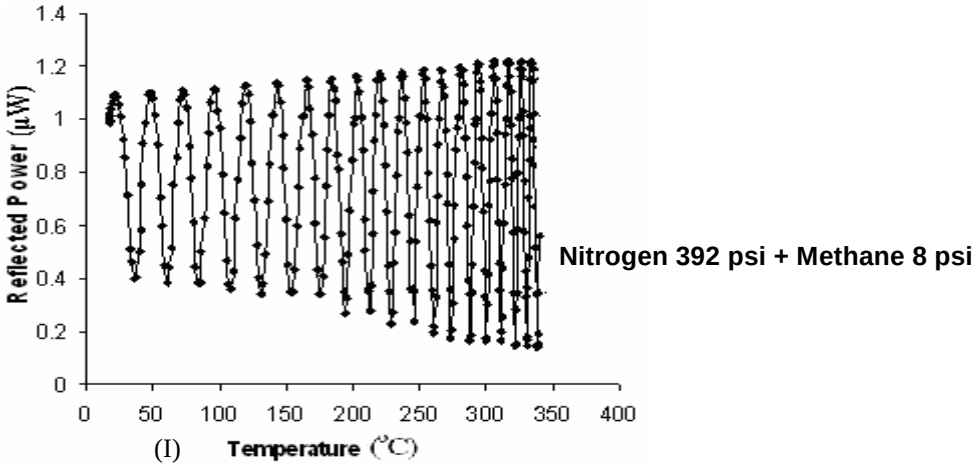

(I)

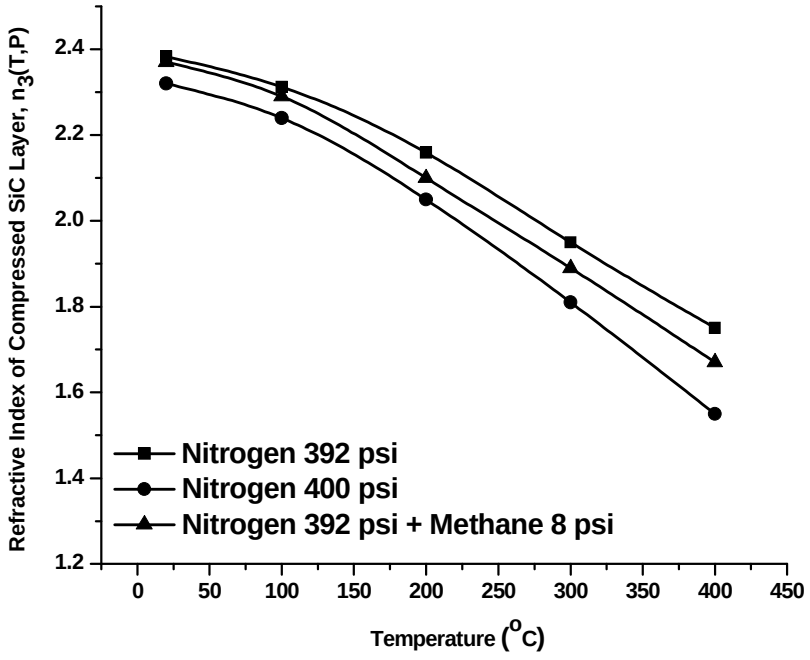

(II)

Fig.G3. 7b (I) Reflected power of undoped silicon carbide upon exposure to nitrogen and Methane partial gas pressure: Nitrogen 392 psi + Methane 8 psi as a function of temperature for normal incidence angle. (II) Contribution of Methane on the refractive index of compressed layer at total pressure of 400 psi as a function of temperature.

SiC Chip Doping Studies (Kar LAMP Lab. and AppliCote Associates Data):

Digital pictures of the 1 cm × 1 cm SiC wafers are presented in Figs. G3. 8a and G3. 8b. Three (3) doped chips were created by laser doping each of the wafers with a particular or combination

of dopants; e.g., Pd-P, Pd and B. Discoloration is observed in the dual simultaneously Pd-P laser doped substrate (Fig G3. 8a). A laser doping technique [32-35] that was developed at UCF for compound semiconductors, such as SiC, was used to fabricate doped chips. The parameters used for the laser doping experiments are presented in Table G3. 3 and Table G3. 4.

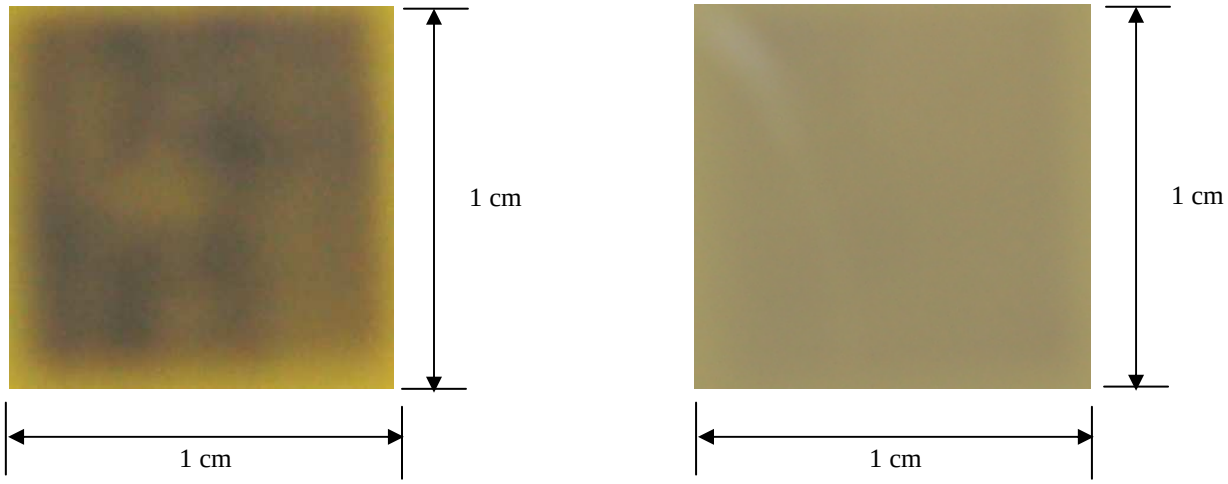

a. Palladium-Phosphorus laser doped

b. Boron laser doped

FigG3. 8. Digital photographs of palladium-phospohorus and boron laser doped 4H-SiC chips.

AppliCote Associates (AA), LLC has completed modification of a scanning electron microscope coupled with energy dispersive spectra chemical analysis (SEM/EDS) sample stage, increasing its sample capacity. This approach was taken to economize materials characterization analysis and to allow “same time” evaluation of a group of samples to better understand inconsistencies and trends in processing, Figure G3. 9.

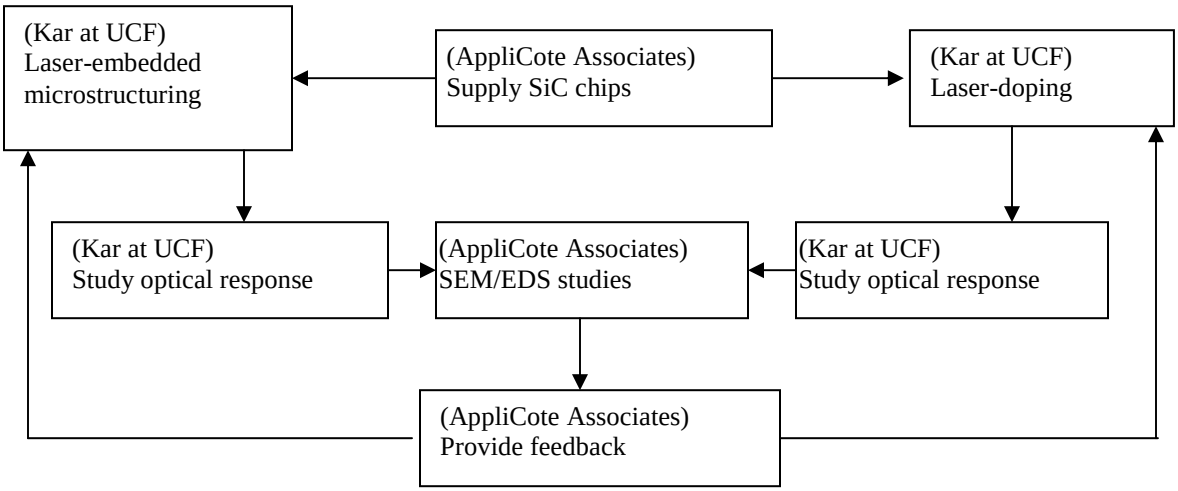

Figure G3. 9. Project activities for SiC chip development, chip fabrication and optical response studies.

SEM/EDS analysis of the samples showed no surface damage or defect generation or concentration variations. To better analyze surface damage an optical profilometer (OP) was used. Energy dispersive spectra chemical analysis (EDS) is generally sensitive to chemical compositions 4% atomic concentration or greater and detects chemistry at a depth 1 micron and deeper; EDS is not a surface or near surface analytical tool. Consequently Secondary Ion Mass Spectroscopy (SIMS) was used to validate that dopants were incorporated to measure concentration profiles. In summary the SEM/EDS protocol was replaced by the OP/SIMS protocol. Figures G3. 10 and G3. 11, representative SIMS data, validate that dopant was incorporated into the 4H-SiC substrate. Figure G3. 10 shows palladium-phosphorus, laser doped by the drive-in process. A standard is required for conversion to concentration which was not available at AMPAC the time of this experiment. Complete standardization is required before detailed SIMS analysis of the Pd-P laser doped sample. Figure G3. 11 shows the SIMS concentration profile for Boron which has exceeded the solubility limit at the surface. Laser

doping is the only known doping technique that can incorporate concentrations beyond the solubility limit; consequently higher dopant concentrations can be obtained compared to conventional processes.

The optical profilometer studies referenced to untreated 4H-SiC surfaces shows no damage after boron laser doping but some surface damage after Pd-P doping (Figures G3. 5 and G3. 6, G3. 7 and G3. 8). The damage on the Pd-P laser doped 4H-SiC surface plausibly results from laser ablation during doping indicating that the laser intensity needs to be decreased below this ablation threshold.

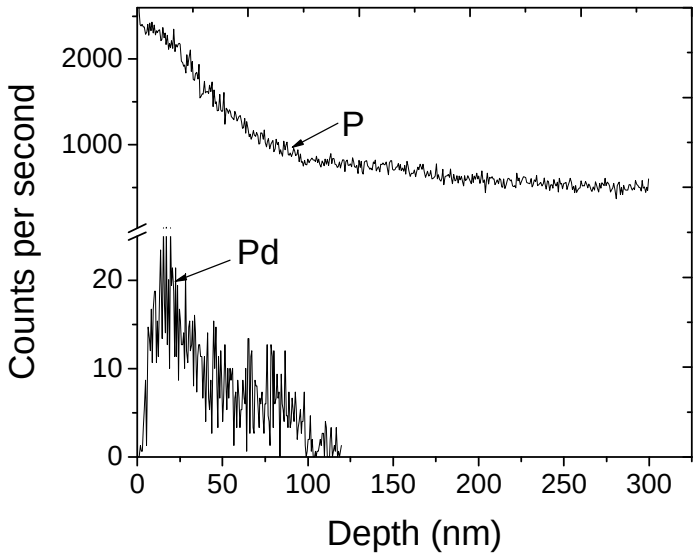

Fig. G3. 10. Laser-doped Palladium-Phosphorus profile in 4H-SiC substrate. The parent wafer was an undoped 4H-SiC substrate. A standard needs to be procured and analyzed to accurately convert counts per second to concentration.

Table G3. **3. Palladium-Phosphorus Laser Doping Parameters**

Sample	Dopant	Power (W)	Pulse repetition rate (KHz)	Focal Length (mm)	Spot size (μm)	# of passes	Scanning speed (mm/sec)	Dopant medium
4H-SiC (undoped)	Pd-P	8	CW	150	100	1	2	Tetrakis (Triphenyl phosphine) Palladium Powder, argon 30 psi
	Pd-P	12.5	5	150	80	1	0.8	Drive in, Argon 30 psi

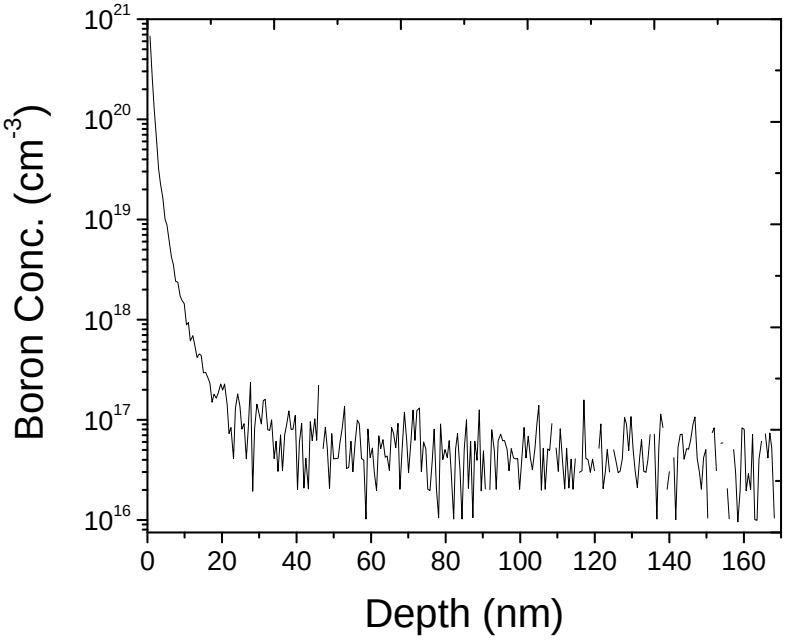

Fig. G3. 11. Laser-doped Boron profile in 4H-SiC substrate. The parent wafer was an undoped 4H-SiC substrate. The sample has exceeded the solid solubility limit of 2.5×10^{20} cm^{-3} for B in SiC at the surface.

Table G3. **4. Boron Laser Doping Parameters**

Sample	Dopant	Power (W)	Pulse repetition rate (KHz)	Focal Length (mm)	Spot size (μm)	# of passes	Scanning speed (mm/sec)	Dopant medium
4H-SiC (undoped)	B	11.9	5	150	100	1	0.7	Triethyl boron heated in a bubbler to 80°C + argon (30 psi)

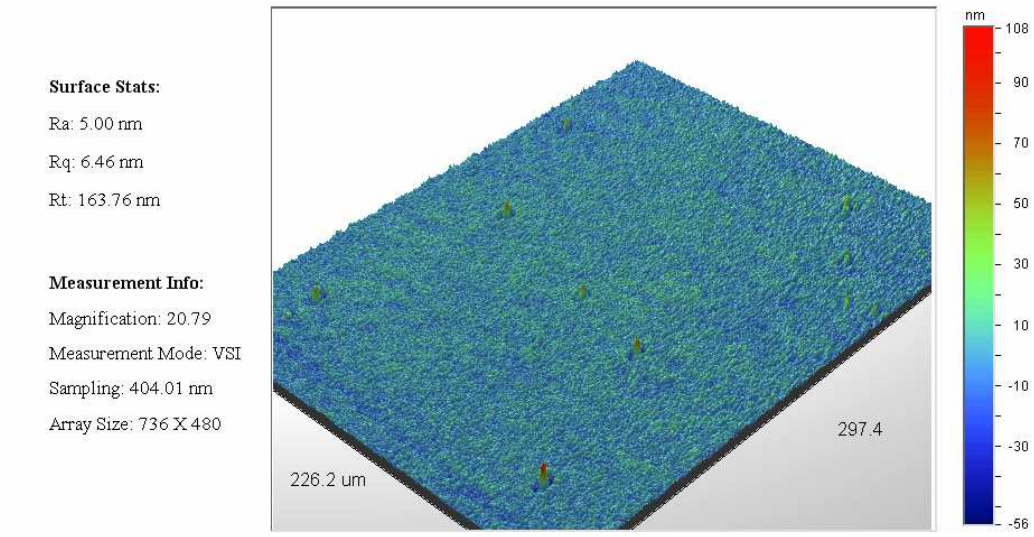

Fig. G3. 12. Parent wafer type: undoped 4H-SiC. Optical profilometric data for laser-untreated wafer surface. The average surface roughness (Ra) is 5 nm and the peak to valley roughness is 163.76 nm. This is the opposite surface of the Pd-P-doped surface.

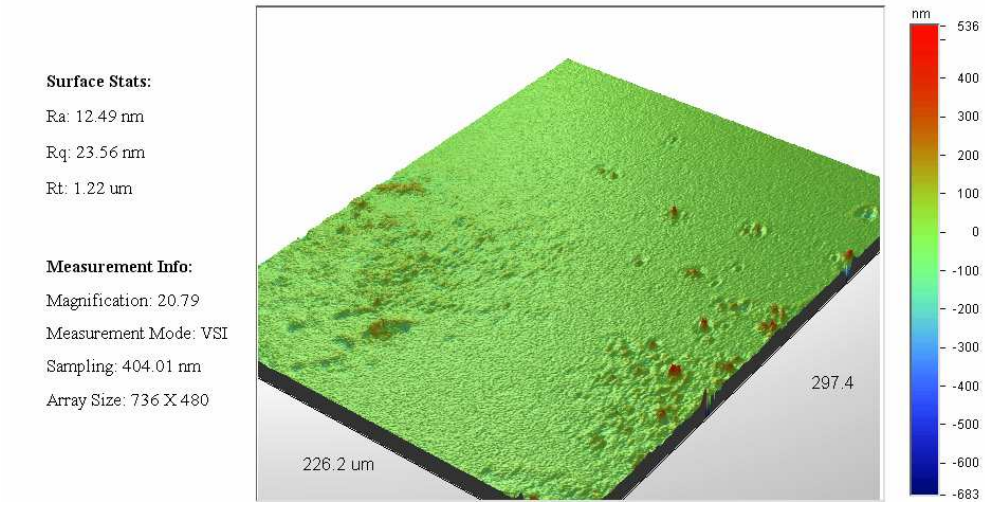

Fig. G3. 13. Parent wafer type: undoped 4H-SiC. Optical profilometric data for laser-treated (laser-doped) wafer surface. The average surface roughness (Ra) is 12.49 nm and the peak to valley roughness is 1.22 μm. This is the Pd-P-doped surface.

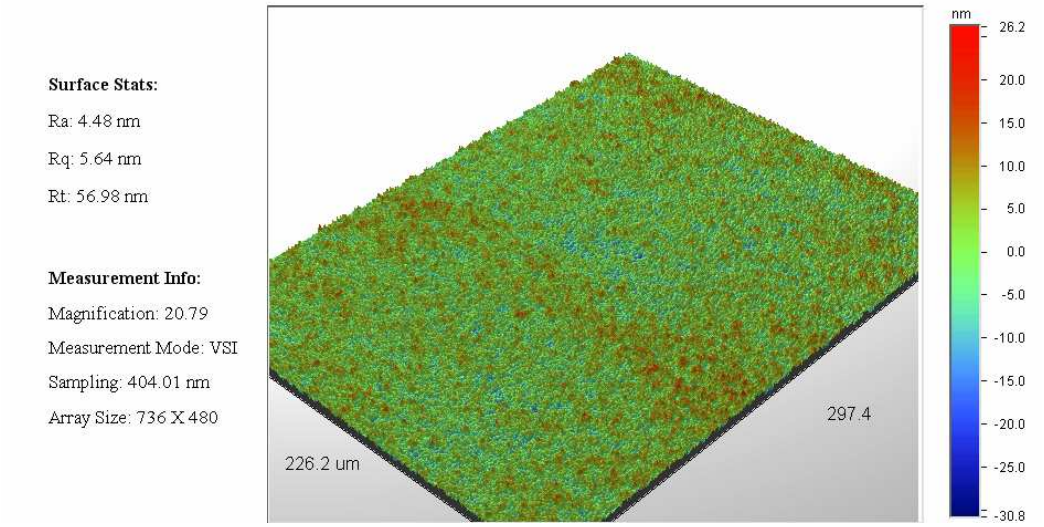

Fig. G3. 14. Parent wafer type: undoped 4H-SiC. Optical profilometric data for laser-untreated wafer surface. The average surface roughness (Ra) is 4.48 nm and the peak to valley roughness is 56.98 nm. This is the opposite surface of the B-doped surface.

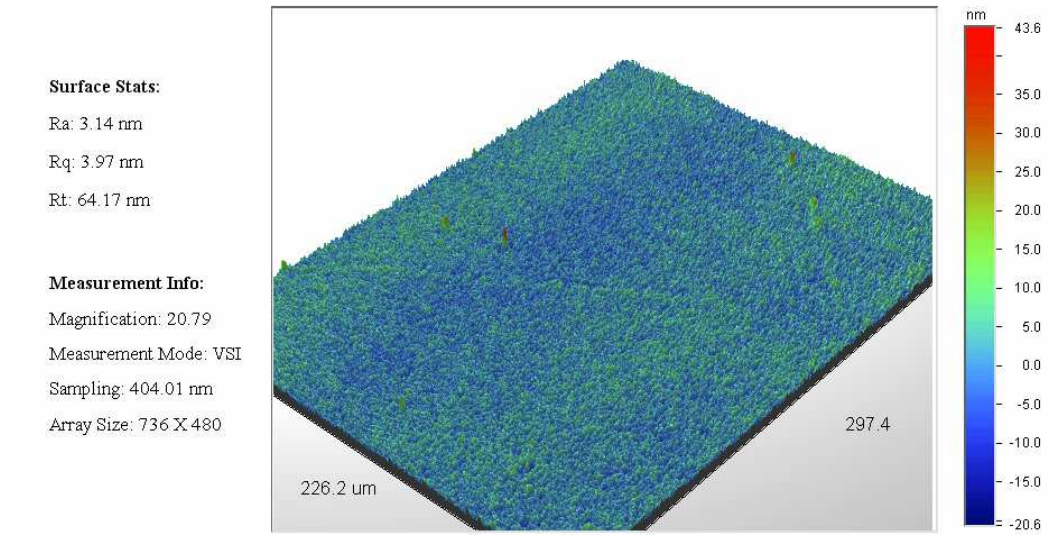

Fig. G3. 15. Parent wafer type: undoped 4H-SiC. Optical profilometric data for laser-treated (laser-doped) wafer surface. The average surface roughness (Ra) is 3.14 nm and the peak to valley roughness is 64.17 nm. This is the B-doped surface.

.

G.4. Temperature Sensor Probe Commercial Test Rig Test at Siemens

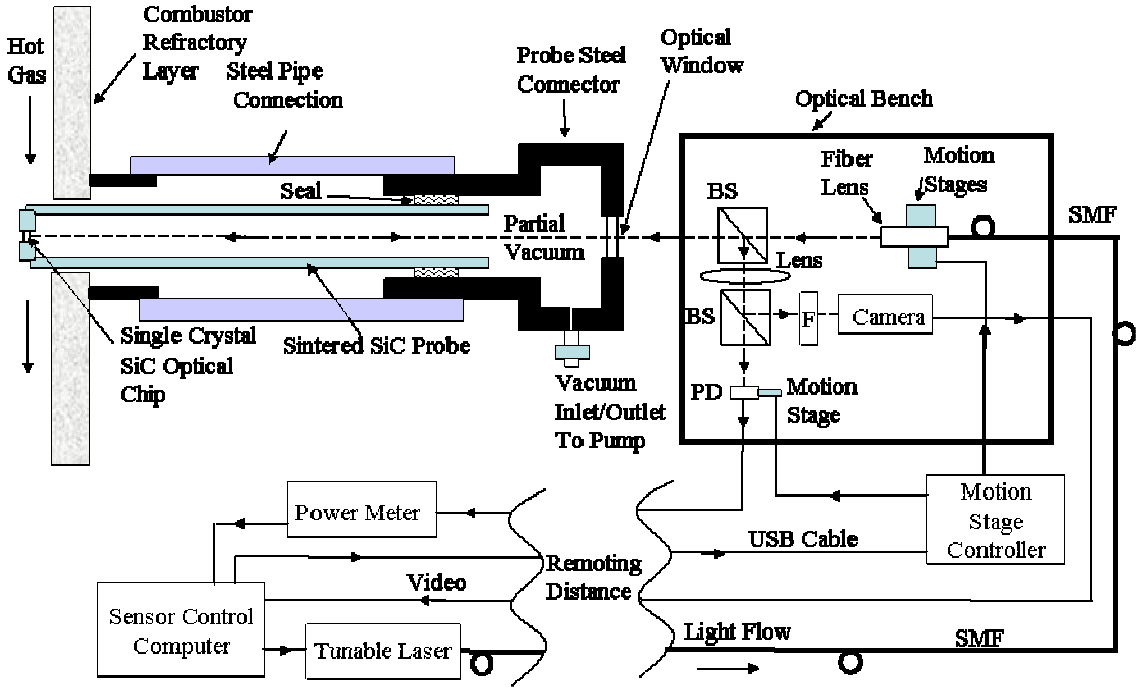

Fig.G4.1. All-SiC frontend probe-based optical sensor system for extreme gas temperature measurements in combustion engines.

Fig.G4.1 shows the basic research design and method of the proposed all-SiC frontend probe sensor system used for extreme gas temperature measurement within the combustor section of a gas turbine. The system is sub-divided into three thermally isolated sub-systems forming a hybrid optical design engaging both wired and wireless optics. The first sub-system represents the sensor controls and processing station that is remotely located at a safe site for human interface. This sub-system includes the sensor control computer, optical power meter, and tunable laser. The remoting distance depending on the electrical signal drive requirements and can range from tens of meters to near a hundred meters. The second sub-system consists of the optical transceiver module containing targeting light beam and detection optics, active

mechanics, and electronics. This transceiver module is located in close proximity (e.g., a few cm) from the frontend probe that forms the third sub-system that is uniquely passive, i.e., contains no lasers, detectors, electronics, or other electrically controlled device. The physical link between the controls sub-system and the transceiver sub-system is via one Single Mode Fiber (SMF) optical cable and three electrical (USB style) cables, providing significant environmental isolation between the two sites. More importantly, the hot frontend probe sub-system is thermally decoupled from the transceiver sub-system with the only physical connection established via a single wireless optical link interfacing the hot SiC optical chip with the laser beam emerging from the SMF-coupled Fiber Lens (FL). The transceiver module is preferably enclosed in an environmentally protected chamber to minimize moisture, dust, and air currents. The transceiver module is designed for under 70 ºC operation that is ideally compatible with turbine manufacturer external safety and technician operational environment requirements. Furthermore, this friendly < 70 ºC temperature range is also compatible with temperature limits for standard fiber-optics, mechanics, and electronics. The transceiver module is mechanically interfaced to a thermally isolated cooler part of the turbine housing. The frontend probe sub-system consists of a steel connector that forms a pressurized fitting at the inlet to the engine combustor section where gas temperature sensing is desired. This steel connector via a high temperature pressure seal connects to a long all-SiC probe that extends slightly into the hot gas section of the combustor. At the tip of this probe is embedded a thick single crystal SiC optical chip packaged within the sintered SiC material thus forming the much desired CTE-matched frontend. As shown, a steel pipe is used as an interface assembly between the probe steel connector and the hot gas section within the thermally isolating refractory layer. The probe steel connector has a high temperature window through which the laser beam travels but equally importantly, the connector has a vacuum inlet/outlet that connects to a on-demand vacuum

pump. Maintaining a partial vacuum within the frontend probe structure is a critical innovation as it essentially eliminates laser beam turbulence along the long thermal ramp influenced probe path that due to air currents within probe can ruin beam alignment between chip and the FL. Furthermore, the partial vacuum prevents the unwanted convection-based cooling of the SiC optical chip from within the probe cavity. Although Fig.G4.1 shows a single refractory layer between the hot gas section and the inlet to the combustor where the probe connector is attached (the scenario for our experiment), a typical deployed commercial combustor has several (e.g., >5) thick refractory layers such that there is a gradual temperature gradient between the extremely hot (say 1500 ºC) gas section and the probe insertion point where temperatures are under 200 ºC. Keeping the overall system design as three independent sub-systems improves system maintenance efficiencies as repairs can be made by independent removal of sub-systems, in particular, the frontend probe that will suffer the most from the harsh environment of the gas turbine.

The sensor system operates as follows. The computer controls the required wavelength and power of the laser as well as providing control signals for the remote motion controller. The computer also stores the received optical power readings for the given wavelength as well as the received Infrared (IR) beam video images from the alignment camera. To measure the gas temperature, the computer instructs the laser to provide optical power of a given infrared wavelength (e.g., 1550 nm) and amount (e.g., 10 dBm) to the SMF that in-turn feeds the FL operated in the low freespace-SMF coupling loss self-imaging condition between SiC chip plane and FL [36]. This light is launched towards the SiC chip sitting at the tip of the probe. The IR beam position at the SiC chip plane is electronically manipulated using piezo-actuators that control the FL translational and tip/tilt conditions such that the IR beam strikes after passing

through the first Beam Splitter (BS) and optical window strikes the SiC chip for optimal retro-reflection. Using the first BS coupled with another second BS, the SiC chip reflected light is routed towards two separate optical detection optics. A lens is used to produce focused beam spots on both the Two Dimensional (2-D) camera, e.g., Charge-Coupled Device (CCD) and the large area point Photo-Detector (PD). The PD is also translated in unison with the FL controls such that the spot stays aligned on the PD active area. The computer processes the optical power and CCD image data and provides feedback control signals to the motion stage controller to adjust the optics for optimal interrogation of the SiC chip. The infrared band filter F (e.g., Bandwidth of 1530-1560 nm) blocks the Black-Body (BB) radiation produced by the SiC optical chip that is captured by the lens optics, thus allowing only the laser beam to pass through to the CCD and hence preventing camera saturation. In short, the sensor system operates to actively target the SiC optical chip and then to properly recover the received retro-reflected temperature coded beam to deduce the SiC chip and hence the gas environment temperature. The SiC chip acts as a temperature sensitive Fabry-Perot cavity and previously described multi-wavelength signal processing techniques implemented via the control computer can be used to deduce the optical chip temperature [11,37]. Do note the SiC chip is of a thick (e.g., 400 microns) single crystal SiC material that is optically flat and mechanically robust for handling high (e.g., 160 atmospheres) pressures [11] and high temperatures (e.g., 1500 ºC). The SiC material that makes the chip and frontend probe is also robust to chemical attack with excellent thermal properties for handling extreme temperatures [37].

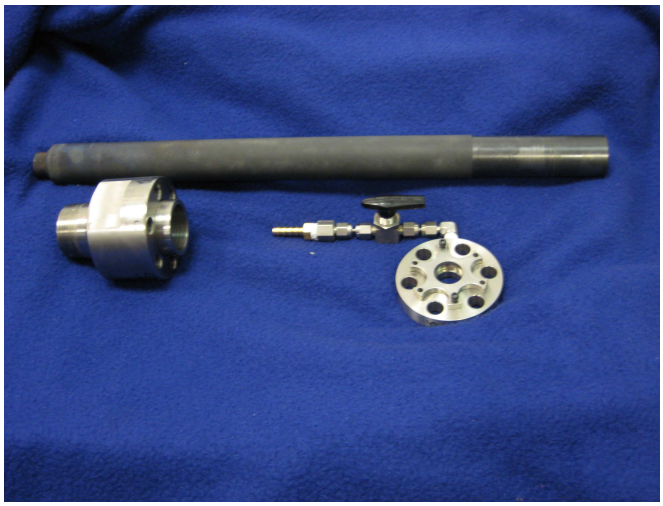

(a)

(b)

Fig.G.4.2. SiC temperature frontend probe shown in an (a) unassembled and (b) assembled fashion.

Fig.G4.2 shows the Nuonics, Inc. provided all-SiC frontend probe displayed in its unassembled and assembled fashions. The point to note is the harsh environment frontend probe assembly consists of three parts, namely, (a) the all-in-one SiC probe consisting of sintered SiC tube assembly with an embedded single crystal SiC optical chip, (b) the pressure sealed steel connector housing that the probe is inserted into to form an interface with pressurized turbine

chamber, and (c) the connector flange with an optical window and vacuum connection housing that can connect to the vacuum pump. The probe uses a 400 micron thick single crystal SiC chip of 1 cm x 1 cm size embedded with a non-porous sintered SiC tube of 41.5 cm length and 2.1 cm and 3.3 cm inner and outer diameters, respectively. The pressure seal between the sintered SiC tube and the steel connector is of Viton material with a maximum sealing temperature of 205 ºC. The window (with 3º wedge angle) is made of a 2.54 cm diameter and 6.35 mm thick Magnesium Fluoride (MgF_2) material with a specified high temperature handling of 500 ºC and 800 ºC in moist and dry conditions, respectively. The wedge design eliminates interference effects from the window acting as a wavelength and temperature sensitive cavity. A Mityvac model EW-79301-20 hand operated vacuum pump is connected to the probe vacuum valve and a 25 inch-Hg (~ 85 kpa) partial vacuum is established within the probe. A cold test of the probe indicates a vacuum drops to 19 inch-Hg and 2 inch-Hg after 62.5 hours and 240 hours (10 days), respectively. The probe is thermally treated over 30 thermal treatment cycles using an oven with a room temperature (~ 20 ºC) to 1100 ºC thermal cycle consisting of a ramp up time of 4.5 hours and cool time of 12 hours.

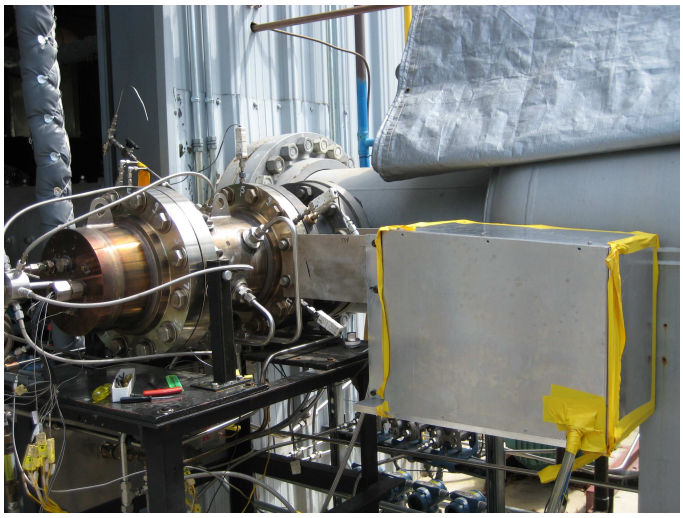

Fig.G4.3. All-SiC temperature sensor deployed for a first test at Siemens rig facility.

Next, the described all-SiC frontend probe along with its Fig.1 transceiver is deployed in a Siemens combustion test rig facility (see Fig.G4.3) to form an industrial scenario gas turbine temperature sensing system. This test combustor is engaged with six reference type B Platinum-Rhodium TCs with ceramic and platinum sheath shieldings and a ± 0.25% uncertainty and 1 second response and data recording time. In addition, the all-SiC probe is located in the combustor exhaust section in close proximity (within ~14 cm) to the TCs that are located at the mid-section of the combustor. The 35.5 cm (length) x 20 cm (width) transceiver optical bench is boxed in a water proofed 48 cm (length) x 30 cm (width) x 37.5 cm (height) aluminum housing that includes a moisture absorbing desiccant bag to counter the rainy high humidity weather in Florida. The housing is also earthed to counter the lightening strikes common in Florida.

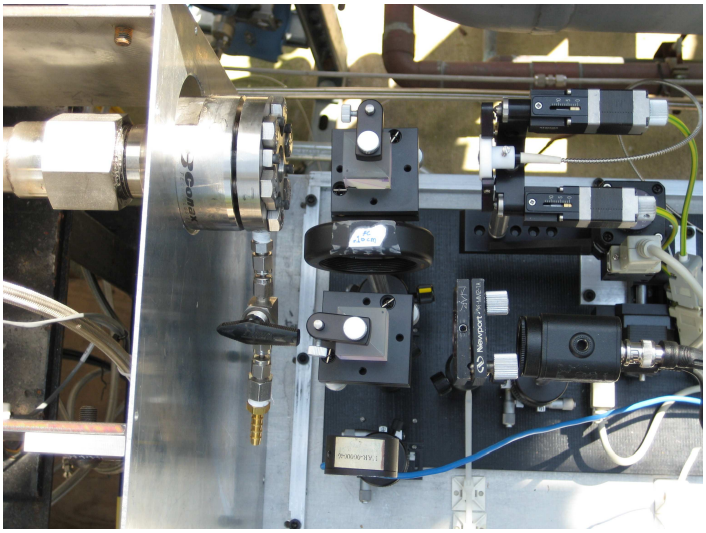

Fig.G4.4 The assembled sensor optical transceiver module top view.

The bench optical layout (see top view in Fig.G4.4) distances are as follows: Fiber lens to First BS: 5.25 cm; Fiber Lens to SiC optical chip: 60 cm; First BS to Probe Window: 6.25 cm; First BS to Focusing Lens: 5 cm; Lens to PD: 11.25 cm; Lens to Camera: 15 cm. The focal length of the lens is 10 cm. Beam diameter size of 0.8 mm is detected on CCD with <0.8 mm diameter

beam on the PD. The PD is a Newport model 818-IR large 3 mm diameter active area point detector while the BB radiation reduction filter F is centered at 1550 nm with a 30 nm (Full-Width Half-Max) passband. The camera is a video rate IR 2-D CCD while Standa piezoelectric translation and tip/tilt motion stages are used to optimize beam alignment. A laser spot size of 550 micron $1/e^2$ beam size forms on the SiC chip. The test rig and control room hardware are connected via 15 meters of one SMF and three 10 m electrical cables. The control room contains other rig operational systems such as TC and pressure data reading electronics as well as combustor flame and fuel monitoring systems. The probe passes through a single 7.62 cm thick combustor refractory layer that for a sample test indicated an external refractory temperature of 426 ºC when the combustion chamber maximum gas temperature reached 1370 ºC, indicating the large (in this case, 944 ºC) thermal insulation power of the deployed refractory.

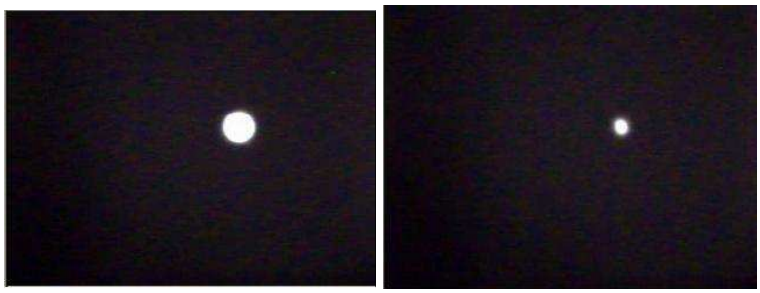

Fig.G4.5. IR CCD camera (8.8 mm x 6.6 mm active area view) received laser beam snap shots during thermal shock stage indicating on/off oscillatory Fabry-Perot etalon behavior of SiC optical chip due to the rapid thermal gradient. Left Photo: Power Max; Right Photo: Power Min.

The rig operation begins with an initial warm up and operational check period when the hot air blowers are turned on and the combustor is pressurized to a desired ~ 100 psi (or 7 atm). For the performed hot rig tests, this warm-up time varied greatly due to various changing on-ground rig conditions and ranged from 20 minutes to 5 hours. Once the rig has reached stable warm-up

operational conditions with a fuel-air ratio ~0.05, the combustor flame is lit. At this stage, the rig temperature drastically ramps up over a 1000 ºC in ~ 3 seconds. In effect, the entire combustor and all its inserted temperature measuring instruments suffer a great thermal shock. In our case of first rig flame lighting, one reference TC completely failed (no electrical signal out) while another gave drastically wrong temperature readings. The remaining 4 TCs continued to supply appropriate temperature readings to the remote data acquisition system. This unwanted behavior of these high performance type-B TCs was expected and hence 6 TCs were deployed for redundancy. The all-SiC probe survived the thermal shock as optical data readings from both the PD and IR CCD continued to register. In fact, the CCD camera recording at the video rate of 30 frames/second produced a rapid sequence of an on/off blinking laser spot (see Fig.G4.4) that spatially darted around a 1 mm diameter around the original alignment point before settling to a beam position within 0.25 mm diameter from its original spot on the camera. The darting around is due to the shock wave the probe frontend suffers on flame ignition causing the SiC chip surface to temporally deform causing the retro-reflected beam to misalign from its original on-axis position of the camera. In addition, the shock wave also slightly misaligns the probe mechanical assembly causing the retroreflected beam to be slightly off its cold alignment position. Nevertheless, both dynamic and settled beam positions stay within the 3 mm diameter active area of the PD and furthermore are well within the CCD image zone to allow the piezo-actuators to optimize beam alignment. The PD's power meter coupled to the control computer is set to take optical power readings after every 78 ms. After the flame light-up, the rig after ~ 30 min settles into its expected high temperature operational range with measured TC maximum temperatures reaching 1239 ºC. Do note that for this particular test rig, one could not set or stabilize the combustor to a given high temperature; thus each time the rig is operated, one finds the combustor temperature sitting in a range between 1100 ºC and 1239 ºC. Over a 28 day

period, the probe was subjected to combustor operations on 6 days, with each given day the combustor tuned on and then off after test operations. After the first rig test, the probe is removed from the rig and inspected for optical and mechanical failures. The probe showed no damage apart from some expected discoloration (see Fig.G4.6) of part of the frontend due to chemical treatment in the hot soup of the combustor refractory zone. The probe is reinserted into the system to continue rig test operations.

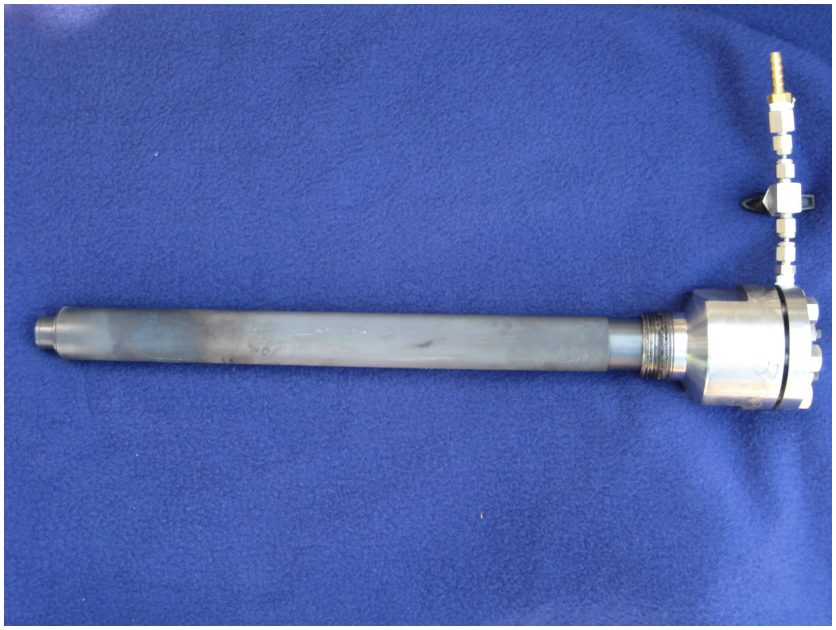

Fig.G4.6 After first rig test of probe, expected part frontend discoloration is seen due to chemical exposure in combustor refractory section.

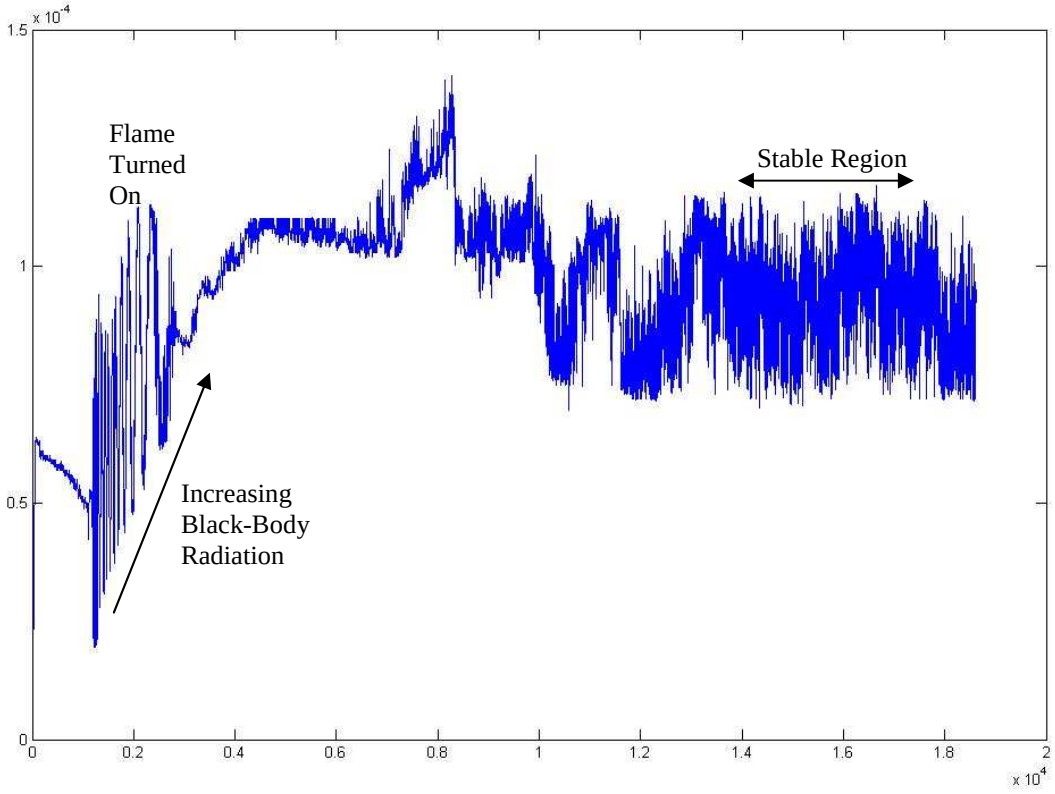

Fig.G4.7. Raw optical data recorded by the probe PD indicating the rig thermal ramp zone and the relative high temperature stabilization zone. Vertical axis is measured optical power in Watts; Horizontal axis is a time counter.

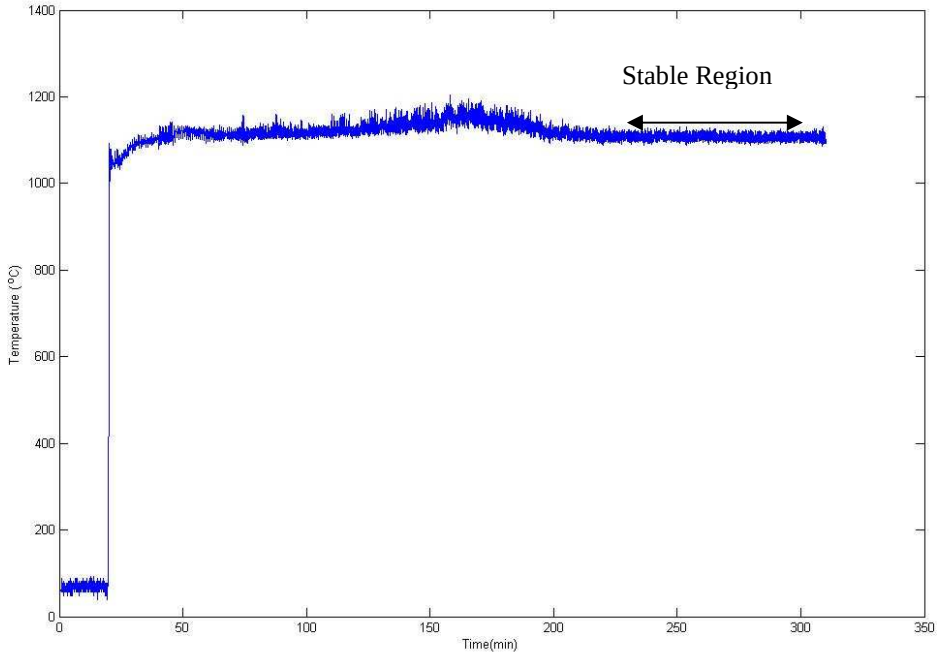

Fig.G4.8 Rig TC provided temperature reading during the Fig.G4.7 optical data acquisition period. This TC data is used for optical probe calibration. Vertical axis is measured temperature; Horizontal axis is a time counter.

Fig.G4.7 shows the raw optical data provided by the PD for one of the test days. For the same test, Fig.8 shows the equivalent temperature readings provided by one of the 4 working TCs in the rig. Both TC and PD data acquisition systems are synchronized via a computer clocks locked time counter so one can have direct one-to-one mapping of probe optical power to TC measured temperature to enable probe calibration. One can clearly see the expected Fabry-Perot effect oscillatory behavior of the optical power during thermal ramping. In addition, the optical power picks up an increasing bias level due to increasing BB radiation during ramping. In addition, the optical power continues to oscillate depending on the rig temperature fluctuations at the set higher temperature zone. This is so as the optical sensor is designed to be sensitive to high

temperature zone changes in a 20 ºC increment indicating that optical power goes from a peak to a null if temperature changes by 10 ºC. This feature points to the fact that the optical sensor can measure temperature to a very high accuracy given the optical power meter is highly sensitive.

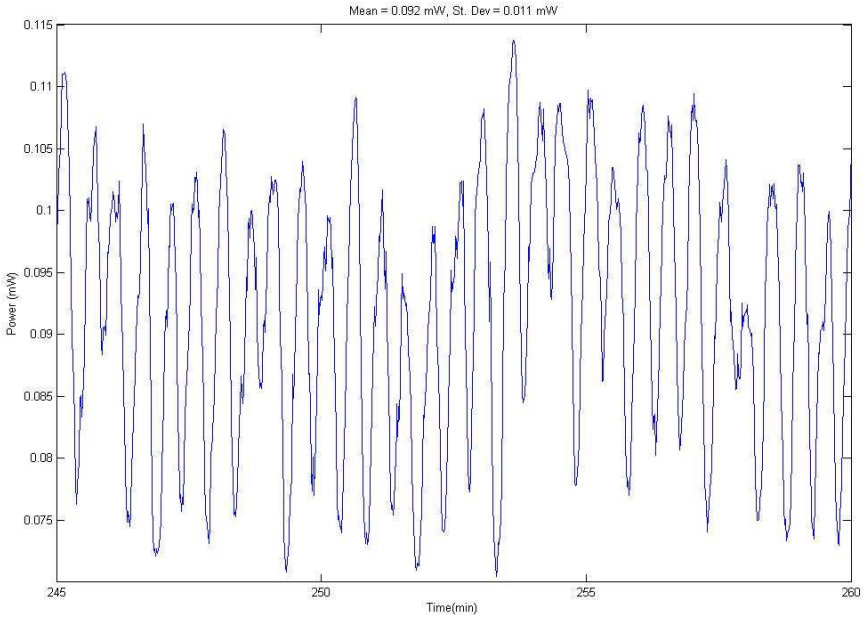

Fig.G4.9. 15 min snap shot of optical power readings from probe during the stable ~ 1107 ºC region of the rig operation.

Fig.G4.9 shows a 15 min snap shot of the probe optical power data taken in the stable ~ 1107 ºC region of the rig operation. This data indicates that the probe temperature measurement Standard Deviation (SD) is ± 2 ºC for time snap shots of 30, 15, and 1 minute sections. Given the deployed power meter accuracy of 1 microW, the given optical sensor has a calculated sensing accuracy of 0.18 ºC. Fig.G4.10 shows the Fig.G4.9 data 15 min. time period TC data. This TC data indicates temperature measurement SD of ± 8.3 ºC, ± 8.1 ºC, and ± 9.9 ºC for time snap shots of 30, 15, and 1 minute sections, respectively. Given that the TC indicates an averaged temperature of 1107 ºC, the specified TC measurement accuracy for this data is ± 2.8 ºC

indicating a possible limitation of TCs compared to the proposed optical probe that has the potential to deliver much better measurement resolution.

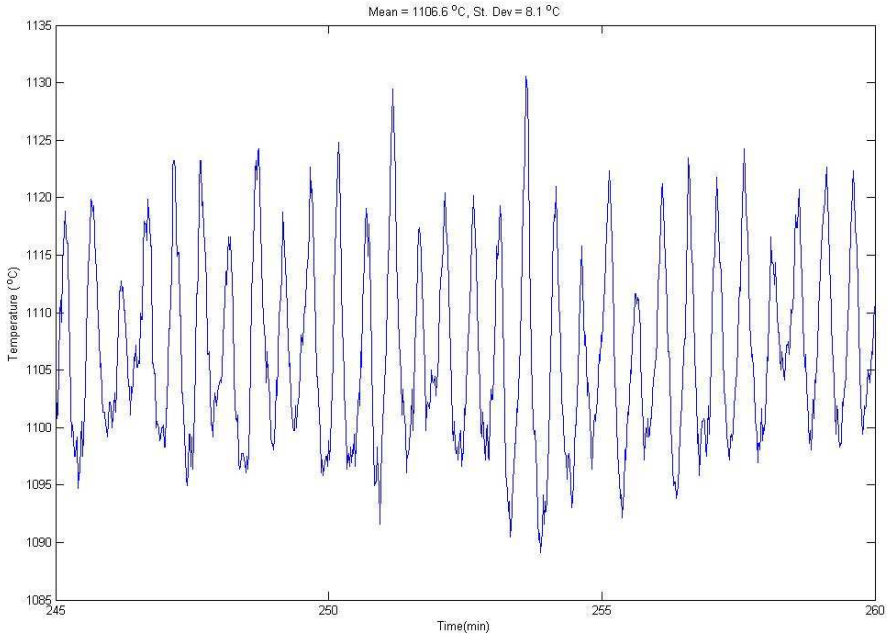

Fig.G4.10 TC data during the Fig.G4.9 data 15 min. time period.

Fig.G4.7 to 10 data, particularly, in the flame light-on region indicates that the optical probe takes a considerable time (~ 30 min) to give stabilized readings. This is so as the present designed all-SiC probe has large thermal mass due to its large highly conducting (thermal) heat sink structure that requires considerable time to reach thermal equilibrium with the rig structure. But do note that once the rig has reached its stable high temperature, the optical probe is quick to pick up small temperature changes. Nevertheless, the probe thermal mass has a clipping effect on the actual temperature readings where the shown ± 8.1 ºC TC readings are clipped to ± 2 ºC probe temperature readings. The solution for reducing this probe limitation is to design a frontend probe package that has much smaller thermal mass providing a slow thermal sinking between the SiC optical chip and the sintered SiC probe package.

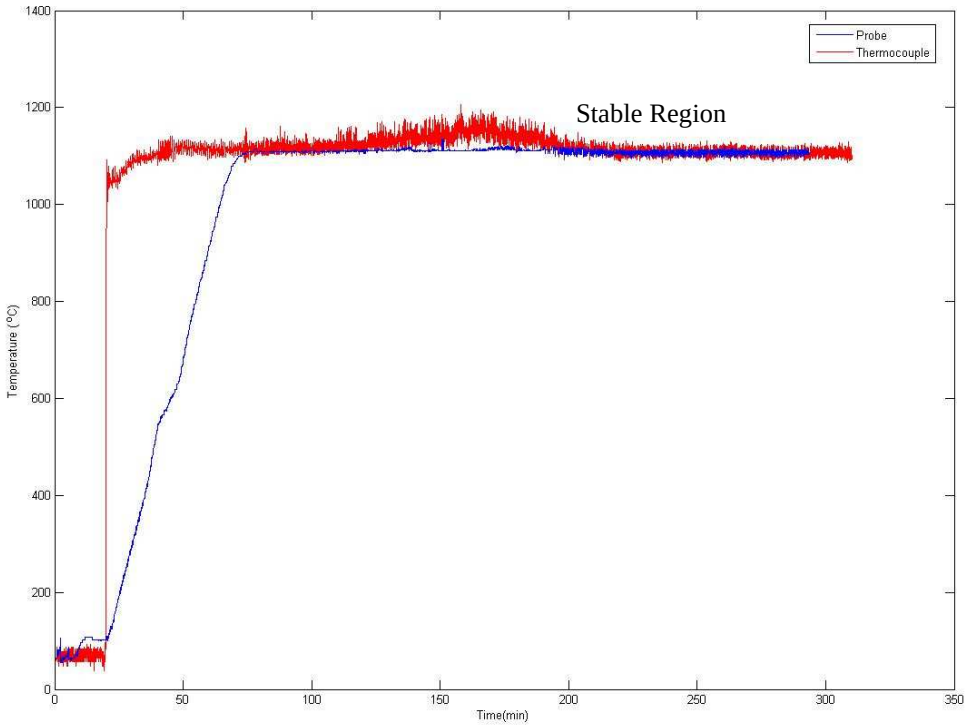

Fig.G4.11. TC calibrated optical probe temperature sensing curve that can be used to deduce temperature readings.

Table G4.1: Summary of all-SiC probe test at Siemens rig.

COMBUSTION RIG FLAME ACTIVE OPERATION	**6 DAYS**
NO. OF TIMES PROBE EXPERIENCED FLAME LIGHT AND THERMAL SHOCK (TEMPERATURE RAMP OF 1000 DEG-C IN 3 SECONDS)	**8 (1 DAY 3 FLAME LIGHTS, 5 DAYS 1 FLAME LIGHT/DAY**
OPERATION WITH FLAME ON	**26 HOURS**
OPERATION WITH FLAME OFF AND BLOWER ON	**13.5 HOURS**
NUMBER OF COMBUSTION HEAT AND COOL CYCLES	**8**
DAYS IN EXTERNAL RIG ENVIRONMENT	**28 DAYS**

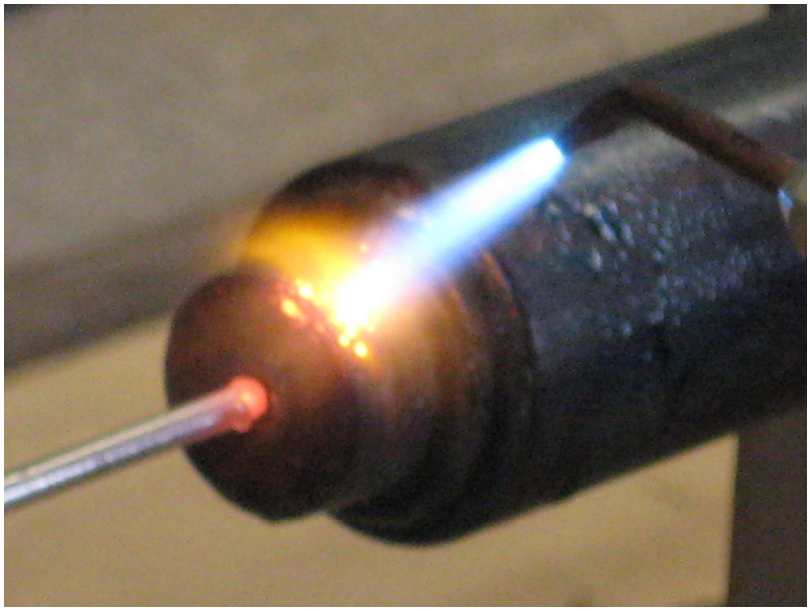

Fig.G4.12. All-SiC probe and Type-R High Temperature Thermo-Couple under oxy-acetylene flame thermal and localized thermal ramp joint test with temperatures reaching 1600 ºC.

Fig.G4.13. Condition of Viton seal used in the probe connector before and after 28 days in rig.

Fig.G4.14 Probe condition showing copper sulphate deposits after 28 continuous days in the rig.

H: RESULTS AND DISCUSSION

H.1 Basic Temperature Sensor

According to Eq. 21, the rate of change of phase is governed by two rates, i.e., $\frac{\partial}{\partial T} n(T)$, also known as the thermo-optic coefficient (TOC) and $\frac{\partial}{\partial T} d(T)$ called the coefficient of thermal expansion α. Both these factors increase with increasing temperature, in particular, the TOC. In fact, the TOC doubles for a change of 300^0C from room temperature. The increase in TOC increases the refractive index and therefore the optical path length (or the optical phase shift) increases at a greater speed producing an increase in the rate of change of phase with temperature. Note that Eq. 21also contains refractive index and thickness in them and the absolute increase in these factors further enhances the value of rate of phase change at higher temperature. Hence, the temperature change that causes a full power cycle decreases with temperature increase because now the phase change of 2π is obtained for smaller change of temperature. This explains why the full optical power cycle temperature change decreases from a value of 30^0C at room temperature to a value of 20^0C at 1000^0C. Finally, do note that the

proposed sensor can also be operated in an alternate signal processing wideband wavelength swept mode that simulates a broadband input source in time. Because state-of-the-art commercial tunable lasers in the 1550 nm band can sweep wavelength at a fast millisecond regime, a wide (e.g., 100 nm) spectral source can be quickly synthesized for the proposed sensor. In this case, the proposed sensor can generate the Fabry-Perot wavelength response of the SiC etalon at the instantaneous temperature without requiring a spectral resolution limited optical spectrum analyzer instrument. Nevertheless, the peak or notch movement of the synthesized received optical spectrum will have to be monitored to access temperature change, thereby running into the temperature sensing resolution constraints limited with monitoring individual notch or peak positions when the etalon spectral shape can deteriorate with changing high hazard extreme sensing conditions. In effect, if the deep notch (or peak) shape changes to a spectrally broad notch (or peak), the sensor temperature resolution will degrade. Furthermore, this data processing is based on a non-robust approach where over the entire temperature range of the sensor, one looks for one given optical power minimum (or maximum) value (here we are assuming equal notch depths) and determines temperature value by measuring the wavelength shift for this minima (or maxima). In the proposed sensor signal processing, full cycle optical power readings and not just a minima (or maxima) power reading gives the sensor measured temperature. Hence, the proposed sensor can use a more robust approach to processing that takes into account many optical power readings and not just a localized minima (or maxima) power reading. Of course, both signal processing methods can be engaged in the proposed sensor without any hardware changes, thus adding built-in redundancy and fault-tolerance to the temperature measurements via the proposed minimally invasive sensor.

Note that the proposed system does not require super-accurate positioning on a micron or $< 0.01^0$ scale as needed with near field SMF optics where coupling light from a freespace beam

to a SMF requires extreme precision. This is because the proposed sensor system is a hybrid fiber-freespace design system where the SMF is used to launch a high spatial quality small beam spot size (e.g., < 0.5 mm diameter) laser beam in the sensing target region and the large aperture freespace beam capture receive optics is used for the return beam power-based detection. Specifically, transverse alignment on both transmit and receive beams is done on a rather large sub-millimeter scale (e.g., 1 mm) implying that the transmit beam hits within for example a 1 mm diameter zone of the SiC chip where the chip is also optically flat over the target zone. Similarly, the receive beam hits within a 1 mm diameter zone of the receive optics that can be a large 3 mm diameter freespace optical detector such as used for the demonstrated experiment or a large diameter multi-mode fiber. Note that the Fig.1 shown alignment and beam control mirror optics using today's state-of-the-art mirrors can scan at fast kilo-Hertz (KHz) rates keeping beams on the chip and receive detector targets despite environmental effects such as vibrations. In addition, these mirrors are excellent for sub-degree high resolution beam pointing allowing the freespace transmit beam to be quickly and accurately angularly adjusted for near normal incidence targeting of the thick SiC chip.

H.2. Basic Pressure Sensor

An extreme environment wireless pressure sensor design has been proposed using a thick single crystal 6H-SiC chip seated in a pressure capsule that can be designed for extreme conditions. The sensor operates on the principle of remote laser beam targeting, SiC chip optical weak lensing, and received beam image measurement. The concept has been tested up-to 41 atm with an initial 1.17 atm pressure measurement resolution. Experimental results also show a linear mechanical and optical behavior of the SiC chip and sensor demagnification parameter read-out indicating

the expected robustness of the SiC chip technology under high pressures. Mechanical deflection analysis points to a clamped seating case for the SiC chip within the capsule while chip stress analysis indicates a robust design reaching 140 atm and beyond. One can greatly improve the pressure measurement resolution by decreasing the pixel size and increasing the size of the optical beam on the CCD plane. The Fig.19 plots indicate that the SiC chip seating is closer to the clamped case, an expected results because of the pressure washer (seal) used to maintain the chip in a sealed arrangement. In addition, the Fig.19 results indicate a linear operation of the demonstrated pressure sensor with the SiC chip performance well within the linear elastic small deformation range, a need for long-life repeatable robust sensor operations. Sensor resolution can be improved with optimized SiC chip and capsule designs. These initial results attest to the promise and strengths of SiC chip-based optical wireless sensor technology for fossil fuel based power generation system applications.

H.3. Gas Species Sensor

(Kar LAMP Lab. Provided Information & Assessment)

All 6H-SiC parent wafers were fabricated. Sample set 4 (Pd-P and B doped) were delivered by Applicote Associates to LAMP Kar Lab. Note that all wafers were purchased in a bulk to reduce expenses. These wafers have been diced to a square shape with perfect dimension so that the chip can fit into Kar's experimental setup with maximum gas sealing for experiments at high temperatures and high pressures using existing diamond saw technology. A very sharp diamond saw blade was used to scribe a 1 cm $\times$ 1 cm grid in the wafer. A scribed corner or edge of the wafer was placed on a rectangular metal substrate aligning the scribe lines with the metal substrate edges; light tapping on the scribe lines freed the chips. This approach proved adequate for the LAMP Lab limited sample requirements. A continuous wave wavelength of 632.8 nm

was used to understand the changes in the refractive index (n_3) of a compressed layer at the chip-gas interface in the presence of a combustion gas such as H_2, CO, CO_2, and CH_4 for both Pd-P and B doped samples. The combustion gases are present in the combustor in trace amounts as presented in Table G3.1. The SiC chip is inherently a Fabry-Pérot interferometer enabling optical measurements pertaining to interference patterns that were analyzed to calculate the compressed layer refractive index, n_3. Both B and Pd-P doped silicon carbide chips have been tested by the Kar LAMP Lab. to examine their sensitivity to different combustion gases. B doped SiC have been found to affect the refractive index of SiC over a small temperature range 100-150°C for methane gas. Further studies are necessary to dope various polytypes of SiC, e.g., 4H-SiC, 6H-SiC and 3C-SiC, with a variety of dopant atoms in different concentrations in order to increase the gas selectivity of SiC chips.

H.4. Probe Industrial Testing at Siemens

Using the Fig.G4.7 BB radiation data (provided by the DC bias level of the recorded optical power) and its equivalent temperature values from the TC data, Fig.G4.11 shows the TC calibrated optical probe temperature sensing curve that can be used to deduce temperature readings. The Fig.G4.11 curve shows that the stable region average temperature of gas in rig is 1107 ºC and the SD in the indicated 60 minutes stable region is ± 6.3 ºC and ± 2 ºC given by the TC and probe, respectively. Ideally, the optical probe must be calibrated using a temperature measuring device that has far better measurement accuracy than today's high temperature TCs as the optical probe exhibits great sensitivity. In addition, the probe calibration must be done at a much slower temporal rate versus an uncontrolled thermal shock mechanism of the rig. Nevertheless, the present rig test of the proposed all-SiC probe technology has proven its operational robustness in the harsh conditions of a commercial test combustion rig.

Specifically, Table G4.1 shows the conducted key operational parameters for the probe rig test. For example, the probe survived 8 thermal up-ramps of 1000 ºC, each ramp in less than 3 seconds. The probe also survived localized thermal shock (see Fig.G4.12) and maintained mechanical integrity when subjected to an oxy-acetylene flame that produced temperatures near 1600 ºC. In fact, the R type thermo-couple began to melt using the oxy-acetylene flame set-up while the all-SiC probe stayed intact. It is important to note that the on/off modulation depth of the retroreflected signal off the SiC optical chip varied from 20:1 to 2:1 during the 28 days of rig tests as different parts of the external chip zone were optically spoiled to a different degree by the hot chemical soup in the combustor. Using the active beam alignment system in the probe, one was highly effective in finding a high modulation depth spot on the chip for effective optical power data recording, again proving the versatility of the smart beam targeting probe design when operating under harsh conditions of a commercial gas turbine. As the optical power meter is highly sensitive, even a 2:1 optical power ratio between a 10 ºC temperature change provides significant signal processing resolution to calculate the measured temperature with high (e.g., 0.2 ºC) accuracy.

The probe operated successfully for 28 days, eventually developing a vacuum seal breakage (see Fig.G4.13) in the pressurized connector on the lower temperature side of the probe. This led to unwanted combustor cooling water entry into the probe at high temperatures (~ 1200 ºC) and stoppage of probe operations. A higher (> 200 ºC) temperature insulating pressure seal needs to be deployed to prevent seal break-down. Do note that during operations, the temperature of the external part of the probe steel connector registered a 200 C reading, indicating that heat from the combustor was efficiently traveling via the probe structure to the external connector chamber. This can indeed be prevented in a deployed combustor using many more thermally insulating

refractory layers between probe frontend and connector zone. This would lead to a much lower connector external temperature and also much lower temperature experienced by the Viton seal in the connector. Fig.G4.14 shows the probe condition after 28 continuous days in the rig. One can notice the blue copper sulphate deposits on the probe frontend. This is indeed so as the combustor chamber was made from copper and the cooling water had sulphur content in it.

I: CONCLUSION

Basic Temperature Sensor:

Proposed and demonstrated to 1000^0C is a novel extreme temperature optical sensor using tunable light, free-space beam targeted single crystal SiC chip front-ends, strong two-beam single wavelength interferometry, and robust multi-wavelength signal processing concepts to simultaneously provide both high resolution and wide unambiguous range sensing for dynamic scenarios. Unlike previous wavelength sensitive sensors (e.g., FBG & etalon), the proposed sensor design is not dependent on optical spectrum analyzer hardware resolution. Because temperature assessment is based upon monitoring optical power data over full min/max cycles and not just locating and tracking minima or maxima (as in traditional FBG and etalon-based sensors), a better sensor resolution can be achieved particularly when the etalon optical spectral filter function peaks/nulls shape change as etalon interface optical reflectivities change based on conditions in the dynamic sensing zone. The proposed sensor relies on instantaneous single wavelength interferometry, thus eliminating inter-wavelength crosstalk issues. The sensor has an operating potential temperature near 2500^0C, the melting point for single crystal SiC. Because single crystal SiC is a highly robust material from a mechanical and chemical point of view, the proposed sensor can also be adapted for extreme environment pressure and chemical species

sensing. The proposed sensor can also produce traditional broadband spectral power sensing data using laser tuning. The tunable laser can also be temporally modulated to reduce system noise by generating the desired optical power data on an intermediate frequency (IF) for low 1/frequency noise signal processing including heterodyne processing. The proposed sensor can also be used to characterize materials under extreme conditions. Strictly speaking, the optical power max/min data provided by the proposed sensor occur for the SiC chip condition $cos\ (\phi) = \pm 1$. From these data points collected over a given sensing parameter (e.g., temperature) range, sensor OPL=ϕ can be calculated that contains SiC material refractive index, thickness, and wavelength data. If the two-beam interferometry condition valid for the SiC chip is invoked, all P_m data points can be used to compute SiC material parameters such as the change of index with temperature called thermo-optic coefficient.

Pressure Sensor:

Proposed is the first extreme environment wireless pressure sensor design using a remoted single crystal SiC chip within a pressurized capsule. A detailed theoretical analysis of the sensor system is performed including the SiC chip mechanical response within the pressure capsule and the pressure measurement technique optical response based on image demagnification. The remote sensor is experimentally tested at room temperature for pressures up-to 41 atm. and sensor response is consistent with the theoretical analysis. The demonstrated sensor has a current experimental resolution of 1.17 atm with a designed maximum pressure range of 140 atm. Improved sensing resolution and range can be achieved via optimal selection of SiC chip dimensions and its seating in the pressure capsule.

Gas Species Sensor:

Dual simultaneous laser doping of Palladium and Phosphorus laser doping have been achieved in 4H-SiC substrates. These 1 cm x 1 cm chips in addition to a new set of Boron laser doped 4H-SiC substrates and Pd-P substrates have been studied for combustion gas sensing applications. The experiments have so far provided no robust mechanism of gas species sensing for the coal-fired power plant scenario.

Commercial Test:

Reported is the world's first commercial rig test for an all-SiC probe technology for temperature sensing in fossil-fuel-based gas turbines. The test has successfully shown that the proposed technology is robust and handles the extreme environments of power plant turbines. The probe has survived many 1000 deg-C thermal ramp shocks within a 3 seconds time frame. The probe has operated successfully for 28 days in the rig. The probe has maintained mechanical and optical robustness with sustained temperatures reaching 1250 deg-C and local shocks reaching 1600 deg-C. The proposed smart sensor design has countered industrial setting requirements for continuous sensor operations. In conclusion, the proposed all-SiC probe technology is ready for sustained advanced engineering and development to realize the optimized TC-like probe package for next generation gas turbines.

J: REFERENCES

1. J. H. Ausubel, " Big Green Energy Machines," The Industrial Physicist, AIP, pp.20-24, Oct./Nov., 2004.
2. R. E. Bentley, "Thermocouple materials and their properties," Chap. 2 in *Theory and Practice of Thermoelectric Thermometry: Handbook of Temperature Measurement*, Vol. 3, pp. 25-81, Springer-Verlag Singapore, 1998.
3. H. Ernst, L. Rauscher, G. Bähr, E. Müller, and W. A. Kaysser, "Long-term stability and thermal cycling of thermocouple contacts to Si up to 350°C," The Third European Conference on High Temperature Electronics (HITEN), pp. 87 – 90, 4-7 July 1999.
4. B. Lee, " Review of the present status of optical fiber sensors," Optical Fiber Technology, Vol.9, pp.57-79, 2003.
5. M. Winz, K. Stump, T.K. Plant, " High temperature stable fiber Bragg gratings," Optical Fiber Sensors (OFS) Conf. Digest, pp.195-198, 2002.
6. D. Grobnic, C. W. Smelser, S. J. Mihailov, R. B. Walker, "Isothermal behavior of fiber Bragg gratings made with ultrafast radiation at tempertaures above 1000 C," European Conf. Optical Communications (ECOC), Proc. Vol.2, pp.130-131, Stockholm, Sept. 7, 2004.
7. H. Xiao, W. Zhao, R. Lockhart, J. Wang, A. Wang, " Absolute Sapphire optical fiber sensor for high temperature applications," SPIE Proc.Vol. 3201, pp.36-42, 1998.
8. D. Grobnic, S. J. Mihailov, C. W. Smelser, H. Ding, " Ultra high temperature FBG sensor made in Sapphire fiber using Isothermal using femtosecond laser radiation," European Conf. Optical Communications (ECOC), Proc. Vol.2, pp.128-129, Stockholm, Sept.7, 2004.
9. Y. Zhang, G. R. Pickrell, B. Qi, A. S.-Jazi, A. Wang, "Single-crystal sapphire-based optical high temperature sensor for harsh environments," *Opt. Eng.*, **43**, 157-164, 2004.

10. N. A. Riza, M.A. Arain, and F. Perez, “Harsh Environments Minimally Invasive Optical Sensing Technique for Extreme Temperatures: 1000 °C and Approaching 2500 °C,” in 17th International Conference on Optical Fibre Sensors, OFS 17, Proc. SPIE Vol. 5855, pp. 687-690, Bruges, Belgium, May 2005.
11. N. A. Riza, M. A. Arain, and F. Perez, “Harsh Environments Minimally Invasive Optical Sensor using Freespace Targeted Single Crystal Silicon Carbide,” IEEE Sensors Journal, Vol. 6, No. 3., pp 672-685, June 2006.
12. N. A. Riza, M. A. Arain, and F. Perez, “6-H Single Crystal Silicon Carbide Thermo-optic Coefficient Measurements for Ultra High Temperatures up to 1273 K in the Telecommunications IR band,” J. Appl. Phys., Vol.98, pp. 103512, 2005.
13. N. A. Riza, M. Sheikh, and F. Perez, “Progress on Silicon Carbide Hybrid-Design Optical Sensors for Extreme Environments,” in OSA 18th International Conference on Optical Fibre Sensors, OFS 18, Paper ThE54, Cancun, Mexico, Oct.23, 2006.
14. N. A. Riza and M. A. Arain, “Cryogenic Temperature Measurement using Silicon Carbide-based Wireless Optical Sensor**,”** IEEE Photon. Tech. Lett., Vol. 18, No. 24, pp. 2599-2601, Dec. 2006.
15. N. A. Riza, M. Sheikh, F. Perez “Wireless Temperature Sensors using Single Crystal Silicon Carbide – An Industrial Feasibility and Design Study,” in Optical Sensing III, F. Baldini, J. Homola, and R. Lieberman, eds., SPIE International Photonics Europe Congress, SPIE Proc. Vol. 6585, Paper No.19, pp. 65850J, Prague, Czech Republic, April 17, 2007.
16. N. A. Riza, M. Sheikh, and F. Perez, “Design and Fabrication of an Extreme Temperature Sensing Optical Probe using Silicon Carbide Technologies,” in IEEE Sensors 2007 International Conference, pp. 660-662, Atlanta, GA, Oct. 28-31, 2007.

17. N. A. Riza, F. N. Ghauri, and F. Perez, “Hybrid Optical Sensor using Laser Targeting,” in Optical Sensing II, SPIE International Photonics Europe Congress, Proc. SPIE Vol. 6189, Invited Paper No.4., pp. 32-46, Strasbourg, France, April 3-7, 2006.
18. N. A. Riza, F. N. Ghauri, and F. Perez, “Wireless Pressure Sensor using Laser Targeting of Silicon Carbide,” Optical Engineering, Vol. 46, No. 1, pp 014401, Jan. 2007.
19. N. A. Riza, F. N. Ghauri, and F. Perez, “Silicon Carbide based Remote Wireless Optical Pressure Sensor,” IEEE Photon. Tech. Lett., Vol. 19, No. 7, pp. 504-506, Apr. 2007.
20. S. P. Timoshenko and S. Woinowsky-Krieger, “Pure Bending of Plates,” Chapter 2, in *Theory of Plates and Shells*, pp. 56-57, (McGraw-Hill Inc., New York, NY 1959).
21. NIST Structural Ceramic Data Base, SRD Data Base No.30. (www.ceramics.nist.gov/srd/summary/scdscs.htm)
22. R. G. Munro, “Material properties of a Sintered alpha-SiC,” Journal of Physical and Chemical Reference Data, Vol. 26, pp. 1195-1203, 1997.
23. W.N. Sharpe, O. Jadaan, G.M. Beheim, G.D. Quinn, N.N. Nemeth, “Fracture Strength of Silicon Carbide Micro-specimens,” IEEE Journal of Microelectromechanical Systems, Vol. 14, No. 5, pp. 903 – 913, Oct. 2005.
24. E. Hecht, Optics, p.148, Eqn.5.36, 2nd Edition, Addison-Wesley, Reading, MA, 1990.
25. Atallah E. Batshon, Jonathan C. Backlund, Alternate Fuels for Supplementary Firing Add Value and Flexibility to Combined Cycle and Cogeneration Plants, Power-Gen International 2001, December 11-13, 2001.
26. G. Cocurullo, F. G. Della Corte, I. Rendina, Temperature dependence of the thermo-optic coefficient in crystalline silicon between room temperature and 550 K at the wavelength of 1523 nm, Applied Physics Letter, V 74, No. 22, 1999, pp. 3338.

27. S. Dakshinamurthy, N.R. Quick and A. Kar, SiC-based optical interferometry at high pressures and temperatures for pressure and chemical sensing, Journal of Applied Physics, Vol. 99, 2006, pp. 094902-1 to 094902-8.
28. S. Dakshinamurthy, N.R. Quick and A. Kar, Temperature-dependent optical properties of silicon carbide for wireless temperature sensors, J. Phys. D: Appl. Phys., Vol. 40, 2007, pp. 353-360.
29. Wen-Chau Liu; Hsi-Jen Pan; Huey-Ing Chen; Kun-Wei Lin; Shiou-Ying Cheng; Kuo-Hui Yu, Hydrogen-sensitive characteristics of a novel Pd/InP MOS Schottkydiode hydrogen sensor, Vol. 48, Issue 9, Sep 2001 pp.1938 – 1944.
30. S. Roy, C. Jacob, S. Basu, Studies on Pd/3C-SiC Schottky junction hydrogen sensors at high temperature, Sensors and Actuators: B, Vol. 94, Oct. 2003, pp. 298-303.
31. Zhao G, Charlson E. M., Charlson E. J., Meese J., Stacy T., Popovici G., and Prelas M. "Silver on Diamond Schottky Diodes Formed on Boron Doped Hot-Filament Chemical Vapor Deposited Polycrystalline Diamond Films," Appl. Phys. Lett., 61 (9), 1992, pp. 1119-1121.
32. Z. Tian, I.A. Salama, N. R. Quick and A. Kar, Effects of Different Laser Sources and Doping Methods used to Dope Silicon Carbide, *Acta Materialia,* Vol. 53, 2005, pp. 2835-2844.
33. Z. Tian, N. R. Quick and A. Kar; Characteristics of 6H-Silicon Carbide PIN Diodes Prototyping by Laser Doping, *Journal of Electronic Materials*, Vol. 34, 2005, pp. 430-438.
34. I.A. Salama, N. R. Quick and A. Kar, Microstructural and electrical resistance analysis of laser-processed SiC substrates for wide bandgap semiconductor materials, *Journal of Materials Science,* Vol. 40, 2005, pp. 3969-3980.
35. Z. Tian, N.R. Quick and A. Kar, Laser-enhanced diffusion of nitrogen and aluminum dopant in silicon carbide, Acta Materiallia, Vol. 54, 2006, pp. 4273-4283.

36. M. van Buren and N. A. Riza, “ Foundations for low loss fiber gradient-index lens pair coupling with the self-imaging mechanism,” Applied Optics, Vol. 42, No.3, pp. 550-565, Jan. 20, 2003.

37. N. A. Riza and M. Sheikh, “Silicon carbide based extreme environment temperature sensor using wavelength tuned signal processing,” OSA Optics Letters Journal, Vol.33, No.10, pp.1129-1131, May 15, 2008.